d/Collection

Doctor of Philosophy

A study on Interface Engineering for High-performance Polymer Solar Cells

The Graduate School

of the University of Ulsan

Department of Physics

Sujung Park

February 2021

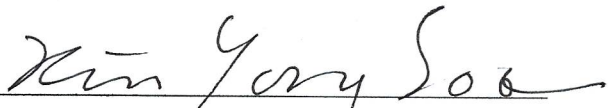# A study on Interfacial Engineering for High-performance Polymer Solar Cells

Supervisor : Shinuk Cho

A Dissertation

Submitted to

the Graduate School of the University of Ulsan

In partial Fulfillment of the Requirements

for the Degree of

Doctor of Philosophy

by

Sujung Park

Department of Physics
Ulsan, Korea

February 2021

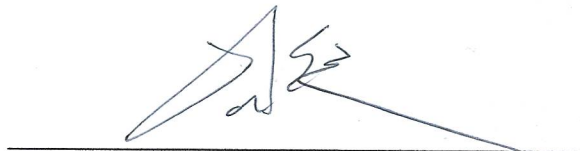# A study on Interfacial Engineering for High-performance Polymer Solar Cells

This certifies that the dissertation/thesis of Sujung Park is approved.

Committee Chair Dr. Yong Soo Kim

Committee Member Dr. Shinuk Cho

Committee Member Dr. Sanghoon Kim

Committee Member Dr. Sung-Yeon Jang

Committee Member Dr. Jung Hwa Seo

Department of Physics
Ulsan, Korea

February 2021

Abstract

Organic solar cells (OSCs) have attracted much attention as energy source for future mobile electronics because of their advantages such as low manufacturing cost, lightweight, flexibility, and transparency, etc. The development of new organic materials and more efficient device structures has enabled rapid progress of OSCs in recent years. The power conversion efficiency (PCE) of OSCs is now exceeded over 17%. Although the low PCE which was one of the serious problem has been overcome, and considered to be one-step loser to commercialization, further improvement in performance is still needed to compete with other solar cells based on inorganic semiconductor which was already commercialized. The charges generated by incident light from the photoactive layer should pass through the interface after separation and transfer to reach the electrode. However, even a few tens meV of the energy barrier formed at the interface between the photoactive layer and charge transport layer can cause significant charge accumulation, thereby leading to a decrease in photovoltaic characteristics. Therefore, an appropriate interface engineering is essentially required to achieve effective charge transport by preventing charge recombination at the interface. In this study, the various interface engineering methods were introduced to maximize the performance of OSCs and analyzed their effects on real devices.

In the first work, the interface problem between PEDOT:PSS and photoactive layer was investigated. Since the PEDOT:PSS hole transport layer has a metallic property intrinsically, it can form an energy barrier by means of metal-semiconductor contact at its interface with the photoactive layer. In this study, hydroquinone (HQ) was applied on PEDOT:PSS surface to remove this contact barrier at the interface between metallic PEDOT:PSS HTL and semiconducting photoactive layer. HQ treatment of the PEDOT:PSS surface lowered the hole transport barrier and reduced sheet resistance of PEDOT:PSS via the secondary doping effect of HQ. Thus, the device fabricated with the HQ-modified PEDOT:PSS showed a 28% increase in PCE compared to the device without HQ treatment.

In the second work, the interface problem of tunnel-junction intermediate connection layer (ICL) was investigated. In tunnel-junction type tandem solar cells, the ICL generally consists of a hole conducting layer and a polyethyleneimine (PEI) polyelectrolyte layer. However, because pristine PEI is intrinsically an insulator, the photocurrent is limited even if it is slightly thick in the intermediate connection layer. In this study, high-efficiency homo-tandem solar cells are demonstrated with enhanced efficiency by introducing carbon quantum dot (CQD)-doped PEI on tunnel-junction ICL. The tandem solar cells with CQD-doped PEI layer in ICL leads to a better series connection in tandem solar cells and it yields a

maximum PCE of 12.13%, representing a 15% increase compared with tandem solar cells with a pristine PEI layer.

In the third work, the effect of interface engineering on the charge dynamics of the photoactive layer was explored. The exciton dissociation probability is also affected by the internal field generated by the work function difference between cathode and anode. In this study, The CQD having NH_2 ligands added to the PEI work-function modifying layer to improve both work-function modification effect and charge transport property. A CQD-doped PEI layer induced a lower work-function of ITO than that of ITO with a pristine PEI, which induced a stronger internal field. This strengthened internal field induced better exciton dissociation efficiency, thereby improving performance of OSCs.

In the last work, the interface problem between PEDOT:PSS and ITO electrode was investigated. The low-conductivity PEDOT:PSS such as AI4083 is mainly utilized in current OSCs. Thus, the contact between PEDOT:PSS and ITO are not ohmic. Despite the high possibility that there are serious interface problems, little attention has been paid to the interface between PEDOT:PSS and ITO. In this study, a conjugated polyelectrolyte WPFSCz- employed between ITO and low-conductivity PEDOT:PSS to overcome complicate organic-inorganic interfacial problems. The inserted WPFSCz- layer modifies the work-function of the ITO, thereby forming effective cascading energy alignment, which is favorable for good hole transport. Also, the introduction of WPFSCz- layer reduces recombination losses at the interface by eliminating the interfacial trap sites, resulting in an improvement in fill factor. These effects result in a significant increase in the PCE from 15.86 to 17.34%.

Through these researches, the interface problems caused by contact between different types of materials can be overcome by introducing various interfacial engineering methods in OSCs. These methods enhanced PCE by improving charge transfer characteristics and charge extraction characteristics, thereby achieving high-performance OSCs successfully.

Table of Contents

List of Figures

List of Tables

List of Abbreviations

Abbreviation	Description
AFM	atomic force microscopy
AIM	anode interface material
BHJ	bulk-heterojunction
CA	citric acid
CB	chlorobenzene
CF	chloroform
CIM	cathode interface material
CN	1-chloronaphthalene
CQD	carbon quantum dot
DIO	1,8-diiodooctane
EQE	external quantum efficiency
ETL	electron transport layer
FF	fill factor
FTIR	Fourier-transform infrared spectroscopy
G_{max}	exciton generation rate
HOMO	highest occupied molecular orbital
HQ	hydroquinone
HRTEM	high-resolution transmission electron microscopy
HTL	hole transport layer
IMPS	intensity-modulated photocurrent spectroscopy
IMVS	intensity-modulated photovoltage spectroscopy
IPA	isopropyl alcohol
IQE	internal quantum efficiency
IS	impedance spectroscopy
ITO	indium tin oxide
J_{ph}	photocurrent density
J_{SC}	short circuit current
KPFM	Kelvin probe force microscope
LUMO	lowest unoccupied molecular orbital
OSC	organic solar cell
P(E, T)	exciton dissociation probability
$PC_{71}BM$	[6,6]-phenyl-C71-butyric acid methyl ester
PCE	power conversion efficiency
PEDOT:PSS	poly(3,4-ethylenedioxy-thiophene):poly(styrenesulfonate)
PEI	polyethyleneimine
PEIE	ethoxylated polyethyleneimine
PSC	polymer solar cell
PTB7-Th	poly[[4,8-bis[5-(2ethy-lhexyl)thiophen-2-yl]benzo[1,2-b:4,5-b0]dithiophene-2,6-diyl][3-fluoro-2-[(2-ethylhexyl)carbo-nyl]thieno[3,4-b]thiophenediyl]]
QY	quantum yield

RMS	root mean square
SRH	Shockley-Read-Hall
TPC	transient photocurrent
TPV	transient photovoltage
UPS	ultraviolet photoelectron spectroscopy
V_{eff}	effective voltage
V_{OC}	open circuit voltage
WF	work-function
WPFSCz-	9-(2,7-Diethylheptyl)-2,7-bis(4,4,5,5-tetramethyl-1,3,2-dioxaborolan-2-yl)-9H-carbazole, 2,7-dibromo-9,9-bis(4-sulfonatobutyl) fluorene dipotassium, and potassium poly[9,9-bis(3′-sulfonatopropyl)fluorene-*alt*-(9-(2,7-diethylheptyl)-carboazole)]
XPS	x-ray photoelectron spectroscopy

Chapter 1. Introduction

1.1 Organic Solar Cells (OSCs)

1.1.1 History of OSCs

The first example of a conducting polymer Polyacetylene was developed by Hideki Shirakawa, Alan MacDiarmid and Alan Heeger in 1977.[1] They tried to improve the conductance and study the polymer system and were able to reach conductivities as high as many metals. Though polyacetylene itself proved to be too difficult to work with and unstable to be used commercially, their discovery lead to an entire field of conducting polymers, including poly(p-phenylene vinylene) (PPV) used in some organic light emitting diode displays and the polythiophene based materials used in OSCs. This work led to them being awarded the 2000 Nobel Prize in Chemistry. A breakthrough occurred in 1986, when Tang showed that much higher efficiencies are attainable by producing a double-layered cell using two different dyes, which had a large photocurrent density, of the order of mA/cm^2, and an efficiency of 1%.[2] This result had a big impact on the field of organic solar cells. A blended junction for small molecule cells was proposed in 1991 by Hiramoto.[3,4] In 1992, Sariciftci reported a polymer heterojunction cell composed of C$_{60}$ and MEH-PPV (poly[2-methoxy-5-(2-ethylhexyloxy)-1,4-phenylenevinylene]).[5] Followed in 1995, a polymer bulk-heterojunction (BHJ) cell reported by Yu.[6] After 2000, based on these fundamental studies, the efficiency rose from 1% and started to increase rapidly and reached 17.5% as shown 1.1.[7] In recent years, Due to the continuous development of active materials[8-12] and device structure engineering, such as tandem, ternary device[13-16],and interfacial engineering[17-21], Power conversion efficiency (PCE) of OSCs has exceeded 17% by choosing matched donor and acceptor materials in photoactive layer.[22]
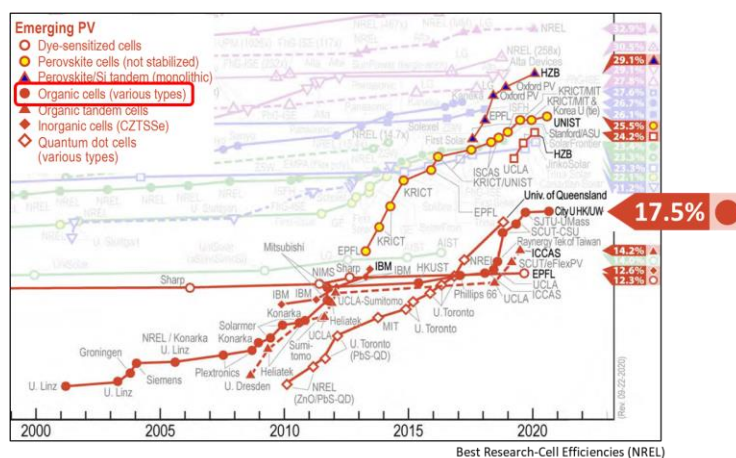
Figure 1.1. Current best research-cell efficiencies in OSCs.

1.1.2 Principle of OSCs

The OSC is a type of solar cell where the absorbing layer is based on organic semiconductors, typically either polymers or small molecules. For organic materials to become conducting or semiconducting, a high level of conjugation is required. The electrons associated with the double bonds become delocalized across the entire length of conjugation due to the conjugation of the organic molecule. These electrons have higher energies than other electrons in the molecule and are equivalent to valence electrons in inorganic semiconductor materials.

However, in organic materials, these electrons do not occupy a valence band but are part of what is called the 'highest occupied molecular orbital' (HOMO). Also, there are unoccupied energy levels at higher energies just like inorganic semiconductors, it is called the 'lowest unoccupied molecular orbital' (LUMO). Between the HOMO and LUMO of the organic semiconductors is an energy gap. With increased conjugation, the band gap will become small enough for visible light to excite an electron from HOMO to LUMO. When the energy of light is equal to or greater than the band gap, leading to absorption and excitation of an electron from the HOMO to the LUMO. The excited electron will leave behind a positively charged space known as a hole. Due to the opposite charges of the hole and electron, they become attracted and form an electron-hole pair, also known as an exciton. The OSCs have low dielectric constants, giving large exciton binding energy values in the range of 0.3-0.7 eV.[23] Because the exciton cannot be dissociated by thermal energy alone, at least two different organic semiconductors are needed. The energy levels between the two different organic semiconductors are offset, with the difference being greater than exciton binding energy, allowing exciton dissociation to occur at the interface between them. Depending on electron has been donated by a material, or accepted by a material, the organic semiconductors are classified as either a donor or acceptor.

The working principle of OSCs can be summarized four steps which required for generation of electrical power via the absorption of incident light:

i) Absorption of photons and formation of photo-induced excitons in donor and acceptor, respectively.

ii) The excitons diffusion and dissociation at the donor and acceptor interface.

iii) Charge-transfer (CT) states generation and then dissociation into free charge carriers (electrons and holes) with an ultrafast quasi-adiabatic charge transfer process.

iv) Charge carriers that are transported through either donor and acceptor and then being collected by the respective electrodes transfer process.
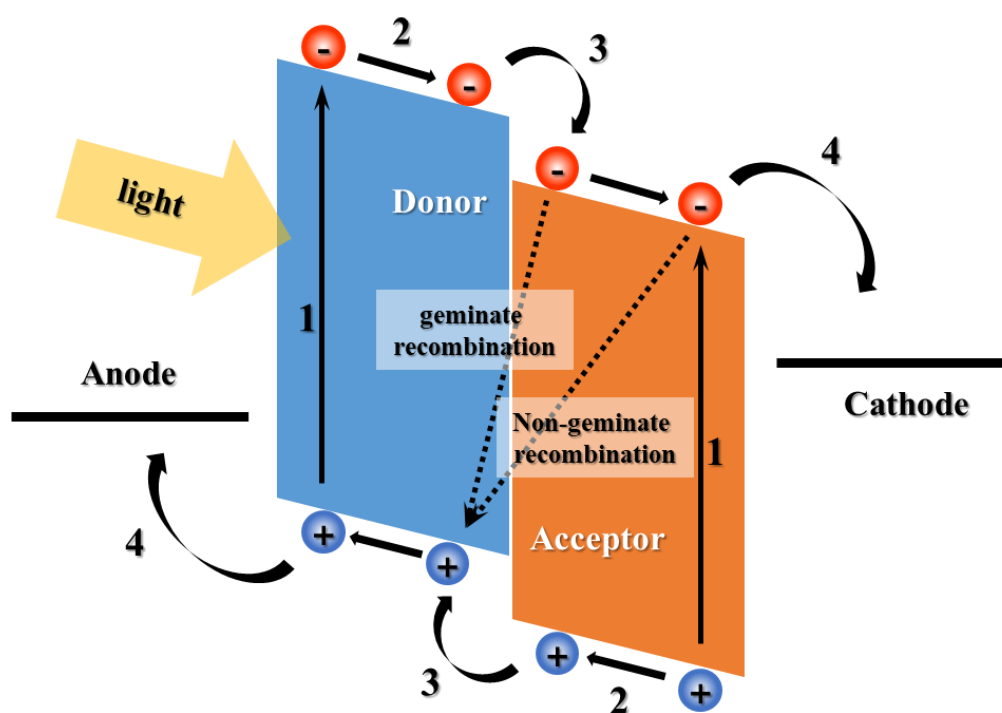
Figure 1.2. The operational principle of BHJ OSCs.

The separated charge carriers may recombine with each other (geminate recombination) before dissociation. Moreover, the separated charge carriers may also be recombined (bimolecular recombination or non-geminate recombination) before collected by the respective electrodes. The germinate and non-germinate recombination have a great effect on the low PCEs in BHJ OSCs.

1.1.3　Structures of OSCs

1.1.3.1　Bilayer & BHJ OSCs

C. W. Tang introduced the world's first two-layer thin-film solar cell with an efficiency of 1% in 1986.[1] In the bilayer structure, a transparent electrode ITO is used as an anode, and a metal having a low work-function is used as a cathode, and a donor material and an acceptor material are stacked as a photoactive layer between them as shown in **Figure 1.3a**. However, since it only takes about 100 ps for the holes and electrons of excitons to recombine, the exciton diffusion length is only about 10 nm. There is a limit to the contact area between them, revealing a limit to the formation of free holes and electrons. To overcome this limitation, a BHJ structure which a donor material and an acceptor material are properly mixed has been developed. As shown in **Figure 1.3b**, it has the advantage of improving photovoltaic conversion efficiency because the interface between the photoactive layer is wide. If the donor and acceptor form a heterojunction structure in the nanometer region within the photoactive layer, excitons excited by light absorbed by the photoactive layer will be separated into free electrons and holes in the adjacent p-n junction region. For excitons to be separated into free electron-holes at the p-n junction interface, the difference between the LUMO or HOMO energy levels of the two materials must be greater than the exciton binding energy. The electrons and holes separated at the many p-n junction interfaces distributed throughout the photoactive layer diffuse and flow to both electrodes along the donor and acceptor respectively to form photocurrents. Therefore, it is important that the donor and acceptor have proper phase separation in the nanometer region in order to separate electrons and holes and transfer to both electrodes. In 1995, A. J. Heeger group announced that BHJ structure solar cell greatly helps to improve efficiency as a solution process that has a much lower process cost compared to vacuum deposition.[24] Currently, OSCs with an efficiency approaching 18% are fabricated by a simple spin-coating method, and the BHJ structure is widely used in OSC research.
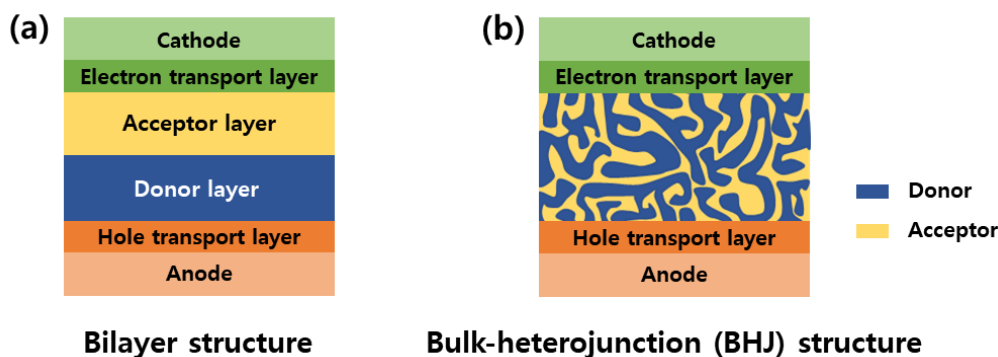
Figure 1.3. The binary device structure of bilayer and BHJ.

1.1.3.2 Ternary OSCs

Despite significant advances in binary BHJ cells, the PCE of OSCs needs to be further boosted to realize practical applications and commercialization. However, their performance is restricted by the insufficient coverage of the solar spectrum of binary blends because of the intrinsic narrow absorption bands of organic semiconductors. On the other hand, as organic molecules typically present low charge carrier mobility, BHJ films usually retain very thin (as low as 100 nm) to gain efficient charge collection, unfortunately, which cannot fully capture all incident sunlight in their absorption ranges.[25] Recently, a ternary OSCs incorporating a simple process of a single-junction OSCs has been in the limelight having the advantage of minimizing the thermalization loss and a wide absorption area of the tandem OSCs. The ternary OSCs consisting of three light absorbing materials (a donor, an acceptor, and an additional third component donor or acceptor) in one photoactive layer. And the third component plays a crucial role in improving the film morphology, facilitating exciton dissociation, and enhancing charge transport of binary BHJ cells. Accordingly, ternary OSCs have been investigated to further increase the PCE of OSCs. According to the functionality of the third component, it can be classified into four categories: charge transfer, energy transfer, parallel-like, and alloy model as shown in **Figure 1.4**. The third component is limited to the donor material in Figure 1.4. Even if the acceptor material becomes the third component, the charge transport mechanism is the same.[26]

In case of charge transfer mechanism as shown in the **Figure 1.4a**, the third component locates at the interface of the main donor and acceptor that transfers the charge to the electrode with forming cascade energy levels alignment. That is, holes generated at the donor 1 and acceptor interface are directly extracted to the anode, and electrons are extracted to the cathode through donor 2 and acceptor. On the other hand, holes generated at the donor 2 and acceptor interface pass through donor 1 to the anode, and electrons are collected directly to the cathode. Thus, the observed V_{OC} of such systems is basically fixed to the smaller V_{OC} of the original binary systems. In the energy transfer mechanism as shown in the **Figure 1.4b**, the big difference from other mechanism is that the emission spectrum of the third component needs to substantially overlaps with the absorption spectrum of the primary donor or acceptor. In other words, there is an energy donor that transfers energy without generating a charge carrier and an energy acceptor that not only absorbs light by itself, but also absorbs the light emitted by the energy donor to generate charge carrier. The location of the energy donor within the photoactive layer should be near the energy acceptor due to the limited energy transport distance. If the energy transfer mechanism of the donor 1, donor 2 and acceptor-based ternary OSC is applied, the exciton energy of donor 1 is transferred to donor 2 through Förster or Dexter energy transport, and the excitons generated in donor 2 are separated at the donor 2 and acceptor interface and creates charge carrier. The generated electrons are collected along acceptor to the cathode, and holes are extracted to the anode

5

through donor 1 or directly to the anode according to the relative HOMO energy level position of donor 1. Therefore, similar to the charge transport mechanism, the change in the V_{OC} is insignificant. The following parallel-like mechanism or alloy model, two binaries operate independently as one photoactive layer without requirements such as morphology, energy level, and band gap of the ternary photoactive layer. In other words, in a donor 1, donor 2 and acceptor-based ternary organic solar cell, when a parallel-like or alloy model is applied, holes and electrons generated at the donor 1 and acceptor interface are directly collected to the anode and cathode along each pathway. In addition, holes and electrons generated at the donor 2 and acceptor interface are also independently extracted directly to each anode and cathode. Therefore, in parallel-like or alloy model, the V_{OC} of the ternary OSC is determined by the ratio of the ternary photoactive material. In the parallel-like mechanism, When the donor 2 absorbs light, splits excitons and transports holes, that is, the third component forms its own independent hole-transport network. In this case, the V_{OC} values of ternary OSCs lie between the measured values of the two individual binary cells and it depends on the composition of the ternary mixture, rather than being fixed by the LUMO energy levels of the acceptors or the HOMO energy levels of the donors (**Figure 1.4c**). Unlike the parallel-like mechanism, the Alloy Model, on the other hand, is electronically coupled between two photoactive materials to form a new charge-transfer (CT) state energy which would require a good miscibility and compatibility of the donor materials as shown **Figure 1.4d**. The CT state energy in such a system was shown to be a function of the ternary blend composition and followed the shift in V_{OC}.[27]
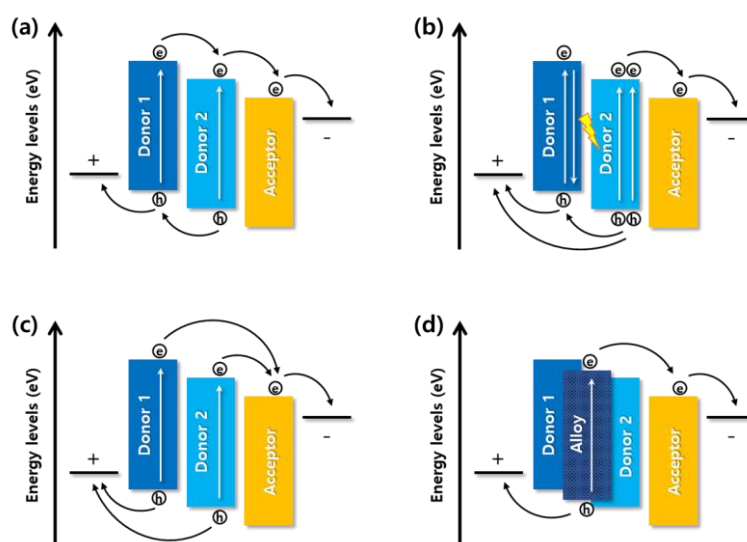
Figure 1.4. Schematic of the working mechanisms in ternary organic solar cells. (a) The charge transfer mechanism. (b) The energy transfer mechanism. (c) The parallel-like mechanism. (d) The alloy model.

1.1.3.3 Tandem OSCs

The single-junction BHJ OSCs have achieved a significant improvement of over 17% power conversion efficiency through the synthesis of highly effective polymer or small molecule materials and device development, but due to a narrow absorption area (~120nm), low exciton diffusion length with low charge carrier mobility (~10^{-5} cm^2 /Vs) and thermalization loss, it is difficult to expect further efficiency improvement for single-junction OSCs. The research on a tandem OSCs has been studied to realizing high performance organic solar cells by overcome this problem. The working principle of the tandem cell is as follows. First, excitons are formed by absorption of light in the top and bottom cells. Second, after excitons are separated from each cell, holes in the bottom cell collect electrons in the top cell and recombine near the intermediate layer. Although the described working principle is based on an inverted tandem OSCs, the principle is the same only the direction of the charge carrier is opposed in the conventional structure.[28-29]

In tandem OSCs, as shown in **Figure 1.5a**, independent single-junction organic solar cells are physically separated by an intermediate layer and can be connected either in series or in parallel depending on the nature of the intermediate layer and on the way the intermediate layer and the two electrodes are connected. Normally, the series connection is widely used. The tandem OSCs can be roughly divided into hetero-tandem OSCs and HOMO-tandem OSCs. The hetero-tandem OSCs is a wide-bandgap material for the bottom cell in combination with a narrow-bandgap material for the top cell with complementary absorption spectra and minimal absorption overlap and The HOMO-tandem OSCs is a same donor material for both sub-cells that comprise high internal quantum efficiency (IQE) in single cells with high PCEs. In the overall tandem OSCs, the thickness of the photoactive layer of each sub-cell is optimized by the light absorption coefficient, band gap, and charge mobility of the photoactive layer. In general, the thickness of the photoactive layer in the bottom cell is thinner than that of the top cell.

The energetic diagram of the device can be represented as in **Figure 1.5b**. In tandem OSCs, intermediate connection layers (ICLs) plays an important role in the overall device characteristics. The ICLs generally consist of a p-type hole transporting layer (HTL) and an n-type electron transporting layer (ETL) and should allow the recombination of holes coming from one sub-cell with electrons coming from the other. In the ICLs, the vacuum level which driven by the alignment of fermi levels of the HTL and ETL is simultaneously shifted. To satisfied ideal ICLs, it should be highly transparent and robust enough to protect underlying layers, and they should form ohmic contact with sub-cell photoactive layers to ensure efficient charge extraction. Therefore, The ICLs optically and electrically connects the sub-cell and also, the formation of HTL and ETL of ICLs is very important because

improves optical field distribution and charge transfer collection to top cell are different depending on which HTL and ETL are used for ICL. Since the tandem OSC is connected in series of bottom cell and top cell, the V_{OC} of the tandem OSC is equal to the sum of the V_{OC} of the two sub-cells. However, J_{SC} appears smaller than each cell. This is because the current value in the tandem OSCs has the current of the sub-cell having a small current, where the light absorption of the top cell absorbs light that has not been absorbed by the bottom cell, the top cell generally generates a relatively low current value because it absorbs light with a lower intensity. Even though the fabrication method is more complicated than the other structure such as binary and ternary structures, and there is a disadvantage that the material for ICLs can be limited by annealing process, still has a high possibility that high efficiency tandem OSCs can be achieved by more efficient new materials, functional intermediate layers and better matching of the materials with complimentary absorption spectra.[30]
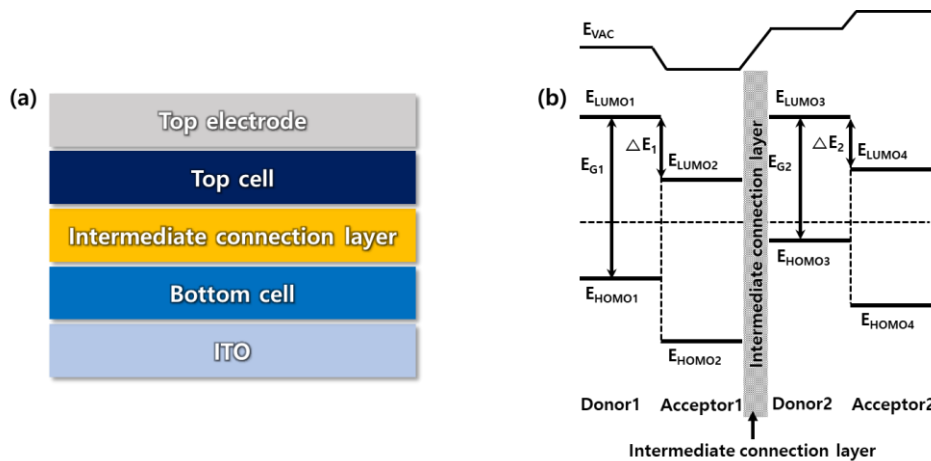
Figure 1.5. (a) Device structure of tandem solar cells, (b) Simplified band diagram of a tandem cell made of two sub-cells connected in series via an intermediate connection layer.

1.2 Characterization of OSCs

1.2.1 Device Characterization

The fundamental electrical characterization of a photovoltaic diode is carried out by obtaining curves of electric current density vs. an external voltage (bias), the so-called *J-V* curves. The *J-V* curve is one of the most common methods of determining how an electrical device functions in a circuit. A typical *J-V* curve for a solar cell is shown in **Figure 1.3**, in the dark and under illumination. The photocurrent density J_{ph} is a subtraction between the two *J-V* curves (illuminated and dark), which are described by the Equations (1) and (2), where J_o is the reverse dark current, *V* is the bias voltage, n is the diode quality factor, k is the Boltzmann constant and T is the temperature.

$$J(V) = J_0 \left[\left(\frac{eV}{nkT} \right) - 1 \right] \qquad (Shockley's\ equation) \qquad \text{Equation (1)}$$

$$J(V) = J_0 \left[\left(\frac{eV}{nkT} \right) - 1 \right] + J_{ph} \qquad (under\ illumination) \qquad \text{Equation (2)}$$

The parameters that characterize solar cells in general are shown in **Figure 1.3**, the short-circuit current density (J_{sc}), the open-circuit voltage (V_{oc}) and the maximum operating power (P_{max}), which determine the fill factor (FF).[31]

The short circuit current density (J_{sc}) is the current that flows when there is no external field applied; the charges are drifting because of the internal field. J_{sc} is determined by the number of photons absorbed (the number of photoexcitations), the quantum efficiency for charge separation, and the transport of the charge carriers through the material. A broad absorption spectrum is advantageous, for one wants to harvest as large a fraction as possible of the photons from the broad spectrum of the sun.

The open circuit voltage (V_{oc}) is defined as the maximum voltage that is obtained when no current is generated by the solar cell. V_{OC} is determined by the difference in the quasi-Fermi levels of the phase. The open circuit voltage is given by Equation (3).

$$V_{oc} \approx E_{acceptor(LUMO)} + E_{donor(HOMO)} + k_B/e\{\ln\,(n_e n_h / N_c^2)\} \qquad \text{Equation (3)}$$

where n e and n h are the electron and hole densities, respectively and N_c is the corresponding density of states near the acceptor lowest unoccupied molecular orbital (LUMO) and the donor highest occupied molecular orbital (HOMO), assumed to be equal. However, the excellent correlation required the addition of an additional 0.3 eV of unknown origin and it directly from the third term in Equation 1. In principle, V_{oc} can be increased by the difference in work functions of the anode and cathode. However, the use of interlayers (electron transport/hole blocking and hole transport/electron blocking) tends to decouple the V_{oc} from the difference in the anode and cathode work functions.[32]

The fill factor (FF) is determined by the competition between sweep-out of the photogenerated carriers and the recombination of carriers to the ground state. Normally, The FF is defined as the ratio of the maximum operating power (P_{max}) to the maximum extractable power from an ideal solar cell, which would be the product of the device area A, V_{oc}, and J_{sc}.

Thus, the power conversion efficiency is the ratio of the maximum operating power P_{max} to the input power of the incident light on the solar cell. Therefore, under an incident light intensity I_{in}, the FF and the power conversion efficiency (η) are given by Equations (4) and (5).

$$FF = \frac{P_{max}}{A J_{sc} V_{oc}} \qquad \text{Equation (4)}$$

$$\eta = \frac{J_{sc} V_{oc}}{I_{in}} FF \qquad \text{Equation (5)}$$
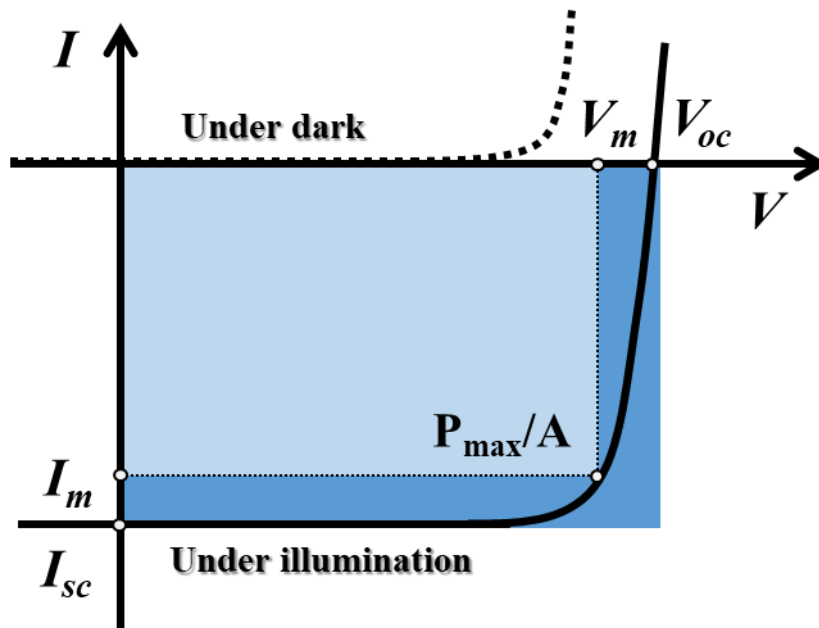
Figure 1.3. The current-voltage characteristics of a solar cell and the photovoltaic parameters.

The quantum efficiency (QE) measurement is critical for material research and device analyzation to understand the conversion efficiency as a function of the wavelength of light. The QE of a solar cell which referred to as incident photon to charge carrier efficiency (IPCE) indicates the ratio of the number of photons incident on device to the number of generated charge carriers. In other word, the QE is defined as the ratio of the number of electrons in the external circuit produced by an incident photon of a given wavelength. The two types of QEs are often considered: external quantum efficiency (EQE) and internal quantum efficiency (IQE). They differ in the treatment of photons reflected from the device. All photons effect on the device surface are considered in the value of the EQE but only photons that are not reflected are considered in the value of IQE.

The external quantum efficiency (EQE) defined as the number of electrons generated by light in the external circuit divided by the number of incident photons as a function of excitation wavelength. Thus, EQE is often useful tool for look at the quantum efficiency of the light left after the transmitted and reflected light has been lost. The EQE is given by Equation (6). Also, because J_{SC} can be calculated by integrating the EQE curve of overall wavelength using Equation (8), the J_{SC} obtained through the EQE measurement can be confirmed whether J_{SC} obtained from the illuminated IV curve is the correct value.

The internal Quantum Efficiency (IQE) refers to the efficiency with which photons that are not reflected or transmitted out of the device can generate collectable carriers. The IQE curve can be corrected to obtain the EQE curve by measuring the transmission and reflection of device. The IQE is given by Equation (7).

$$EQE = \frac{electrons/sec}{photons/sec} = \frac{(current)/(charge\ of\ one\ electron)}{(total\ power\ of\ photons)/(energy\ of\ one\ photon)} \qquad \text{Equation (6)}$$

$$IQE = \frac{electrons/sec}{absorbed\ photons/sec} = \frac{EQE}{1-Refelction} \qquad \text{Equation (7)}$$

$$J_{sc} = q \int \Phi(\lambda)EQE(\lambda)d\lambda \qquad \text{Equation (8)}$$

The QE depends on the absorption of light and the collection of charges, thereby, charge recombination leads to a decrease in the QE. Therefore, the recombination at the interface should be minimized to obtain improved QE.

1.2.2   Data Characterization Techniques

1.2.2.1 Light intensity Dependence J_{sc} & V_{oc}

The recombination in the device causes loss of photogenerated charge carriers, which is one of the factors that reduce the J_{SC} and FF of the device. Shockley and Queisser showed that V_{OC} of OSC is at its maximum when the photogenerated charges recombine only radiatively. However, the recombination mechanism in BHJ OSCs is mostly non-radiative which mainly affects OSCs includes monomolecular and bimolecular recombination. So, it is important to understand these recombination mechanisms to improve the performance of OSCs. The monomolecular recombination historically refers to either Shockley-Read-Hall (SRH) recombination or geminate recombination. SRH recombination is a first order recombination process in which one electron and one hole recombine through a trap state or recombination center.[33] The impurities in the donor and acceptor materials and incomplete phase separation which interfacial defects that act as traps are contributed to a trap-assisted recombination. That is, if the electrons are trapped in a short time, they provide a fixed place for the holes to recombine.

The light intensity dependence measurement performed by simply changing the incident light intensity using various neutral density filter. The J-V characteristics were collected while illuminating the solar cells over a range of intensities from 1.4 mW/cm^2 to 100 mW/cm^2. As the incident light intensity decreases, the generated photocurrent also decreases. And at low light intensity, trap sites which present inside the device can more influence on the photocurrent. By fitting J_{SC} vs. light intensity and V_{OC} vs. light intensity, the information of bimolecular recombination and monomolecular (trap-assisted) recombination can be obtained. J_{SC} is proportional to light intensity(I), $J_{SC} \propto I^\alpha$. With log-log scale a plot of J_{SC} vs. light intensity which fit to a power law, if fitting line nearly linear dependence as $\alpha=1$, it means this system is not dominant to bimolecular recombination. On the other hand, it means that carrier losses which originated from bimolecular recombination is existed. V_{OC} is expressed by $\delta V_{OC}=(k_B T/e)$ ln(I), where k_B is the Boltzmann constant, T is the absolute temperature and e is the electron charge. The slope of δV_{OC} vs. ln(I) demonstrates that bimolecular recombination dominates for applied voltages near V_{OC} to light intensity. That is, slope S of V_{OC} versus the logarithm of light intensity being equal to kT/q. If slope of fitting line of V_{OC} vs. light intensity is higher than $k_B T$, it means that additional trap-assisted recombination is existed.[34]

1.2.2.2 Trap Density

The electrical characterization techniques are necessary to understand the factors limiting charge transport in these systems, which is usually limited by the low mobility of charge carriers and by trapping effect of defects. Among the technique, admittance spectroscopy technique has been used for investigation for the density of defect states within the OSCs. Admittance spectroscopy is measuring the contribution of the traps by passing from the low frequency to high frequency. With combine admittance spectroscopy to capacitance voltage measurement, the main electrical characterizations which have been performed on these samples were, *C-V* at room temperature and admittance spectroscopy (*C-f*). The capacitance voltage and admittance spectroscopy measurements were carried out using impedance analyzer (IVIUM Tech., IviumStat) in the frequency range 10^0-10^6 Hz.

In the measurement, the junction capacitance will show a dependence on the measurement frequency. In this case, the measured capacitance frequency dependence $C(\omega)$ is given by Equation (9).

$$C(\omega) = C_d + C_t(\omega) \qquad\qquad \text{Equation (9)}$$

The C_d is the frequency independent depletion capacitance and $C_t(\omega)$ is the frequency dependent contribution of trap level.

The contribution of one single defect level to the capacitance can be given by Equation (10).

$$C(\omega) = C_{hf} + \frac{1}{1+\omega^2\tau^2}(C_{lf} - C_{hf}) \qquad \text{Equation (10)}$$

The C_{hf} is high frequency capacitance which is the depletion capacitance C_d and C_{lf} is the combined contribution of the deep defect and the depletion capacitance. And the contribution of trap C_t is thus given by C_{hf} - C_{lf}, and the dynamics of trap are described by the time constant τ in Equation (11).

$$\tau = (2\omega_0)^{-1}\exp\left(\frac{E}{k_BT}\right) \qquad\qquad \text{Equation (11)}$$

where E is the depth of the state above E_v or below E_c and ω_0 is an attempt-to-escape frequency.

The condition $\omega\tau$=1 determines the trap level E_ω with respect to the valence band maximum is given by Equation (12).

$$E_\omega = kTln\left(\frac{2\omega_0}{\omega}\right) \qquad\qquad \text{Equation (12)}$$

To determine the energetic distribution of traps $N_t(E_\omega)$ from the measured capacitance frequency data $C(\omega, T)$. The trap density of states at energy E_ω is related to the derivative of the capacitance with respect to the frequency as given by Equation (13).

$$N_t(E_\omega) = -\frac{V_{bi}}{qL}\frac{dC}{d\omega}\frac{\omega}{k_BT} \qquad\qquad \text{Equation (13)}$$

The V_{bi} is the built-in voltage and L is the thickness of photoactive layer.[35]

The traps are generally classified as shallow traps, and deep traps for both electron and hole. If traps are very close to the conduction band (LUMO) within energy bandgap, then traps are classified as shallow traps for electrons. Similarly, if traps located around valence band (HOMO) within energy bandgap, then traps are identified as shallow traps for holes. On the other hand, deep traps of electron and holes are existing far away from LUMO and HOMO level, respectively. The trap density according to energy can be calculated from the following equations measured by admittance spectroscopy (*C-V* and *C-f*). By varying the trap energy for frequency-domain analysis of admittance spectroscopy, it is possible to differential between shallow and deep traps for OSCs.

1.2.2.3 Photocurrent Density vs Effective Voltage

From *J-V* characteristics in a wide reverse bias range under 1 sun illumination, by plotted the results using the net photocurrent (J_{ph}) and the dependence on the effective applied voltage (V_{eff}), it gives further understand of the charge extraction process. The exciton generation rate (G_{max}) and exciton dissociation probability (P(E, T)) also can obtain from plotted J_{ph}-V_{eff} results. J_{ph} can expressed by $J_{ph} = J_L - J_D$ and J_L and J_D are the current density under illumination and in the dark, respectively. V_{eff} also expressed by V_{eff}=V$_0$-V and V is the applied voltage and V$_0$ is the voltage at which J$_{ph}$= 0.

If J_{ph} saturated at a large reverse voltage (V_{eff}> 1.5 V), it suggests that all the photogenerated excitons are dissociated into free carriers and all of the carriers are collected at the electrodes without any bimolecular recombination. In this case, saturation current density (J_{sat}), is only limited by the absorbed incident photo flux, N$_{photon}$. This means that the maximum obtainable G$_{max}$ are essentially the same in devices under 1 sun illumination. G$_{max}$ can calculated by J_{sat}=eG$_{max}$L where L is the thickness of the photoactive layer. Using J_{sat}, P(E, T) can obtain to the ratio of J_{ph}/J_{sat}. This ratio is essentially the product of the exciton dissociation efficiency and the charge collection efficiency, a decreased J_{ph}/J_{sat} suggests either a reduced exciton dissociation efficiency or a reduced charge collection efficiency. A reduced charge collection efficiency would suggest that bimolecular recombination begins to dominate. This usually leads to lower FF.[36]

1.3 Interface Engineering

The power conversion efficiency of OSCs is as a result of four processes that occur with the device: generation of excitons, diffusion of excitons to an donor and acceptor interface, generation of holes as a result of charge separation and transport and collection of charge carriers. Apart from these four processes, the quality of the interface materials is another crucial factor to be considered because they are responsible for facilitating good contact. A typical OSC has a light absorbing BHJ between two electrodes. Interface materials are placed between the photoactive layer, donor and acceptor materials, and the electrode materials as shown in **Figure 1.6**. Interfaces play an important role in the maintenance of proper contact between photoactive layers in an organic solar cell. The interfacial layer placed between donor and acceptor materials and the electrode and from interfacial engineering, used to achieve ohmic contact at the organic and metal interface. Also the interfacial layer form a selective contact preventing the oppose charge carriers and excitons from recombining at the electrodes thereby enhancing charge extraction property. In addition, the interface materials act as protective layers which prevent the penetration of substance causing problems in OSC stability.

The electrons and holes separated at the BHJ interface where organic semiconductor donors and acceptor materials are irregularly mixed must reach each electrode efficiently to form an external circuit. To this end, the contact of the organic semiconductor/electrode becomes an important factor that determines the performance of the OSC. The electrical barrier of a few tens of meV of organic semiconductors and metals unfavorable affects OSC characteristics due to significant charge accumulation at the interface and reduction in built-in electric field. Therefore, ohmic contact between each electrode and the organic photoactive layer and selective and efficient charge collection at each electrode are essential. Such methods include the conducting polymers, polymer/polyelectrolytes, fullerene derivatives, or metal oxides.

Another important role of the interfacial layer is to reduce unnecessary energy loss in the OSC structure by matching the energy levels between layers, and to efficiently move charges by increasing the built-in electric field within the device. And to extract. In addition, it is possible to prevent charge recombination occurring at the interface by improving the selective charge collection ability in each electrode, and to form an appropriate morphology of the upper organic photoactive layer by controlling the surface energy of the lower layer. On the other hand, the interfacial layer inserted between the organic photoactive layer/electrode acts as an optical spacer and induces a plasmonic effect to improve exciton generation and charge transport by controlling the optical properties of the organic photoactive layer.

By controlling the energy difference, the V_{OC} is increased, or the collection efficiency of electrons is increased to improve the current density J_{SC} and the FF. There are essential requirements that the interfacial layer must have in an OSC based on a solution process. First, when applying the organic photoactive layer solution, the bottom interfacial layer should not have solubility in the organic solvent. Second, it is necessary to efficiently high light transmittance to the organic photoactive layer. last, the energy level of materials must be considered to enhance the charge transfer capability and charge mobility.[31,37]
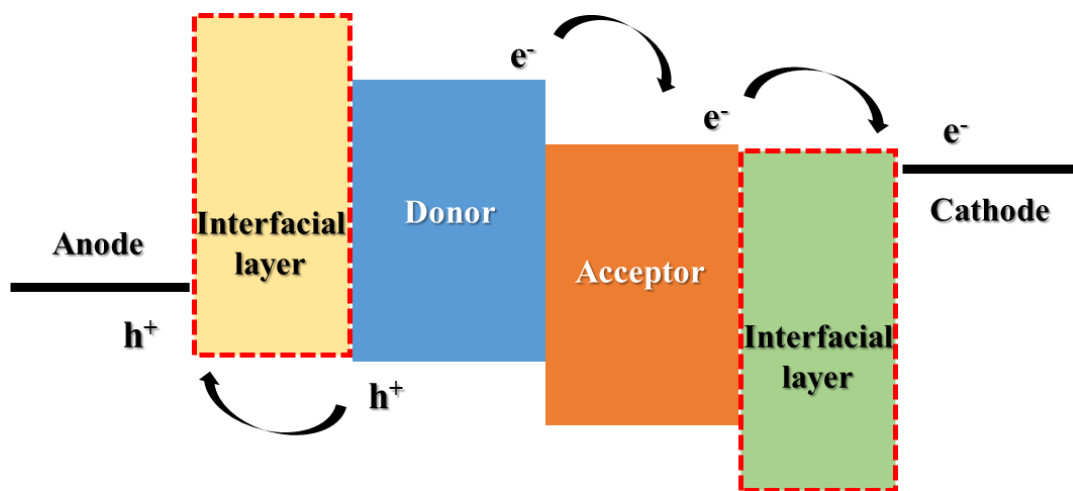
Figure 1.6. Schematic illustration of an OSCs with interfacial layer.

1.3.1 Metal Oxides

First, ZnO is an inorganic n-type semiconductor, it is commonly used in metal oxide cathode interface materials (CIMs) due to it has a property such as low cost, easy synthesis, non-toxicity, high stability, and unique optical/electronic properties. Generally, ZnO materials have a low WF around 4.3 eV, which offers a proper energy level to reduce WF of ITO or metal electrodes, and to match with LUMO levels of various acceptors such as fullerene-based acceptor and non-fullerene acceptor.[38,39] When synthesizing not only ZnO films but also other cathode interface materials, oxygen vacancy may occur depending on the film fabrication condition. By reducing oxygen vacancy through various interface treatments, charge traps can be reduced, and electrical properties can be improved. Therefore, property control of ZnO CIMs to balance their transmittance, electron mobility and interfacial properties, is critical for high performance OSCs.

Zhang et al. applied a bilayer ZnO/CQD as electron extraction layer and it shown that bilayer ZnO/CQD leading to enhanced exciton dissociation, reduced charge recombination and more efficient charge extraction probability, and thereby achieving significant improvement in power conversion efficiency (PCE) of 9.64%.[40] By using a dye to modify inorganic ZnO, Nian et al. reported a highly photoconductive CIM for inverted OSCs. This hybrid CIM was achieved by doping a small amount of light absorber such as PBI-H into a sol-gel-derived ZnO, where the PBI-H molecules could form a N−Zn bond with ZnO during the thermal treatment. As a result, the inverteGod devices based on ZnO:PBIH increased from 8.45% to 10.59% for the PTB7-Th:PC$_{71}$BM system.[41] Moreover, Yu et al. reported that as an ion-liquid of 1-butyl-3-methylimidazolium tetrafluoroborate ([BMIM]BF4) was used to modify ZnO, the [BMIM]BF4-modified ZnO device showed increased J_{SC} and FF as a result of the reduction in the WF of the cathode because the modified ZnO can form spontaneous dipolar polarization at the interface. The PCE of the device using the [BMIM]BF4-modified ZnO CIM was increased to 10.15% in comparison with a PCE of 8.94% for the reference device based on the regular ZnO CIM.[42] By doping the ZnO ripple layer with various metal-carbonate materials, Nho et al. reported the improvement of the performance of the inverted structure organic solar cell. Doping of various metal carbonates in the ZnO ripple layer is formed as a vertical gradient, the work function of the ZnO layer and the LUMO level of PC$_{71}$BM are properly match. So, it induces improvement in device performance, by preventing electron-hole recombination at the interface.[43] Moreover, Wen et al. reported that introduction of four hydroxy (HO) groups into the two perylene bisimide (PBI) bay areas, new HO-PBI ligands were obtained which upon deprotonation can complex Zn^{2+} ions and photosensitize semiconductive zinc oxide thin films. Supported by the photoconductive effect of the ZnO:HO-PBI hybrid interlayers, improved electron collection and transport properties are achieved, leading to remarkable power conversion efficiencies of up to 15.95 %.[44]

Titanium oxide (TiO$_x$) is another n-type metal oxide CIM because it has good optical transparency, relatively high electron mobility, and environmental stability. By solution processing from a sol-gel or spin-coating of TiO$_x$ NPs, TiO$_x$ films were fabricated as effective CIMs for both conventional and inverted OSCs. [45,46] Wang et al. achieved efficient electron transport in OSCs, a transferable GO layer with a WF of 4.3 eV was fabricated by graphene stamping and subsequent oxidation with HNO$_3$. This GO/TiO$_x$ CIM can reduce the series resistance and improve the J_{SC} because of the efficient electron extraction and transport from the photoactive layer to the Al cathode. As a result, the GO/TiO$_x$ CIL-based OSC achieved a PCE of 7.50%. [47] And by hybridizing poly(ethylene glycol) (PEG) with sol-gel TiO$_x$, Yin et al. reported a universal electron transport CIM designed for OSCs based on different polymer blends, where the corresponding device structure, components and energy levels. The hybrid PEG–TiO$_x$ CIM offered advantages of facile solution processability, low annealing temperature (150 °C), low-cost and safety with cheap and environment-friendly raw materials, good interfacial properties. The hybrid PEG-TiO$_x$ CIM can facilitate electron injection and transport by reducing energy barriers between the BHJ layer and ITO, which can be used as a novel class of CIMs for improving electron-collection and reducing interface energy barriers in various BHJ systems. Device performance based on this PEG-TiO$_x$ CIM was greatly improved PCEs up to 9.05%. [48]

In case of MoO$_3$, A MoO$_3$ is an important material as an anode interface material (AIM) owing to its good transparency, high work-function and much better environmental stability compared to PEDOT:PSS. [49] Qin et al. reported that by oxidized MoS$_2$ into a MoS$_2$/MoO$_3$ double-layered film as an AIM, efficient conventional OSCs based on P3HT:PCBM were fabricated with a PCE of 4.15%. [50] Also by using solution-processed MoO$_x$ as the AIM, Tan et al. reported that conventional OSCs based on P3HT:IC$_{70}$BA showed better photovoltaic properties with a PCE of 6.57% and longer lifetime compared to the OSCs with a PEDOT:PSS AIM. It was revealed that the oxygen vacancy of the transition metal oxide played an important role in the electronic property, and the oxygen level could be controlled to improve the device performance. [51]

1.3.2   Conjugated Polyelectrolytes (CPEs)

These materials can efficiently adjust the WF of cathodes by forming an interfacial dipole between the cathode and the active layer, benefiting the charge transport. Due to their ambient solution processibility, a lot of water/alcohol soluble conjugated polymers were designed as CIMs or AIMs for efficient electron or hole injection/transport in OSCs. By introducing thin poly[(9,9-bis(3′-(N,N-dimethylamino)propyl)-2,7-fluorene)-alt-2,7-(9,9-dioctylfluorene)] (PFN) as CIM, He et al. reported simultaneously enhance V_{OC}, J_{SC}, and FF in conventional OSCs, leading to an increase in PCE from 5.0%

to 8.37%. The improved performance upon the use of PFN were ascribed to multiple functionalities of the CIM, including enhanced built in potential across the device due to the existed interface dipole improved electron transporting properties.[52] Li et al. reported that fullerene derivatives such as fulleropyrrolidinium iodide (FPI), were blended with ethoxylated polyethyleneimine (PEIE) can improve their conductivity and WF tunability of the hybrid FPI-PEIE CIMs. Using solution-processed FPI-PEIE as CIMs, high PCEs up to 9.62% were achieved in inverted OSCs.[53] Amine containing polymer polyethyleneimine (PEI) has been used to produce electron-collecting interface in fullerene solar cells. But high-performance non-fullerene acceptors tend to react with PEI. The reaction destroys their chemical and electronic structure of the acceptor and results in poor performance. By using a robust low-work function interlayer of Zinc ion (Zn^{2+}) chelated PEI (PEI-Zn), Zhou et al. reported for efficient non-fullerene OSCs. Simultaneously, the chelation of Zn^{2+} with the PEI reduces the chemical reactivity of PEI, and therefore the reaction between the PEI and the non-fullerene active layer is suppressed. The PEI-Zn can work efficiently as the interlayer of electron injection layer with PCE of 13.3%.[54] A series of PFS derivatives with π-conjugated 5-(9H-fluoren-2-yl)-2,2′-bithiophene(fluorene-alt-bithiophene) backbones, namely PFS-4C containing alkyl sulfonate pendants of alkyl side chains reported by Zhang et al. Based on the PBDB-T:ITIC active layer, devices were fabricated using PFS-4C as AIMs. PFS-4C has a proper HOMO level of 5.15 eV, which is beneficial to reduce the hole collection energy barrier of the anode, and the superior performance with a PCE of 10.54% was achieved.[55]

1.3.3 Conducting Polymer

Poly(3,4-ethylenedioxy-thiophene):poly(styrenesulfonate) (PEDOT:PSS) is the most widely used anode interface material in organic solar cells because it has excellent electrical properties and is soluble in water, so the process is simple. Many studies have been reported to improve the efficiency of solar cells by improving this PEDOT:PSS. The proper WF of PEDOT:PSS (~5.1 eV) matches well with many polymer donors to form good ohmic contact at the anode and photoactive layer interface.[56-58] So far extensive studies have been carried out to improve the performance of PEDOT:PSS AIMs. By embedding core-shell Au@Ag nanocomposites in PEDOT:PSS as an AIM, Zheng et al. showed improved the efficiency of solar cells using scattering light through localized surface plasmon resonance. Using this point, metal nanoparticles are mixed with PEDOT:PSS to achieve an efficiency of 8.31% to 9.19%.[59] Also an Ag nanowires (Ag NWs)/PEDOT:PSS composite was prepared by a facile solution-processing method and employed as AIM reported by Peng et al., which showed PCE up to 13.53%. The Ag NWs/PEDOT:PSS Simultaneous enhanced short-circuit current and fill factor, in comparison

to the case of the pristine PEDOT:PSS. Due to the improved electrical conductivity of Ag NWs/PEDOT:PSS composites accompanied by the increased work function for a better matching with the ITO electrode, charge transfer facilitated increased and charge recombination reduced at the anode and photoactive interface.[60] By incorporating a photo-crosslinking agent into a PEDOT:PSS film, Ha et al. demonstrated a water resistant PEDOT:PSS HTL, which combination of the crosslinking system and methanol surface treatment simultaneously improved the device efficiency and stability of OSCs. The crosslinking system inside PEDOT:PSS changed its intrinsic water-soluble characteristic into a water-resistant property, thus preventing water penetration into the PEDOT:PSS film. In addition, methanol treatment improved the surface conductivity and reduced the surface roughness of the PEDOT:PSS film by removing surface residues of PDAs and insulating PSS parts.[61] Wang et al. reported 2D α-In$_2$Se$_3$ nanosheets with high conductivity and suitable work function synthesized by liquid-phase exfoliation method. α-In2Se3 nanosheets are directly added into PEDOT:PSS to obtain the PEDOT:PSS:α-In$_2$Se$_3$ composite film. The PEDOT:PSS:α-In$_2$Se$_3$ composite film exhibits excellent optical transmittance, suitable work function, and enhanced conductivity. The devices with the PEDOT:PSS: α-In$_2$Se$_3$ CIM showed enhanced PCEs of 11.22%, mainly attributed to the high J_{SC} and FF.[62] By adding graphitic carbon nitride (g-C$_3$N$_4$) into the PEDOT:PSS, Li et al. reported the g-C$_3$N$_4$ as a Bronsted base can be protonated, weakening the shield effect of insulating PSS on conductive PEDOT, which enables exposures of more PEDOT chains on the surface of PEDOT:PSS core-shell structure, and thus increasing the conductivity. Therefore, at the interface between g-C$_3$N$_4$ doped HTL and PBDB-T-2F:Y6 layer, the charge transport is improved, and the charge recombination is suppressed, leading to boosting the PCE from 15.29% to 16.38%.[63] And also by doping of PEDOT:PSS with dopamine hydrochloride (DA·HCl) which reacts with the redundant sulfonic acid of PSS (PEDOT:PSS-DA), Cao et al. reported that the PEDOT:PSS-DA film exhibits enhanced work function and conductivity compared to prisitne of PEDOT:PSS. PEDOT:PSS-DA-based devices showed a PCE of 16.55% which provides an efficient modification strategy via doping the compounds with amino derivatives into PEDOT:PSS to enhance the performance of PEDOT:PSS in OSCs.[64]

The various methods were applied to CIM and AIM to realizing a highly efficient OSCs. The contents of each category are summarized in **Table 1.1** for each device structure and device parameters.

Table 1.1. Device characteristics of some representative OSCs with different CIMs and AIMs.

OSC type	Cathode configuration	Active layer	Anode configuration	V_{OC} [V]	J_{SC} [mA/cm²]	FF [%]	PCE [%]
Inv.	ITO/ZnO/CQD	PTB7:PC$_{71}$BM	MoO$_3$/Ag	0.75	19.60	66.4	9.64
	ITO/ZnO:PBI-H	PTB7-Th:PC$_{71}$BM	MoO$_3$/Ag	0.82	17.69	72.9	10.59
	ITO/ZnO/[BMIM]BF4	PTB7-Th:PC$_{71}$BM	MoO$_3$/Ag	0.78	17.70	73.5	10.15
	ITO/ZnO/Li$_2$CO$_3$	PTB7:PC$_{71}$BM	MoO$_3$/Ag	0.73	18.93	73.0	10.08
	ITO/ZnO:HO-PBI	PBDB-T-2F:Y6	MoO$_3$/Ag	0.83	25.34	74.8	15.73
	GO/TiO$_X$/Al	PCDTBT:PC$_{71}$BM	ITO/PEDOT:PSS	0.88	12.40	68.0	7.50
	ITO/PEG-TiO$_X$	PTB7-Th:PC$_{71}$BM	MoO$_3$/Ag	0.79	17.40	65.6	9.05
	ITO/PFN	PTB7-Th:PC$_{71}$BM	MoO$_3$/Al	0.83	17.43	73.8	10.61
	ITO/FPI-PEIE	PBDTT-TT:PC$_{71}$BM	MoO$_3$/Ag	0.80	16.15	72.0	9.62
	ITO/PEI-Zn	PBDB-T-2F:IT-4F	MoO$_3$/Ag	0.84	20.80	76.0	13.30
Con.	PFN-Br/Ca/Al	PBDB-T:ITIC	ITO/PFS-4C	0.93	16.74	67.8	10.52
	Al	P3HT:PCBM	FTO/MoS2/MoO$_3$	0.63	9.90	67.1	4.15
	Ca/Al	P3HT:IC$_{70}$BA	ITO/s-MoO$_3$	0.84	11.09	70.5	6.57
	TiO$_x$/Al	PTB7:PC$_{71}$BM	ITO/PEDOT:PSS+ Ag@Au	0.75	17.50	70.0	9.19
	Al	PTB7-Th:PC$_{71}$BM	ITO/PEDOT:PSS+ PDA(MeOH)	0.72	17.40	59.0	7.71
	PDINO/Al	PBDB-T-2Cl:IT-4F	ITO/Ag Nws /PEDOT:PSS	0.87	20.76	75.0	13.53
	PFN-Br/Al	PBDB-T:ITIC	PEDOT:PSS:α-In$_2$Se$_3$	0.91	17.31	71.1	11.22
	PFN-Br/Ag	PBDB-T-2F:Y6	ITO/PEDOT:PSS:g-C$_3$N$_4$	0.84	26.71	73.0	16.38
	PNDIT-F3N/Ag	PBDB-T-2F:Y6	ITO/PEDOT:PSS-DA	0.85	25.66	72.1	15.62

Chapter 2. Treating the Poly(3,4-ethylenedioxythiophene):Poly(styrene-sulfonate) Surface with Hydroquinone Enhances the Performance of Polymer Solar Cells

This chapter is reproduced in part with permission of "ACS Applied Materials & Interfaces, Vol. 10, pages 41578-41585". Copyright 2018, American Chemical Society.

2.1 Research Background

Polymer BHJ solar cells have attracted much attention for their potential applications in large-area flexible devices because they are lightweight, low cost, and simple to fabricate.[65-69] Since the first report on polymer BHJ solar cells in 1995,[6] substantial progress has been made, raising device efficiencies by more than 13% through improvements in the design and synthesis of active materials,[70-73] the optimization of nanoscale morphology,[74-76] and interface engineering.[43,77-80] Of course, the most important component in high efficiency solar cells is high performing active materials, but developing new and better active materials requires a lot of time and effort. Therefore, a cost-effective approach to improving the performance of existing materials is maximizing charge collection efficiency through interface engineering.

The insertion of an electron or hole transport layer is part of interface engineering in a broad sense. Numerous organic and inorganic materials that could function as hole and electron extraction layers have been developed and studied to enhance the performance of BHJ solar cells.[81-85] The most widely used inorganic buffer layer materials are probably metal oxides. A variety of transition metal oxides, such as ZnO, TiO_2, NiO and MoO_3 have been developed as either hole or electron transport materials for fabricating high performance and cost-effective BHJ solar cells due to their advantages of environmental stability, high transparency and high carrier mobility.[86-88] Organic-based buffer materials are much more diverse. Dozens of novel synthetic materials which can be classified in conjugated polyelectrolyte,[89,90] small molecule transport materials,[91,92] polymer buffer materials,[93,94] etc., have been developed and successfully applied as a buffer layer in BHJ solar cells. Among the organic-based hole transport materials, however, poly(3,4-ethylenedioxy-thiophene):poly(styrenesulfonate) (PEDOT:PSS) remains the most widely used material even though it is the oldest. In early studies of organic BHJ solar cells, PEDOT:PSS offered superior performance in many ways. First, PEDOT:PSS showed excellent hole extraction because of a well-matched work function (~5.1 eV) for the highest occupied molecular orbital (HOMO) level of the donor polymer.[95-97] Second, PEDOT:PSS delivered better adhesion

between the inorganic ITO electrode and the organic active layer.[98,99] In addition, PEDOT:PSS induced uniform deposition of the active layer by smoothing the ITO surface.[100] Now, various hole transport materials have been newly developed and used to replace PEDOT:PSS in BHJ solar cells. Nonetheless, PEDOT:PSS is still the best hole transport material in terms of process simplicity and performance consistency. In fact, PEDOT:PSS is the standard hole transport material; the performance of each newly developed hole transport material is judged by whether it is better or worse than PEDOT:PSS.

Until now, interface engineering for organic BHJ solar cells has focused mainly on problems that occur at the interface between the organic active layer and the charge transport layer, which uses a metal-oxide such as ZnO, TiO$_2$, or MoO$_3$. In solar cells with a metal-oxide charge transport layer, many surface treatment methods, such as polar solvent treatment,[101,102] surface doping,[103-106] or the insertion of a thin conjugated polyelectrolyte layer,[107,108] are applied to improve the interfacial properties between the inorganic metal-oxide layer and the organic BHJ layer. However, the literature contains only a few reports of surface treatments for the PEDOT:PSS hole transport layer. Recently, surface modifications of PEDOT:PSS were reported by adding a p-type dopant[109] or treating it with either an alcoholic polar solvent[110,111] or a high boiling point solvent.[112] However, those studies focused on increasing the conductivity of PEDOT:PSS. Furthermore, most studies about modifying the PEDOT:PSS surface have considered only inverted planar perovskite solar cells, which have interfacial problems between the inorganic metal-oxide transport layer and organic active layer similar to those in organic BHJ solar cells. Although several investigations have considered the interfacial problem between PEDOT:PSS and the active layer in organic BHJ solar cells,[113-115] it is true that the interfacial problem between PEDOT:PSS and the active layer was much less considered compared to the interfacial problem between metal oxides and the active layer, probably, because PEDOT:PSS was itself understood to be a modifying material for the ITO surface.

Conventionally, single-layer BHJ cells, which have a cathode/active/anode structure, were treated as metal-insulator-metal diodes. However, a careful investigation of dark current found that the fundamental unit is a semiconductor–metal Schottky junction.[116-118] Because PEDOT:PSS also has a metallic property (though with relatively low conductivity),[119,120] it still carries the possibility of forming a Schottky-type contact barrier at the interface. Therefore, in this work, we have modified the PEDOT:PSS surface with hydroquinone (HQ) by spin-coating to reduce the Schottky-type contact barrier that can interfere with hole transport. The conjugated polymer is an electron-rich system, and ultraviolet photoelectron spectroscopy (UPS) measurements showed that PEDOT:PSS and the conjugated polymer form an n-type Schottky contact. Surface treatment of PEDOT:PSS with HQ changed the energy level bending properties in a direction more favorable to hole extraction. In addition,

2 4

HQ treatment significantly reduced surface resistivity. Those HQ-derived surface property improvements nearly doubled the density of the extracted holes. Consequently, a PCE of up to 10.18% was achieved from a conventionally structured BHJ solar cell using poly[[4,8-bis[5-(2ethyl-lhexyl)thiophen-2-yl]benzo[1,2-b:4,5-b0]dithiophene-2,6-diyl][3-fluoro-2-[(2-ethylhexyl)carbo-nyl]thieno[3,4-b]thiophenediyl]] (PTB7-Th) and [6,6]-phenyl-C71-butyric acid methyl ester (PC$_{71}$BM) as the active layer, a ~28% increase in efficiency compared to solar cells without HQ treatment.

2.2 Experimental

Device fabrication: ITO substrates were cleaned with detergent and ultrasonicated in acetone and IPA for 15 min each. A hole transport layer of PEDOT:PSS (Clevios PH) was spin-coated at 4000 rpm for 40 s after UV-ozone surface treatment and annealed at 150 °C for 10 min. The thickness of the PEDOT:PSS was 40–50 nm. Solutions with between 0.2 wt% and 2 wt% of HQ in IPA were spin-coated on top of the PEDOT:PSS layer at 5000 rpm for 40 s and annealed at 100 °C for 10 min. The substrates were then transferred to a N$_2$-filled glovebox. The active layer solution was made with a 1:1.5 ratio of PTB7-Th and PC$_{71}$BM in chlorobenzene with 3% DIO as a processing additive to get a better phase-separated morphology. The prepared solution was stirred overnight. The active layer was deposited on top of the PEDOT:PSS layer by spin-coating at 1000 rpm for 60 s and then annealed at 80 °C for 10 min. A ZnO nanoparticle solution (2.5 wt% in IPA) diluted to an IPA ratio of 1:10 was spin-coated at 3000 rpm for 30 s on top of the PTB7-Th:PC$_{71}$BM layer as an electron transport layer, and it was then annealed at 80 °C for 10 min. Finally, 100 nm of aluminum was deposited by thermal evaporation at a vacuum condition of 2×10^{-6} Torr. The device area is 0.13 cm^2.

Device characterization: The power conversion efficiencies of the organic solar cells were measured by *J-V* curves using a Keithley 2401 source measurement unit under AM 1.5G 100 mW/cm^2 spectra from a solar simulator (Newport Co., Oriel). To calibrate the intensity of the solar simulator, a standard Si-photodiode detector with a KG-3 filter (Newport Co., Oriel) was used. The EQE was measured using a quantum efficiency measurement system solar cell spectral response/QE/IPCE (Newport Co., Oriel IQE-200B). The light intensity at each wavelength was calibrated using a standard, single-crystal Si photovoltaic cell. The absorption spectra of the device films were measured by a UV/Vis spectrophotometer (Varian, Cary5000).

The surface properties and morphologies of pristine PEDOT:PSS, HQ-modified PEDOT:PSS, and PTB7-Th:PC$_{71}$BM films were characterized by AFM (NanoNavi II, SII Nano Technology Inc.) in the

tapping mode. The current levels of the pristine PEDOT:PSS and HQ-modified PEDOT:PSS were measured using a C-AFM system (HITACHI NanoNavi E-Sweep) with +3V applied on the ITO bottom electrode under dark conditions. The pristine PEDOT:PSS film was fabricated by spin-coating PEDOT:PSS at 4000 rpm for 40 s on an ITO substrate, and the HQ-modified PEDOT:PSS film was further coated with 1 wt% HQ solution. IS measurements were taken using an impedance analyzer (IVIUM Tech., IviumStat) under dark conditions at an open circuit voltage in the frequency range between 0.1 Hz and 1.0 MHz. CE was conducted using the CE analyzer function of an organic semiconductor parameter test system (McScience T4000) under 1.0 sun at V_{oc} conditions. To determine the valence band and work function of pristine PEDOT:PSS and HQ-modified PEDOT:PSS, UPS measurements were carried out with an ESCALAB 250-XI surface analysis system equipped with a He-discharge lamp providing He-I photons of 21.22 eV. The XPS investigation used a monochromatic Al-Kα X-ray gun with a photon energy of 1486.6 eV. The base vacuum pressure of the analysis system was ≈10^{-7} Torr. The Fermi edge was calibrated using a clean Au film, and all spectra presented were plotted with respect to the determined Fermi level. All XPS measurements were calibrated with reference to the Au 4f7/2 core level (83.98 eV) of a freshly deposited Au film. The measured samples were prepared by spin coating a PTB7-Th solution of 0.003 to 0.3 wt% on both pristine PEDOT:PSS and HQ-modified PEDOT:PSS films. The surface conductivity of pristine PEDOT:PSS and HQ-modified PEDOT:PSS was determined using a hall effect measurement system (Ecopia model No. HMS-5000). The thickness of the film was measured using a Dektak XT surface profiler. These samples were fabricated in the same way as the AFM samples. Mid-IR absorption spectra from pristine PEDOT:PSS and HQ-modified PEDOT:PSS were measured using an FTIR spectrometer (Varian, Varian 670). These samples were fabricated in the same way as the AFM samples, except ZnSe was used as the substrate.

2.3 Results and Discussion

Figure 2.1a shows a schematic of the conventional BHJ solar cell architecture and the chemical structures of the materials used in this study (PTB7-Th, PC$_{71}$BM, PEDOT:PSS, and HQ). HQ treatment was simply done by spin-coating HQ solution diluted with isopropyl alcohol (IPA) on the PEDOT:PSS layer. HQ is weak polar solvent with a dipole moment of 1.4 Debye. Its effects are similar to those of alcoholic solvents such as methanol and ethanol, which are often used for surface treatment,[110,111,121] because they all have two hydroxyl groups (-OH). Because HQ has a high boiling point (287 °C), it combines the effects of an alcoholic polar solvent and a high boiling point solvent. Furthermore, HQ can lose an H$^+$ from one of the hydroxyls to form a monophenolate ion or lose an H+ from both to form a diphenolate ion. Therefore, we expected HQ to provide additional protonation doping on the PEDOT:PSS surface. **Figure 2.1b** shows the energy level diagrams of each material used in our PTB7-Th:PC$_{71}$BM solar cells. The work-function of the HQ-treated PEDOT:PSS was determined by UPS measurement as shown **Figure 2.2**. Other energy level values, such as the HOMO/LUMO level of active materials and conduction band minimum level of the ZnO nanoparticles, were obtained from the literature.
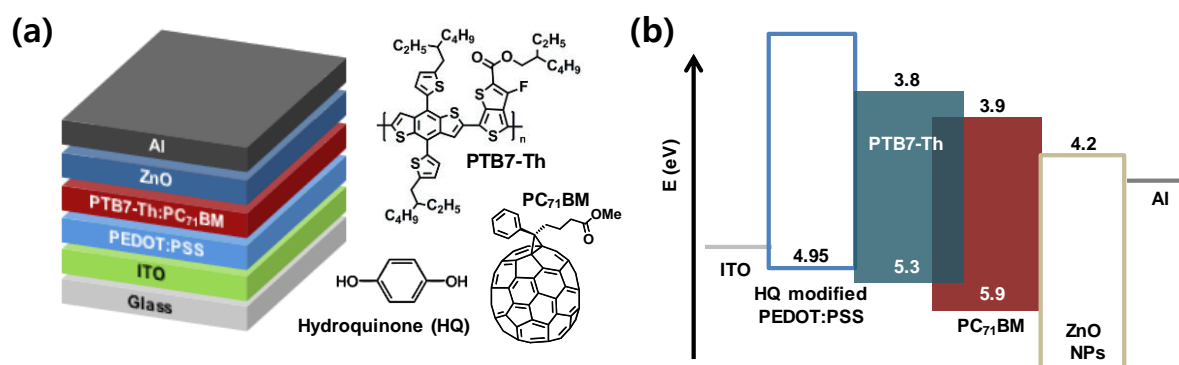
Figure 2.1. (a) Schematic illustration of the device structure and chemical structure of the photoactive materials (donor: PTB7-Th, acceptor: PC$_{71}$BM) and hydroquinone (HQ) surface modifier for PEDOT:PSS, (b) Energy level diagram of a BHJ solar cell based on a PTB7-Th:PC$_{71}$BM blend.
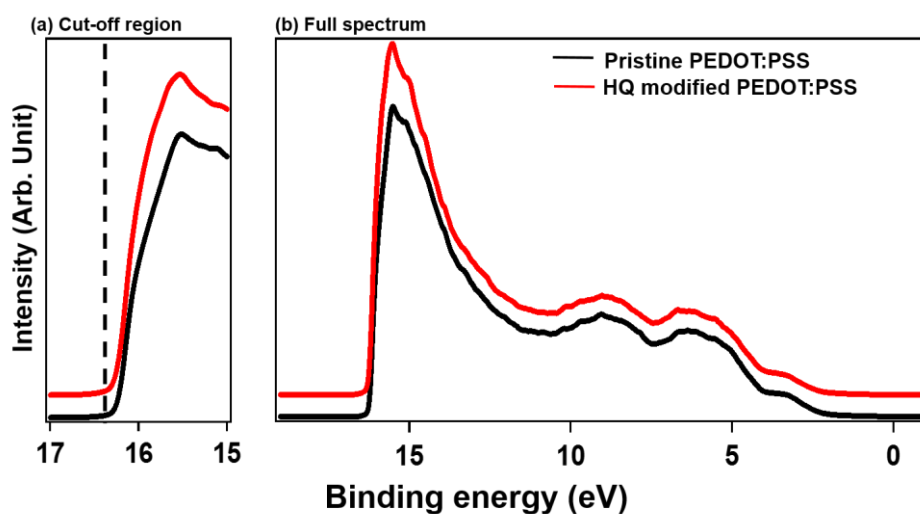
Figure 2.2. UPS spectra of pristine PEDOT:PSS and modified PEDOT:PSS on ITO.

Figure 2.3a shows the current density (J)-voltage (V) characteristic curves of conventionally structured PTB7-Th:PC$_{71}$BM solar cells. Details of the performance of these solar cells are listed in **Table 2.1**. To find the proper dilution ratio for the HQ solution, we varied the ratio of HQ to IPA from 0.2 wt% to 2.0 wt%. Solar cells with a pristine PEDOT:PSS layer (without HQ treatment) yielded a PCE of 7.98% with a J_{sc} of 15.6 mA/cm^2, a V_{oc} of 0.782 V, and a fill factor (FF) of 0.654. The performance of solar cells with an HQ-modified PEDOT:PSS layer gradually increased along with the HQ concentration up to 1.0 wt%. The most efficient solar cell had a PCE of 10.2%, with a J_{sc} of 18.9 mA/cm^2, a V_{oc} of 0.793 V, and an FF of 0.680. However, when the HQ concentration exceeded 1.0 wt%, cell efficiency decreased rapidly. Since we have used HQ solution diluted with alcohol solvent such as methanol or ethanol, it has possibility that this performance enhancement may originated by alcohol solvent because alcohol solvent also can modify the PEDOT:PSS surface a little. However, the performance increase was not observed when the PEDOT:PSS surface was treated with a simple alcohol solvent. Thus, the performance enhancement was obviously an effect of the HQ. In addition, the performance enhancements from the HQ treatment were universal (clearly observable in other polymer BHJ systems).
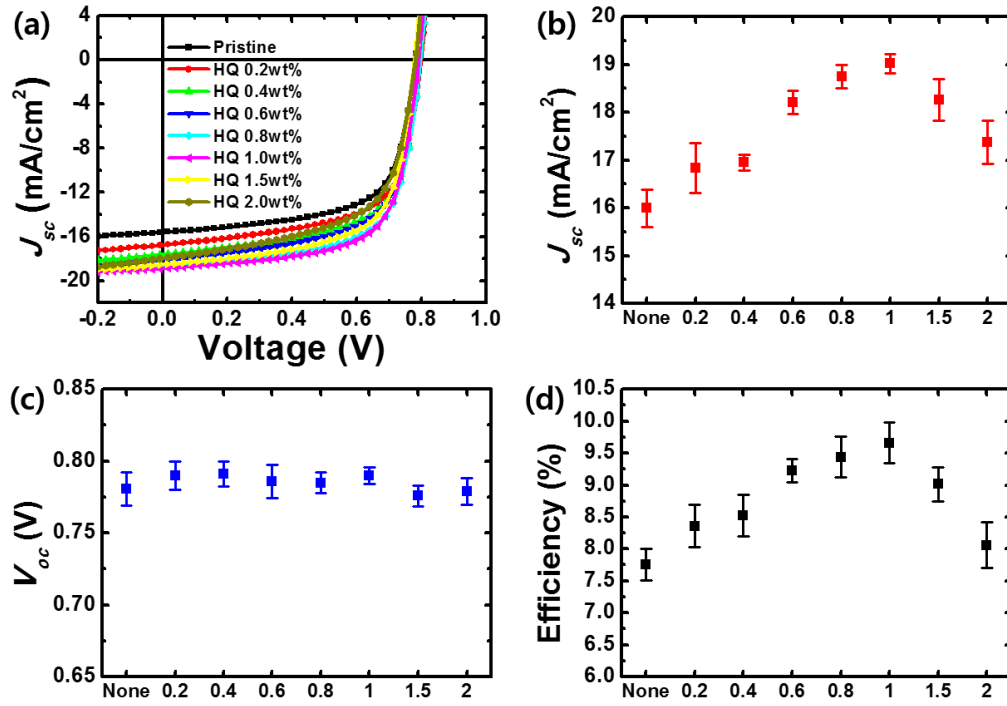
Figure 2.3. (a) *J-V* characteristics of PTB7-Th:PC$_{71}$BM solar cells with pristine PEDOT:PSS and PEDOT:PSS modified with various ratios of HQ. (b) *J$_{sc}$*, (c) *V$_{oc}$*, and (d) PCE distributions for the solar cells with pristine PEDOT:PSS and PEDOT:PSS modified with various ratios of HQ. The data were obtained from 20 devices for each case.

Table 2.1. Summarized device performance characteristics of PTB7-Th:PC$_{71}$BM solar cells with pristine PEDOT:PSS and PEDOT:PSS modified with various amounts of HQ.

concentration	V_{oc} (V)	J_{sc} (mA/cm^2)	J_{sc-EQE}[§] (mA/cm^2)	FF	η (%)	η_{ave*} (%)	R_s (Ω/cm^2)	R_{sh} (Ω/cm^2)
Pristine	0.782	15.6	15.4	0.654	7.98	7.87	4.03	509
HQ 0.2wt%	0.798	16.8	15.7	0.658	8.82	8.63	4.33	372
HQ 0.4wt%	0.795	17.6	16.2	0.657	9.19	9.06	3.95	339
HQ 0.6wt%	0.792	18.1	16.3	0.649	9.30	9.23	3.81	347
HQ 0.8wt%	0.796	18.6	17.1	0.681	10.1	9.95	4.01	477
HQ 1.0wt%	0.793	18.9	17.4	0.680	10.2	10.1	3.81	518
HQ 1.5wt%	0.779	18.5	17.1	0.639	9.21	9.16	3.31	382
HQ 2.0wt%	0.781	17.9	16.4	0.611	8.54	8.48	3.84	251

*Average PCE values were obtained from 20 devices.
[§] *J$_{sc}$* values calculated from EQE measurements.

Figure 2.4 show the *J-V* characteristic results from poly(3-hexylthiophene) (P3HT) and [6,6]-phenyl-C61-butyric acid methyl ester ($PC_{61}BM$), poly[[4,8-bis[(2-ethylhexyl)oxy]benzo[1,2-b:4,5-b']dithiophene-2,6-diyl][3-fluoro-2-[(2-ethylhexyl)-carbonyl]-thieno-[3,4-b]thiophenediyl]] (PTB7) and $PC_{71}BM$ respectively. Note that the optimal HQ concentration varied a bit depending on the BHJ active material. The device with the PTB7:$PC_{71}BM$ mixture showed the highest efficiency at the same optimal dilution ratio of HQ and IPA as the PTB7-Th:$PC_{71}BM$ device, whereas the P3HT:$PC_{61}BM$ device showed the best efficiency at 0.8 wt%. Details of the performance of these solar cells are listed in **Table 2.2 and 2.3**.
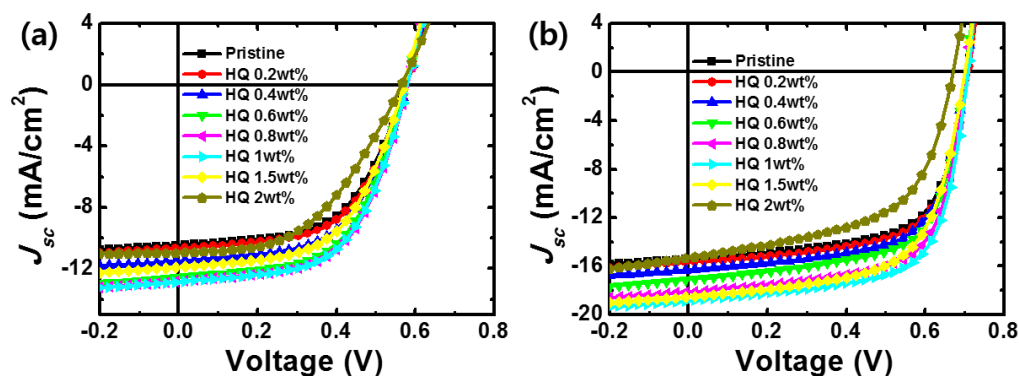
Figure 2.4. *J-V* characteristics of (a) P3HT:PCBM and (b) PTB7:$PC_{71}BM$ solar cells with pristine PEDOT:PSS and HQ modified PEDOT:PSS with various HQ ratios

Table 2.2. Summarized device performance characteristics of P3HT:PCBM solar cells with pristine PEDOT:PSS and HQ modified PEDOT:PSS with various ratios.

	V_{OC} (V)	J_{SC} (mA/cm^2)	FF	η (%)
Pristine PEDOT:PSS	0.576	10.4	0.553	3.31
HQ 0.2wt%	0.579	10.7	0.558	3.46
HQ 0.4wt%	0.577	11.5	0.556	3.69
HQ 0.6wt%	0.576	12.6	0.559	4.06
HQ 0.8wt%	0.580	12.8	0.568	4.22
HQ 1wt%	0.581	12.9	0.561	4.20
HQ 1.5wt%	0.572	11.9	0.543	3.70
HQ 2wt%	0.566	11.0	0.464	2.89

Table 2.3. Summarized device performance characteristics of PTB7:PC$_{71}$BM solar cells with pristine PEDOT:PSS and HQ modified PEDOT:PSS with various ratios.

	V_{OC} (V)	J_{SC} (mA/cm^2)	FF	η (%)
Pristine PEDOT:PSS	0.706	15.4	0.648	7.04
HQ 0.2wt%	0.710	15.7	0.652	7.27
HQ 0.4wt%	0.702	16.3	0.646	7.39
HQ 0.6wt%	0.701	17.1	0.645	7.73
HQ 0.8wt%	0.701	18.1	0.660	8.37
HQ 1wt%	0.708	18.8	0.665	8.85
HQ 1.5wt%	0.702	18.5	0.624	8.10
HQ 2wt%	0.671	15.3	0.533	5.47

As clearly shown in the $J\text{-}V$ results, the PCE enhancement in devices with HQ treatment stemmed from improvements in J_{sc}. In an organic BHJ solar cell, factors that significantly influence J_{sc} are improvements in the charge extraction efficiency through energy level changes or morphology changes at the interface. First, to investigate the influence of HQ treatment on energy level changes in both the PEDOT:PSS and PTB7-Th donor polymer, we performed UPS measurements, as shown in **Figure 2.5a**. To observe the band bending degree of the PTB7-Th polymer caused by the change in the PEDOT:PSS surface properties, we measured the UPS with various thicknesses of PTB7-Th polymer, which we controlled by changing the solution concentration from 0.003 wt% to 0.3 wt%. When PTB7-Th was deposited on pristine PEDOT:PSS, the secondary edges shifted toward higher binding energies as the concentration of the PTB7-Th solution increased. The total vacuum level (VL) shift at the saturated coverage was 0.25 eV for PTB7-Th deposited on pristine PEDOT:PSS and 0.35 eV for PTB7-Th deposited on HQ-treated PEDOT:PSS. The right side of the figure shows the evolution of the HOMO onsets for PTB7-Th. **Figures 2.5c and 2.5d** show the C 1s and S 2p emission lines from the PTB7-Th layers on PEDOT:PSS. These XPS analyses show the energies of the core levels, allowing us to probe the band bending. As the concentration of PTB7-Th solution increased to 0.3 wt%, the S 2p emissions increased in intensity, and the PSS emissions became attenuated because of the thicker PTB7-Th layer. Using that S 2p and C 1s peak shift between the thin and thick PTB7-Th layers, we determined the band bending energies: 0.28 eV for PTB7-Th on pristine PEDOT:PSS and 0.32 eV for the PTB7-Th on PEDOT:PSS with HQ treatment. **Figures 2.5e and 2.5f** show energy level diagrams obtained by summarizing the UPS and XPS results. The hole injection barrier (φ_h) was estimated using the energy difference between the E_F and HOMO levels extracted from the UPS results. Although the band bending degree of PTB7-Th on the HQ-treated PEDOT:PSS was slightly larger than that of PTB7-Th on pristine PEDOT:PSS, the φ_h of the PTB7-Th on the HQ-treated PEDOT:PSS was smaller than on pristine PEDOT:PSS. Thus, in terms of hole transport, HQ treatment improved the interfacial contact barrier and facilitated hole transfer.
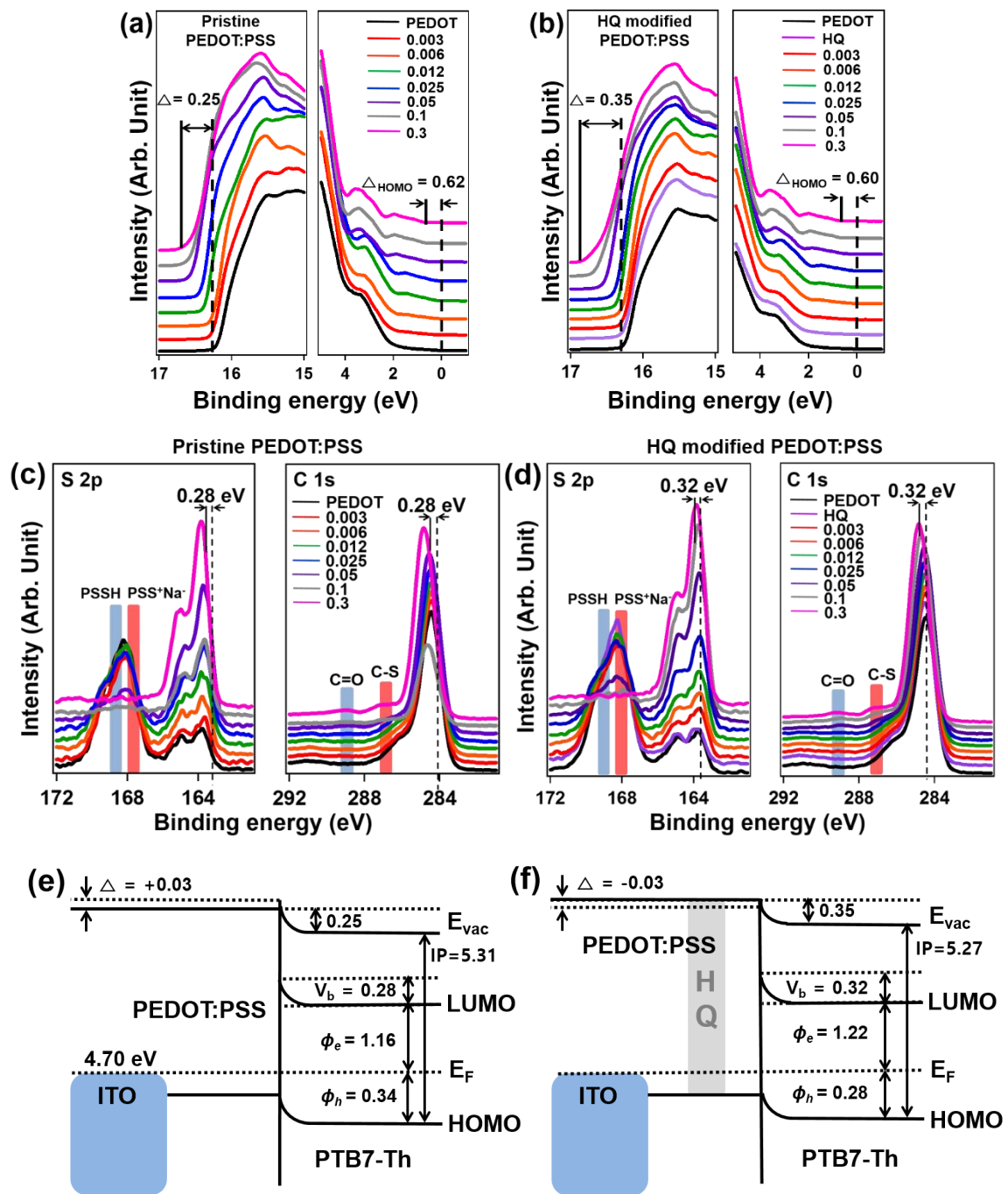
Figure 2.5. Secondary electron cut-off and HOMO onset UPS spectra of (a) pristine PEDOT:PSS and (b) HQ-modified PEDOT:PSS with increasing concentrations of PTB7-Th. The XPS spectra for S 2p and C 1s of (c) pristine PEDOT:PSS and (d) HQ-modified PEDOT:PSS with increasing concentrations of PTB7-Th. Schematic energy-level diagrams of PTB7-Th on (e) pristine PEDOT and (f) HQ-modified PEDOT:PSS. The energy unit is eV. (E_F: Fermi energy level, E_{vac}: Vacuum level, Δ: Interfacial dipole, IP: Ionization potential, V_b: Energy level relaxation, φ_e: Electron injection barrier, φ_h: Hole injection barrier).

3 3

The effect of the energy level change from HQ treatment was consistently confirmed in several experiments, as shown in **Figure 2.6**. After HQ treatment, although the hole extraction barrier was reduced, the electron injection barrier became larger. Normally, electrons injected from the anode electrode generate undesirable leakage current. Within the operation range between 0 V and V_{oc}, the flow of leakage current is opposite to the photocurrent, thereby reducing the device efficiency. Therefore, we expected that the enlarged electron injection barrier created by the HQ treatment would reduce the leakage current, and indeed we found significantly reduced leakage current in the device with HQ-modified PEDOT:PSS, as shown in the *J-V* characteristics measured under dark conditions (**Figure 2.6a**). The effect of reducing the interfacial contact barrier by HQ treatment was confirmed by impedance spectroscopy (IS), which is a useful method for analyzing the interfacial transport and recombination properties of solar cells. **Figure 2.6b** shows the Nyquist plots of the IS results measured under illumination at V_{oc}. Devices both with and without HQ treatment appear on one semicircle without a transmission line (TL). The absence of the TL indicates that solar cells with and without HQ treatment can be interpreted using the Gerischer impedance model.[122,123] Because neither transport resistance nor recombination resistance can be unambiguously determined in the Gerischer impedance model, only relative comparisons are possible, and the combined effective resistance is called Gerischer resistance. Because all device fabrication parameters were identical for both solar cells (except for the HQ treatment of the PEDOT:PSS surface), the difference in the IS spectra likely originated from that interface modification. The real impedance decreased significantly in the device with the HQ-modified PEDOT:PSS, which indicates that the surface modification improved the interfacial contact. The enhanced charge extraction (CE) property from the HQ treatment was confirmed by measurement, as shown in **Figure 2.6c**. Using the CE measurement, we calculated the charge extraction density directly, as shown in **Figure 2.6d**. Direct comparison between the devices with and without HQ treatment indicated that the device with HQ treatment had almost double the charge extraction density of the untreated device.
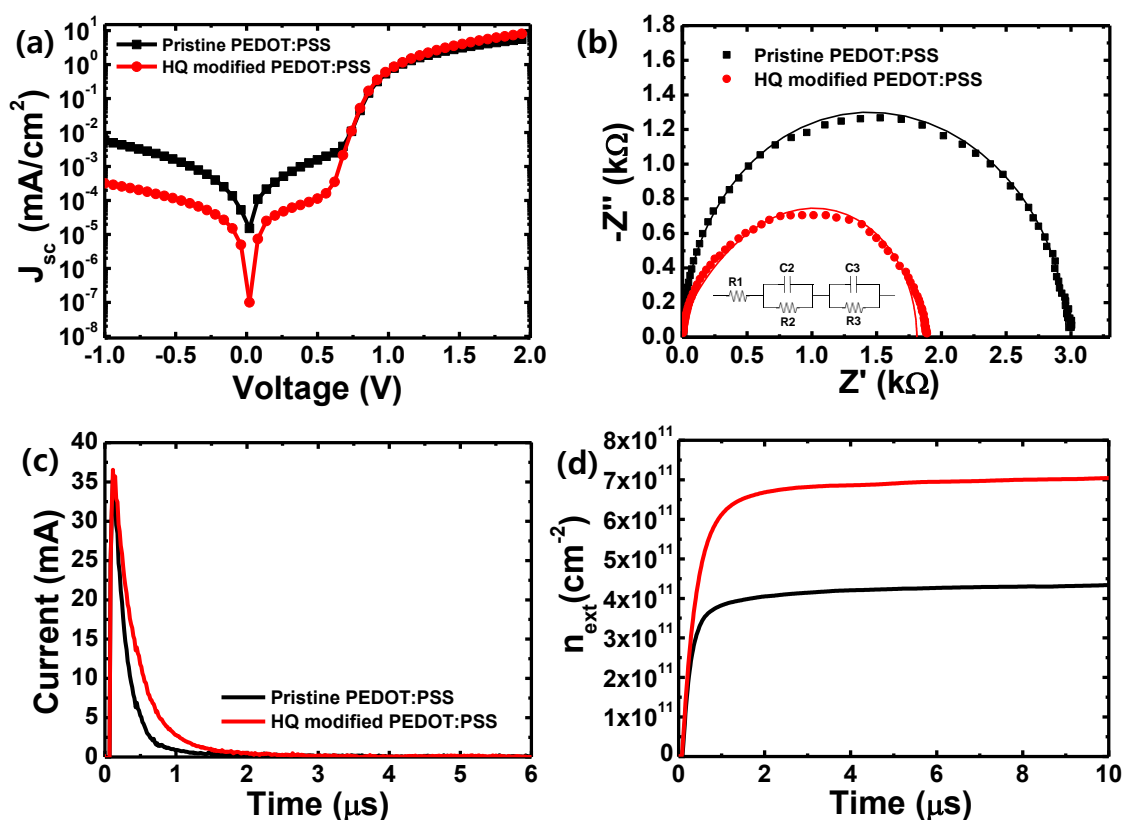
Figure 2.6. (a) Dark *J-V* characteristics of PTB7-Th:PC$_{71}$BM solar cells with pristine PEDOT:PSS and HQ-modified PEDOT:PSS. (b) Nyquist plot of impedance spectroscopy measurements at V_{oc} under light irradiation and the corresponding equivalent circuit model. (c) CE current transient under 1 sun V_{oc} conditions. (d) Calculated charge extraction density from the CE measurements.

One more thing to note in the energy diagrams obtained through UPS measurements (**Figures 2.5e** and **2.5f**) is the VL shift. When an organic layer contacts a metallic layer, the organic layer can be affected by the potential of the surface dipole. In general, VL shifts can yield the magnitude and direction of the interfacial dipole that originates from the polarization of the charge carrier density at the metallic surface. Therefore, the larger VL shift indicates that the PEDOT:PSS with HQ treatment has more free charge carriers than the pristine PEDOT:PSS, which indicates the possibility that the HQ allows secondary doping of the PEDOT:PSS surface. The conjugated PEDOT is positively doped by the sulfonate anionic groups of the PSS.[124] Because the PEDOT:PSS is not fully doped, it can be doped to a higher level by an additional protonating source. In fact, many papers have reported on secondary doping of PEDOT:PSS.[125-127] To investigate the possibility that the HQ treatment was responsible for secondary doping, we measured the conductivity sheet resistance of the PEDOT surface (**Table 2.4**).

Pristine PEDOT:PSS had a conductivity of 0.18 ($\pm 6.35 \times 10^{-3}$) Ω^{-1}cm^{-1} and sheet resistance of 1,340$\pm$9.87 kΩ/□. The PEDOT:PSS with HQ treatment, however, showed a significantly reduced sheet resistance of 59.1$\pm$0.92 kΩ/□, almost two orders of magnitude lower. Such reduction of surface resistance also can be originated by the reduction of PSS.[128] However, in our case, no PSS reduction was observed in XPS study. Furthermore, if there was a reduction of PSS by HQ treatment, there would have been a significant morphology change. However, we couldn't get any significant change of surface morphology of PEDOT:PSS by HQ treatment. Based on these facts, we concluded that additional doping by hydroxyl group of HQ would be main mechanism rather than PSS reduction.

Table 2.4. Conductivity and sheet resistance of pristine PEDOT:PSS and HQ-modified PEDOT:PSS.

	Thickness (nm)	Conductivity (Ω^{-1}cm^{-1})	Sheet Resistance (kΩ/□)
Pristine PEDOT:PSS	52.5	0.18 ($\pm 1.35 \times 10^{-3}$)	1,340 ($\pm$9.87)
HQ-modified PEDOT:PSS	51.7	3.38 ($\pm 5.17 \times 10^{-3}$)	59.1 ($\pm$0.92)
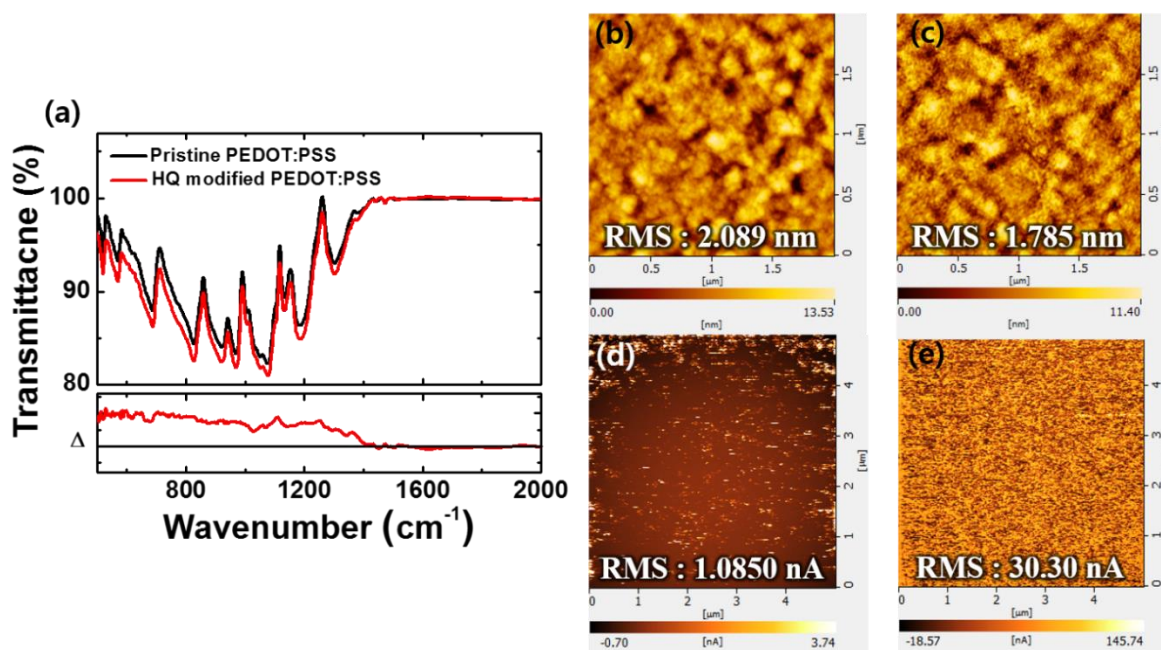
Figure 2.7. (a) FTIR absorption spectra of IRAV modes in mid-IR region in pristine PEDOT:PSS and HQ-modified PEDOT:PSS. AFM topo images of (b) pristine PEDOT:PSS and (c) HQ-modified PEDOT:PSS. C-AFM images of (d) pristine PEDOT:PSS and (e) HQ-modified PEDOT:PSS on an ITO substrate in the dark at +3V.

We also found evidence of secondary doping in our Fourier-transform infrared spectroscopy (FTIR) measurements. **Figure 2.7a** shows the mid-IR absorption spectra obtained from the pristine PEDOT:PSS and HQ-modified PEDOT:PSS. Because the PEDOT:PSS was dispersed in water, we used ZnSe as a substrate instead of KBr, which has a weak resistance in water. Direct comparison between the absorption peaks of pristine PEDOT:PSS and HQ-modified PEDOT:PSS indicates that the intensity of all the absorption peaks in the HQ-modified PEDOT:PSS increased slightly. A conducting polymer in a doped state exhibits very strong doping-induced infrared bands, so called infrared active vibration (IRAV) modes, in the mid-IR region (typically between 400 cm^{-1} and 1500 cm^{-1}, the fingerprint region). All the peaks observed between 500 cm^{-1} and 1500 cm^{-1} in both the pristine PEDOT:PSS and HQ-modified PEDOT:PSS are IRAV modes. Normally, the intensity of the IRAV modes increases slightly with the doping level.[129] Therefore, slightly increased IRAV modes in the HQ-modified PEDOT:PSS clearly indicate that the PEDOT:PSS was secondarily doped by the HQ.

Lastly, to confirm whether the improvement of solar cell performance was caused by the morphology change at the interface, we took atomic force microscopy (AFM) measurements for the PEDOT:PSS layers with and without HQ treatment. **Figure 2.7b** shows the AFM image of the pristine PEDOT:PSS, which had a root mean square (RMS) roughness value of ~2.1 nm. **Figure 2.7c** shows the AFM image of the HQ-modified PEDOT:PSS, and it had a RMS roughness value of ~1.8 nm. Although the RMS roughness of the HQ-modified PEDOT:PSS layer was slightly lower than that of the pristine PEDOT:PSS, the surface morphology did not change significantly. Therefore, we conclude that the improvement in the performance of the solar cell with the HQ-modified PEDOT:PSS was not due to a morphology change at the interface between the PEDOT:PSS and the active layer. In conducting AFM (C-AFM) measurements, which can probe local current levels, we found that the overall current level improved significantly in the HQ-modified PEDOT:PSS, as shown in **Figures 2.7d and 2.7e**. This C-AFM result is consistent with our previous results and confirms that the performance improvement in the solar cell with HQ-modified PEDOT:PSS resulted from enhancements to the charge transfer property between the PEDOT:PSS and the active layer.

2.4 Conclusion

In summary, we have enhanced the PCE of PTB7-Th:PC$_{71}$BM BHJ solar cells by modifying the PEDOT:PSS surface with HQ. Although the band bending degree of PTB7-Th on the HQ-modified PEDOT:PSS was slightly larger than on pristine PEDOT:PSS, the HQ treatment lowered the hole transport barrier at the interface between the PEDOT:PSS and the active layer. In addition, because the HQ had a secondary doping effect, the sheet resistance of the PEDOT:PSS surface decreased by almost two orders of magnitude. IS studies clearly show reduced interfacial resistance after HQ treatment of the PEDOT:PSS surface. By lowering the hole transport barrier and reducing interfacial resistance, the HQ treatment nearly doubled the hole extraction density calculated from the CE measurement. An increase in the current level of the HQ-modified PEDOT surface was also clearly seen in our C-AFM results. Thus, the device fabricated with HQ-modified PEDOT:PSS showed a 28% increase in efficiency compared to the device without HQ treatment. The best solar cell with HQ-modified PEDOT:PSS exhibited a maximum PCE of 10.18%. Modifying the PEDOT:PSS surface using an HQ solution is thus an easy way to effectively boost the performance of polymer solar cells.

Chapter 3. High-Efficiency Polymer Homo-Tandem Solar Cells with Carbon Quantum-Dot-Doped Tunnel Junction Intermediate Layer

3.1 Research Background

BHJ plastic solar cells (PSCs) based on composites of semiconducting polymers and soluble fullerene derivatives have received much attention in the field of renewable energy sources due to the advantages of light weight, low cost, flexibility, and simple fabrication process.[130-132] Over the last decade, substantial progress in the field of BHJ solar cells has increased single-cell efficiency to near 13%.[133,134] Despite this improvement, the commercialization of PSCs still lags behind due to the insufficient PCE caused by sub-bandgap transmission and narrow absorption region which leads to a low short-circuit current (J_{sc}), and weak symmetry breaking which leads to a low open circuit voltage (V_{oc}).[135,136] To overcome this PCE limitation of single-junction organic solar cells, tandem structure, which connects two single cells in series through intermediate connection layer (ICL), was introduced to improve both spectral response and V_{OC}.[137,138] There are two approaches to construct a tandem structure depending on the combination of donor materials utilized in the two sub-cells. First, in a general tandem solar cell, a tandem structure was constructed with two different donor materials with complementary absorption spectra and minimal absorption overlap to obtain wide range light absorption.[139,140] The other type tandem solar cell is the so-called homo-tandem solar cell, which is fabricated using same donor material for both front cell and back cell.[136,141-144] The main concept of homo-tandem cell is split a thick photoactive layer into two thin subunits in order to induce improvement both on light absorption by doubling light pathway and on charge extraction property by shortening the travel distance of charge carriers. In construction of tandem solar cells, ICL is the most critical component to achieve high performance. In an early study on tandem solar cells, tandem structure was investigated with thin metal ICL to make series stacking of two subcells.[146-147] Although expected sum of the V_{oc} of the two sub-cells was achieved, J_{sc} was significantly lower than that of either single cell because of weak metallic properties of thin metal film. In addition, even though thin thickness near 5 nm was utilized, thin metal ICL showed semitransparency, thereby some loss of passing lights from front cell to back cell was inevitable. In 2007, Kim et al. have demonstrated the first successfully accomplished tandem solar cells with a PCE over 6% using p-n junction ICL layer consisting of a poly(3,4-ethylenedioxythiophene)-poly(styrenesulfonate) (PEDOT:PSS) hole transporting layer (HTL) and a TiO_x electron transporting

layer (ETL).[139] The p-n junction layer inserted between two sub-cells functions as the charge recombination layer, and it simultaneously induces the shift of vacuum levels driven by the alignment of Fermi levels of the HTL and ETL. Recently, new conceptual intermediate ICL layer has demonstrated by Zhou et al.[148] Their new ICL, named tunnel junction ICL, consisted of PEDOT:PSS HTL and a polyethyleneimine (PEI) interfacial polyelectrolyte. The PEI is ionically self-assembled on PEDOT:PSS surface and then induce favorable interfacial dipoles on the PEDOT:PSS surfaces by forming a strong electrostatic force. As a result, the ultrathin PEI layer reduces the surface work-function (WF) up to 3.9 eV, thereby facilitates electron extraction.[143,148-151] However, based on the mechanisms known so far, such dipole-mediated WF modification is thought to occur only near interface.[143,152,153] Furthermore, since the intrinsic feature of PEI is nonconducting insulator. Even if a little thicker PEI layer is introduced, the series connection of the tandem cell will be cut off. Thus, only ultrathin PEI layer less than 2 nm can work properly as an ideal ICL component.[143,148-151] However, fabrication of uniform ultrathin PEI layer by spin coating is not that easy, thereby reducing reproducibility of tandem devices. To overcome this problem, in this work, we have introduced a doped PEI layer as a component of tunnel junction ICL. As a dopant, a few nanometer-sized zwitterionic carbon quantum dots (CQDs) were incorporated in PEI intermediate layer. There were a few reports that carbon-dot itself has been utilized as an electronic transporting layer or electron donor in organic photovoltaics.[154-157] Although CQDs showed promising potential as an electron transporting material, the use of CQDs alone has not yet been shown sufficient performance required in BHJ solar cells. However, the inclusion of CQDs as a dopant in PEI layer led to improved electron extraction property in single-junction solar cells and better series connection in tandem solar cells. The highest performing tandem solar cell fabricated with CQD-doped PEI layer in ICL yields a PCE of 12.13%; this value represents an ~15% increase in the efficiency compared with tandem solar cells with pristine PEI layer.

3.2 Experimental

Preparation of CQD: CQDs were synthesized by a commercial microwave (700 W). First, 1.0 g (5.2 mmol) of citric acid (Sigma Aldrich) was diluted with 10 mL of distilled water and mixed with different amount (2.6, 5.2, 10.4, 15.6, and 20.8 mmol) of β-Ala (Sigma Aldrich). Then, the transparent solution was placed into a microwave oven and heated for 3 min to proceed carbonization and surface passivation. After cooling down to room temperature, the obtained yellowish-brown solid was dissolved into distilled water and filtered with a syringe filter (0.45 μm) to remove salt and unreacted residues.

Finally, the solution was filtered against distilled water through a polyacrylamide desalting columns (MWCO: 1800 Da) (Thermo Fisher Scientific, Inc., PA, USA), collecting the same volume of solution that emerged from the column. To observe the quantum yield (QY, %) according to the ratio between citric acid and β-Ala, quinine sulfate in 0.1 N sulfuric acid solution was used as a reference at excitation wavelength of 360 nm.

TEM of CQD: HRTEM (JEM-2100F, JEOL) analysis was performed to investigate the size and morphology of the CQDs. The accelerating electron voltage was 200 kV.

Cross-Sectional TEM of Tandem Solar Cell: The cross-sectional TEM samples were prepared through a conventional mechanical polishing process including cutting, grinding, polishing, and a final ion-milling thinning step by means of focused ion beam (AURIGA dual-beam FIB, Carl Zeiss) milling. Ion beam (Ga ion) acceleration voltage was 5 kV. The cross-sectional structure of tandem solar cells was investigated by TEM (JEM-ARM200F, JEOL) operated at 200 keV with scanning transmission electron microscopy (STEM) mode. The thickness of each layer was measured using scale bar in TEM.

Single-Junction Device: The ITO substrates were cleaned with detergent, ultrasonicated in acetone and isopropyl alcohol (IPA) for 15 min each. The PEI was dissolved in distilled water (0.1 mg mL^{-1}) with various doping amounts of CQD solution. The weight ratios of CQD and PEI were 0, 0.1, 0.3, 0.5, 0.7, and 1 wt%. The blended PEI solutions were ultrasonicated for 30 min. Prepared blended PEI solutions were spin-coated at 5000 rpm for 30 s on top of the ITO in air after oxygen plasma treatment, and annealed at 100 °C for 10 min. The PEI-coated ITO substrates were then transferred into a N_2-filled glove box. The PTB7-Th:$PC_{71}BM$ solution was made by 1:1.5 weight ratios in chlorobenzene with 3 vol% of 1,8-diiodooctane (DIO) at room temperature and spin coated at 1000 rpm for 60 s on top of the PEI layer and dried for 1 h. Finally, a 5 nm MoO_3 layer and 100 nm Ag layer were deposited by thermal evaporation method as top electrode at the vacuum condition of 2×10^{-6} torr. The device area was 0.13 cm^2.

Tandem Device Fabrication: The ITO substrates were cleaned with detergent, ultrasonicated in acetone and isopropyl alcohol for 15 min each. The CQD 0.5 wt% of PEI solution was spin coated at 5000 rpm for 30 s on top of the ITO in air after oxygen plasma treatment and annealed at 100 °C for 10 min. The substrates were then transferred into an N_2-filled glove box. The bottom layer of PTB7-Th:$PC_{71}BM$ (1:1.5 weight ratios in chlorobenzene with 3 vol% of DIO) was prepared by spin coating at 1300 rpm for 45 s and annealed at 80 °C for 10 min. Then the intermediate layers m-PEDOT:PSS and PEI were coated. The m-PEDOT:PSS with Triton X-100 (0.1 wt%) was coated on top of the PTB7-Th:$PC_{71}BM$ active layer at 2000 rpm for 60 s and dried for 1 h. Then a thin layer of PEI film was spin-coated at 5000 rpm for 30 s, followed by thermal annealing at 80 °C for 10 min. The top active layer of

PTB7-Th:PC$_{71}$BM (1:1.5 weight ratios in chlorobenzene with 3 vol% of DIO) was prepared by spin coating at 1000 rpm for 45 s and annealed at 80 °C for 10 min. Finally, a 5 nm MoO$_3$ layer and 100 nm Ag layer were deposited by thermal evaporation method as top electrode at the vacuum condition of 2 × 10^{-6} torr. The device area was 0.13 cm^2.

Device Characterizations: The *J-V* curves of the solar cell devices were obtained using a Keithley 2401 source measurement unit under AM1.5G simulated illumination (100 mW cm^{-2}). All measurements were performed inside glove box filled with N$_2$. The intensity of the simulated sunlight was measured using a standard Si-photodiode detector with a KG-3 filter (Newport Co., Oriel). An aperture mask was used while measuring the devices. EQE and IQE spectra of each solar cell device were obtained using a solar cell spectral response/QE/IPCE measurement system (Newport Co., Oriel IQE-200B). The light intensity at each wavelength was calibrated using a standard single crystal Si photovoltaic cell. The absorption spectra were measured by a UV-vis spectrometer (Varian, Cary5000).

AFM Measurements: The surface morphologies of the pristine PEI and CQD-doped PEI films were characterized by AFM. The AFM images (scan area: 5.0 μm × 5.0 μm and 1.0 μm × 1.0 μm) were obtained using a Seiko E-Sweep atomic force microscope in tapping mode.

IS Measurements: Nonmodulated impedance spectroscopy and IMVS were performed using an impedance analyzer function of organic semiconductor parameter test system (McScience T4000) at various forward biases. A 30 mV voltage perturbation was applied over a constant forward applied bias between 0 and 1.55 V in the frequency range between 0.1 Hz and 1.0 MHz with a red light emitting diode (LED) light source. The LED (λ = 635 nm) provided both the DC and AC components of the illumination, where the modulation depth of the AC component superimposed on the DC light was 10%. The light intensity was 0.85 mW cm^{-2}, which was measured silicon photodiode. In order to maintain pseudolinearity, only small intensity amplitudes were applied. In addition, the cell was illuminated prior to each experiment and its open-circuit potential was measured until it was constant.

UPS Measurements: Photoelectron spectroscopies were carried out with an ESCALAB 250-XI surface analysis system equipped with a He-discharge lamp providing He-I photons of 21.22 eV for UPS analysis; and a monochromatic Al-Kα X-ray gun with photons energies of 1486.6 eV for X-ray photoelectron spectroscopy (XPS) investigation. The base vacuum pressure of the analysis system was ~10^{-7} torr. The Fermi edge was calibrated using a clean ITO film, and all spectra presented were plotted with respect to the determined Fermi level. All XPS measurements were calibrated with reference to the In 3d$_{5/2}$ core level (443.9 eV) of a freshly ITO film.

3.3 Results and Discussion

Figure 3.1a shows the schematic illustration of the synthesis procedure of CQDs used in this study. The CQDs were prepared according to a well-established one-pot microwave pyrolysis reported in previous literatures using citric acid (CA) as a carbon source and amino acid derivative (β-alanine) as a zwitterionic passivation agent.[158,159] Details regarding the fabrication of CQDs are described in the Experimental Section. A high-resolution transmission electron microscopy (HRTEM) image of the C-dots is presented in **Figure 3.1b-d**. The TEM image clearly shows their monodispersity and narrow size variation. The typical mean size of the CQDs was 3.1 ± 0.5 nm. In addition, a crystalline hexagonal unit structure with an interlayer spacing of 0.24 nm, which corresponds to (111) lattice spacing of the graphite hexagons,[160,161] was clearly observed by aberration-corrected HRTEM (**Figure 3.1d**). Note that only one size CQD was utilized in current study. The size of CQD may not the optimal size. There might be a possibility to show better performance when using different sized CQDs. First, the effects of CQD doping on PEI layer were investigated with single-junction solar cells.
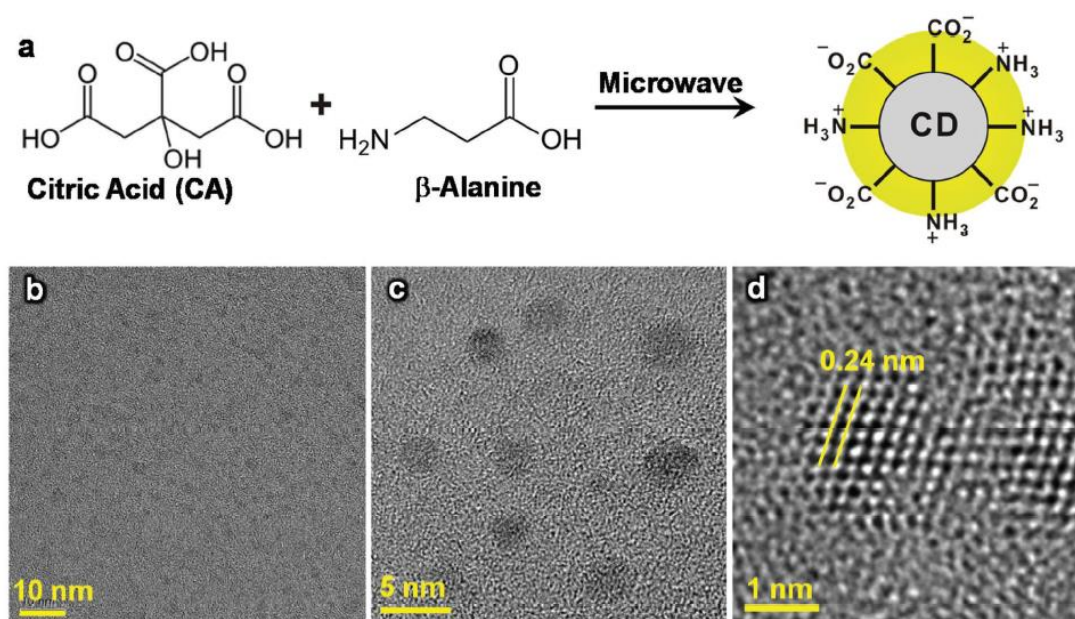
Figure 3.1. (a) Schematic scheme of CQD synthesis. (b, c) TEM images of CQDs. The typical mean size of the CQDs was 3.1 ± 0.5 nm. (d) HRTEM image showed the arrangement of carbon atoms in CQDs with a lattice spacing of 0.24 nm.

Figure 3.2a shows schematic illustration of single-junction solar cell structure. Instead of general ETL based on metal oxide such as ZnO and TiO_2,[131,132,164] PEI WF modify layer was introduced in between photoactive layer and indium tin oxide (ITO) electrode.[83,161] **Figure 3.2b** shows the current density (J)-voltage (V) characteristics of inverted BHJ solar cells based on poly[4,8-bis(5-(2-ethylhexyl)thiophen-2-yl)benzo[1,2-b:4,5-b′]dithiophene-alt-3-fluoro-thieno[3,4-b]-thiophene-2-carboxylate] (PTB7-Th, also called PCE-10) and [6,6]-phenyl-C71-butyric acid methyl ester ($PC_{71}BM$). Details related to the performance of these solar cells are listed in Table 3.1. The single-junction solar cell with pristine PEI layer yielded a PCE of 8.56% with a J_{sc} of 16.430 mA cm^{-2}, a V_{oc} of 0.774 V, and a fill factor (FF) of 0.673. The performance of solar cells with CQD-doped PEI layer gradually enhanced with increasing the doping ratio up to 0.5%. The best efficiency solar cell showed the PCE of 9.49% with a J_{sc} of 17.242 mA cm^{-2}, a V_{oc} of 0.772 V, and an FF of 0.713. However, when the doping ratio was exceeded over 5%, rather the cell efficiency was reduced. These performance enhancements by introducing CQD-doped PEI layer were universal. It was clearly observed from other polymer BHJ systems.
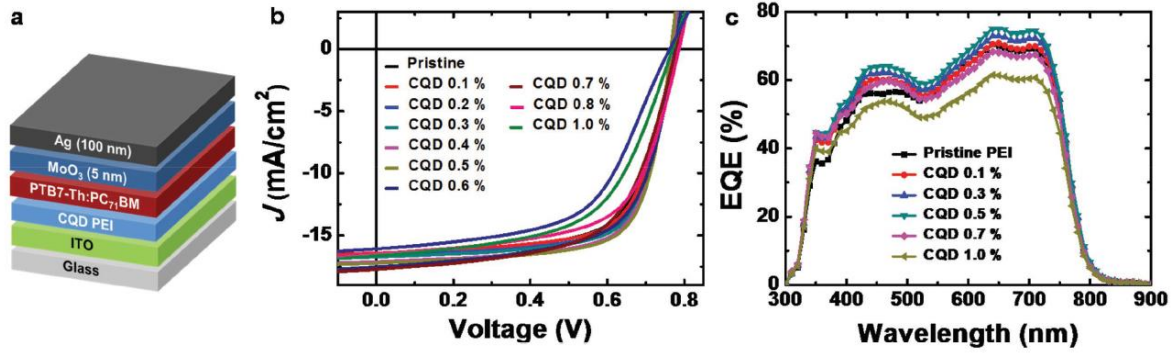
Figure 3.2. (a) Schematic illustration of the single-junction solar cell structure. (b) *J-V* characteristics of PTB7-Th:PC$_{71}$BM single-junction solar cells with pristine PEI and CQD-doped PEI with various doping ratio. Note that the PEI layer in single-junction solar cells was acted as a WF modify layer. (c) EQE spectra of PTB7-Th:PC$_{71}$BM single-junction solar cells with pristine PEI and CQD-doped PEI with various doping ratio.

Table 3.1. Summarized photovoltaic performance characteristics of single-junction solar cells with pristine PEI layer and CQD-doped PEI layer with various doping ratios.

	V_{OC} (V)	J_{SC} (mA/cm^2)	*FF*	η (%)	η_{avg} (%)
Pristine PEI	0.774	16.430	0.673	8.56	8.40
CQD 0.1%	0.774	16.422	0.679	8.63	8.46
CQD 0.2%	0.771	16.598	0.692	8.87	8.64
CQD 0.3%	0.770	16.737	0.703	9.06	8.86
CQD 0.4%	0.769	17.131	0.705	9.29	9.01
CQD 0.5%	0.772	17.242	0.713	9.49	9.30
CQD 0.6%	0.777	17.551	0.654	8.92	8.89
CQD 0.7%	0.779	17.740	0.619	8.55	8.39
CQD 0.8%	0.785	16.285	0.629	8.04	7.80
CQD 0.9%	0.770	16.621	0.579	7.41	7.31
CQD 1.0%	0.761	16.081	0.574	7.03	6.89

Figure 3.3a and 3.3b showed the *J-V* characteristic results obtained from poly(3-hexylthiophene) (P3HT) and [6,6]-phenyl-C61-butyric acid methyl ester ($PC_{61}BM$), poly[[4,8-bis[(2-ethylhexyl)oxy]benzo[1,2-b:4,5-b′]dithiophene-2,6-diyl][3-fluoro-2-[(2-ethylhexyl)-carbonyl]-thieno-[3,4-b]thiophenediyl]] (PTB7), and $PC_{71}BM$, respectively. Details of the performance of these solar cells are listed in Table 3.2 and 3.3. In all cases, the optimal CQD doping ratio was found to be 0.5%. Using the optimized CQD doping condition obtained from single-junction solar cells, a tunnel junction ICL layer was constructed for homo-tandem solar cells. The tunnel junction ICL layer consisted of m-PEDOT:PSS and CQD-doped PEI layer as shown in **Figure 3.4a**. The m-PEDOT:PSS was prepared by mixing of 100 ml PEDOT:PSS (AI4083) and 100 μL 4-(1,1,3,3-Tetramethylbutyl)phenyl-polyethylene glycol solution (Triton X-100) based on the information in the literatures.[140,163,164] As in the case of the single cell, the photoactive materials of both front cell and back cell was composed of PTB7-Th and $PC_{71}BM$. The cross-sectional TEM image in **Figure 3.4b** showed physically well-constructed tandem structure. Although it is a bit difficult to distinguish the CQD-doped PEI layer as a finite distinct layer because of relatively thin thickness, the CQD doped PEI layer can be confirmed by the difference in contrast due to higher electron density compared with m-PEDOT:PSS. The thickness of the front cell was 75 nm and the thickness of the back cell was 96 nm. In addition, average thickness of our PEI layers was definitely thicker than the thickness proposed by previous study.[143,148,149]

Figure 3.4c shows *J-V* characteristics of tandem solar cells with CQD-doped PEI ICL and pristine PEI ICL. The results obtained from single-junction solar cells were presented together for comparison. Overall feature of *J-V* characteristics was a typical photovoltaic response of tandem solar cells; reduced J_{sc} compared with that of single solar cells and doubling on V_{oc}. The tandem solar cell with pristine PEI yielded a PCE of 10.54% with a J_{sc} of 10.67 mA cm^{-2}, a V_{oc} of 1.581 V, and an FF of 0.625. The tandem solar cells with CQD-doped PEI ICL exhibited significantly enhanced performance. The PCE of the best performing tandem solar cell reached 12.13% with simultaneous enhancements in a J_{sc} of 11.485 mA cm^{-2}, a V_{oc} of 1.581 V, and an FF of 0.668. Performance parameters of tandem solar cells are summarized in Table 3.4 together with the results obtained from the best-performing single-junction solar cells.
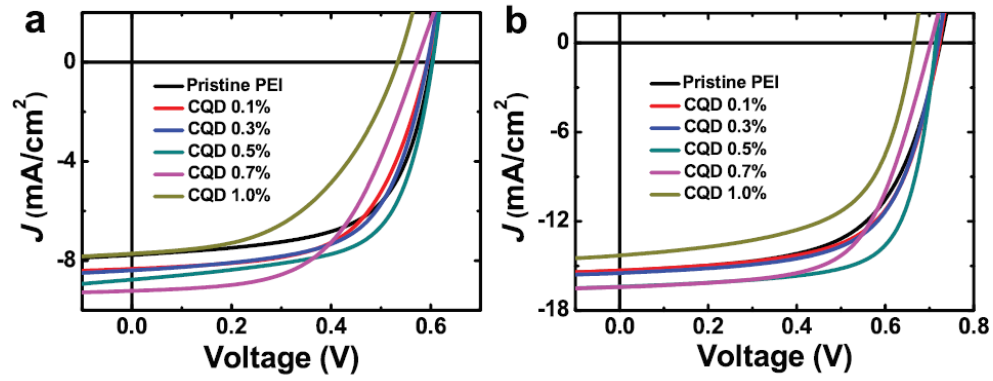
Figure 3.3. (a) *J-V* characteristics of P3HT:PCBM single-junction solar cells with pristine PEI and CQD-doped PEI with various doping ratio. (b) *J-V* characteristics of PTB7:$PC_{71}BM$ single-junction solar cells with pristine PEI and CQD-doped PEI with various doping ratio. In both cases, the optimized CQD doping concentration was 0.5%.

Table 3.2. Summarized photovoltaic performance characteristics of single junction solar cells fabricated with P3HT and $PC_{61}BM$ as a photoactive layer.

	V_{OC} (V)	J_{SC} (mA/cm^2)	*FF*	η (%)
Pristine PEI	0.603	7.800	0.618	2.904
CQD 0.1%	0.594	8.279	0.604	2.970
CQD 0.3%	0.593	8.404	0.620	3.090
CQD 0.5%	0.604	8.760	0.624	3.297
CQD 0.7%	0.576	9.247	0.547	2.917
CQD 1.0%	0.533	7.651	0.501	2.043

Table 3.3 Summarized photovoltaic performance characteristics of single junction solar cells fabricated with PTB7 and $PC_{71}BM$ as a photoactive layer.

	V_{OC} (V)	J_{SC} (mA/cm^2)	*FF*	η (%)
Pristine PEI	0.723	15.297	0.619	6.845
CQD 0.1%	0.724	15.291	0.633	7.011
CQD 0.3%	0.723	15.469	0.636	7.122
CQD 0.5%	0.715	16.395	0.706	8.271
CQD 0.7%	0.703	16.425	0.623	7.192
CQD 1.0%	0.667	14.378	0.601	5.762

Figure 3.4d shows the EQE spectra of tandem solar cells with and without CQD doping on PEI layer. In comparison, EQE spectra obtained single-junction solar cells were presented together. These presented total EQE spectra were estimated value deduced from total absorption of device and internal quantum efficiency (IQE) of sub-cells.[135,165,166] The estimate IQE of tandem solar cells calculated by dividing the two times of the measured tandem EQE by the total absorption of tandem cells was similar with IQE of single cells. From **Figure 3.4d**, the calculated total EQE of tandem solar cell with CQD-doped PEI ICL exhibits a slightly increase, on average by 20%, compared to that of tandem solar cell with pristine PEI ICL. This result indicates that m-PEDOT:PSS and CQD-doped PEI were better functioning as an interconnection layer, result in well matching of photocurrents between the two identical sub-cells.
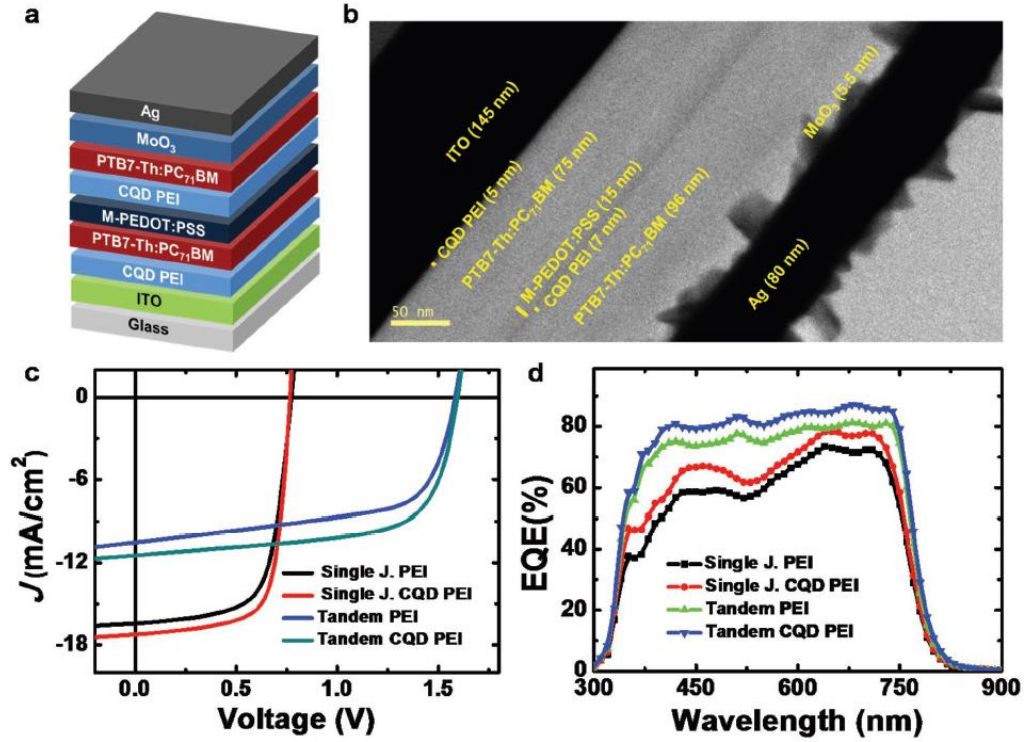
Figure 3.4. (a) Schematic illustration of the homo-tandem solar cell structure. (b) Cross-sectional TEM images of tandem solar cell with CQD-doped PEI. (c) *J-V* characteristics of tunnel junction tandem solar cell with and without CQD doping on PEI. *J-V* characteristics of single-junction solar cells were presented together for comparison. (d) Estimated EQE spectra deduced from total absorption of device and IQE of sub-cells. EQE spectra of single-junction solar cells were presented together for comparison.

Table 3.4. Summarized photovoltaic performance characteristics of single-junction solar cells and tandem solar cells with pristine PEI layer and CQD-doped PEI layer.

	V_{OC} (V)	J_{SC} (mA/cm^2)	*FF*	η (%)	η_{avg} (%)
Single J/Prisine PEI	0.774	16.430	0.673	8.56	7.78
Single J/CQD-doped PEI	0.772	17.242	0.713	9.49	8.66
Tandem/Prisine PEI	1.581	10.669	0.625	10.54	9.79
Tandem/CQD-doped PEI	1.581	11.485	0.668	12.13	11.57

Figure 3.5 shows the statistical distribution of the efficiency of single-junction cells and tandem solar cells efficiency. The results of 50 devices were used for each condition. In both single-junction cell and tandem cell, a clear increase tendency was observed by CQD doping on PEI layer. Interestingly, the distribution range of tandem solar cell was definitely narrow compared with single-junction solar cells, which means reproducibility of our tandem solar cell was also fairly good. In order to investigate the morphology changes in the PEI layer by adding the CQD, atomic force microscopy (AFM) measurements were performed.
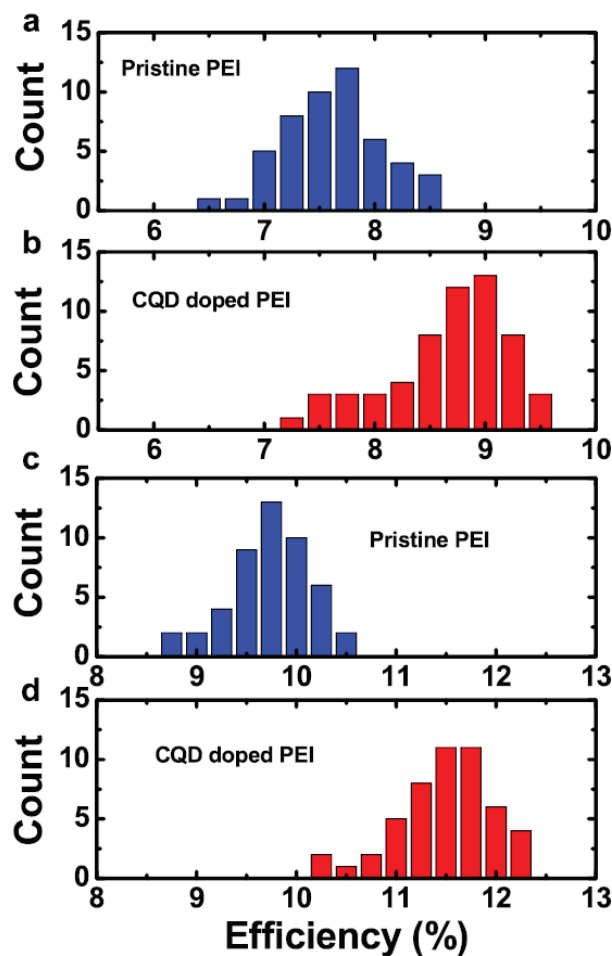
Figure 3.5. (a) Statistical distribution of the efficiency of single-junction cells with pristine PEI layer. (b) Statistical distribution of the efficiency of single junction cells with CQD-doped PEI layer. (c) Statistical distribution of the efficiency of tunnel junction tandem solar cells with pristine PEI layer. (d) Statistical distribution of the efficiency of tunnel junction tandem solar cells with CQD-doped PEI layer.

Figure 3.6 shows AFM images of PEI layers with various concentration of CQD dopant. From these AFM topography images, no distinct morphological changes were observed. Even in enlarged scale AFM images, no meaningful morphological changes were observed. Therefore, we can exclude the possibility of increasing performance due to morphology change. The enhancement on performance of both single-junction cells and tunnel junction tandem cells with CQD doping was attributed to improvement on overall impedance (resistance) of device.
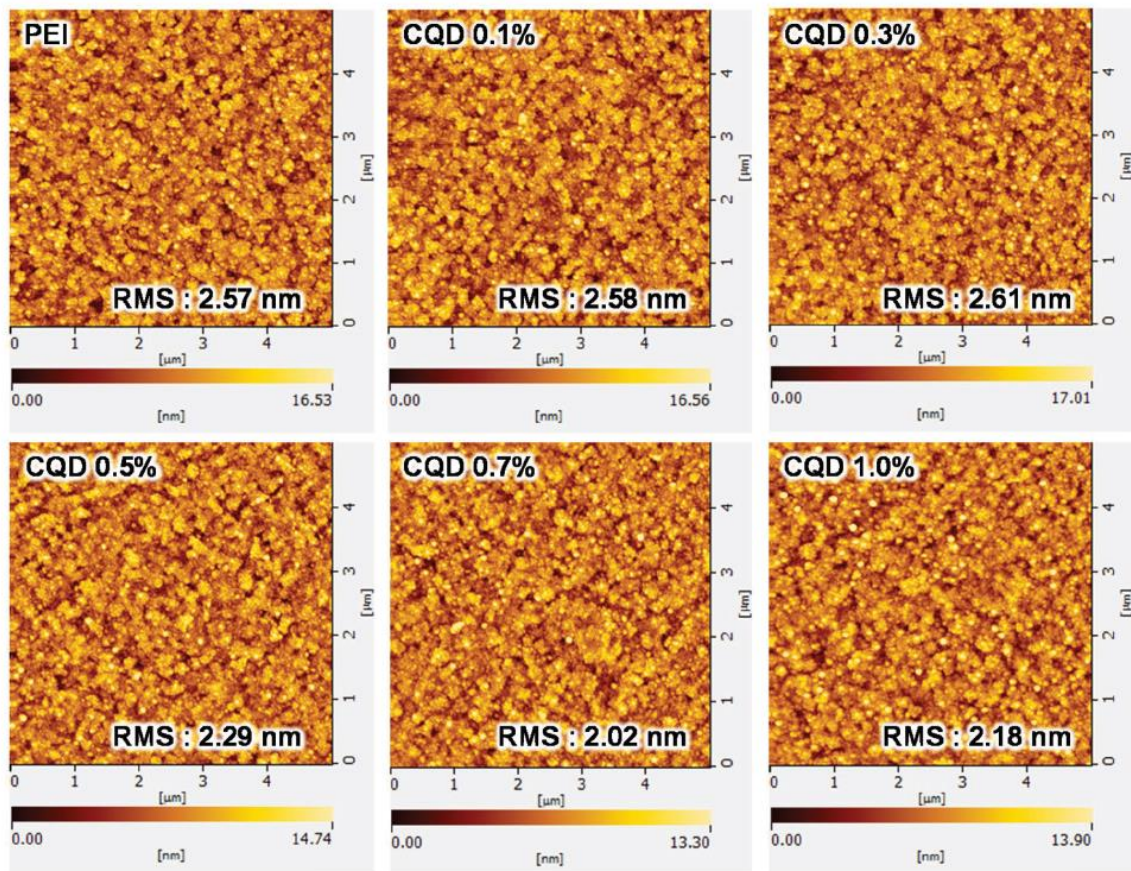
Figure 3.6. AFM height image (5.0 μm × 5.0 μm) of pristine PEI layer and CQD-doped PEI layer with various doping ratio.

Figure 3.7a shows the Nyquist plots of impedance spectra for single-junction solar cells with various CQD doping ratio. Note that overall features of impedance spectroscopy (IS) spectra of both single-junction solar cells and tandem solar cells are typical of Gericher impedance. In which case, transport resistance and recombination resistance cannot be unambiguously determined.[167,168] Thus, only relative comparison is possible with combined effective resistance named Gericher resistance. The real part of impedance was gradually decreased with increasing the doping ratio up to 0.5%. However, with over 0.5% CQD doping, the real part impedance value was larger than the value of solar cell with pristine PEI. These results are in good agreement with *J-V* characteristics, which indicate that better diode characteristics were formed with small amount CQD incorporation at PEI WF modify layer.[122,168]

    Figure 3.7b shows the results of IS for tandem solar cells with and without CQD doping on PEI. In tandem solar cells for IS measurements, WF modification of ITO was performed with pristine PEI to extract the effect of PEI doing on ICL only. As similar to the single-junction cells, the real part of impedance was significantly decreased with CQD doping, which indicates that better series connection with reduced series resistance was built up at ICL by incorporation of CQD-doped PEI. It is worthy to note that these decreases in impedance did not seem to be due to energy level changes by CQD doping because no WF changes were detected in ultraviolet photoelectron spectroscopy (UPS) measurements as shown in **Figure 3.8**. For further analysis, intensity modulated photovoltage spectroscopy (IMVS) was carried out successively as shown in **Figure 3.7c**. IMVS measures the photovoltage response, which is periodically modulated by the difference in the Fermi level in the dark and the quasi Fermi level under illumination, of the cell to a small sinusoidal perturbation of light intensity superimposed on a largely steady background level. IMVS is performed under open-circuit conditions. In open-circuit condition, the solar cell reaches steady-state at the open-circuit potential, which means the rate of charge injection is equal to the charge recombination rate. Thus, IMVS provides information about the carrier lifetime and electron–hole recombination dynamics under open-circuit conditions.[122,168-170] The semicircle radius of IMVS spectrum was significantly decreased in tandem solar cell with CQD-doped PEI layer. Thus, the frequency corresponding to the minimum in the complex plane was increased, which indicated that the carrier lifetime was decreased. Therefore, it means that the carrier recombination was more pronounced at tandem solar cell with CQD-doped PEI layer. Since we used same configuration for both devices expect CQD doping, this difference was likely to be induced by CQD doping at PEI ICL. Thus, we attributed the enhancement of performance of tandem solar cell with CQD doped PEI to more effective recombination of electrons produced in back cell and holes produced in front cell in the ICL.
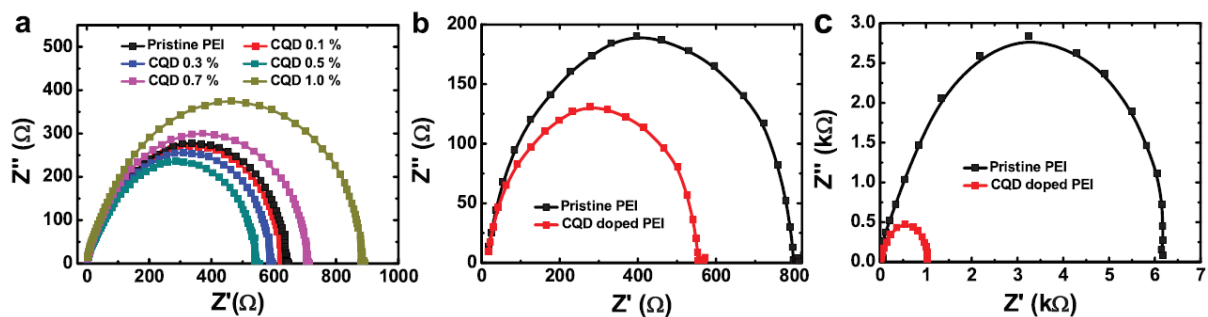
Figure 3.7. (a) Nyquist plots of impedance spectra for single-junction solar cells with various CQD doping ratio. (b) Nyquist plots of impedance spectra for tandem solar cells with and without CQD doping on PEI. (c) Intensity modulated photovoltage spectroscopy (IMVS) of tandem solar cells with and without CQD doping on PEI.
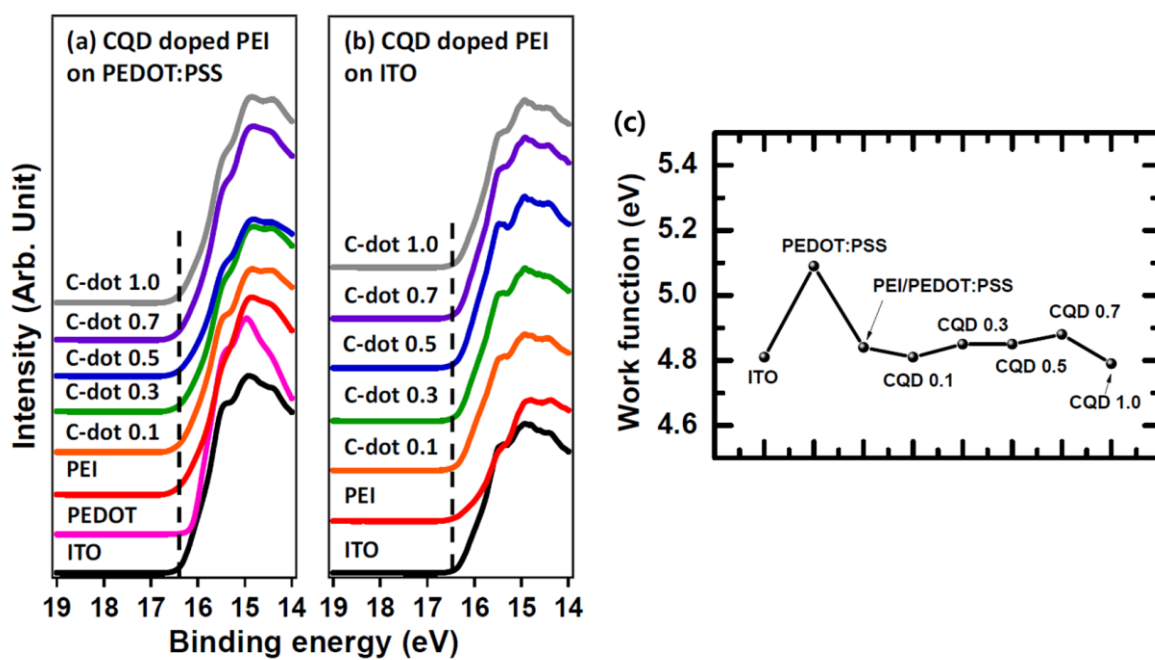
Figure 3.8. UPS spectra of (a) CQD doped PEI on PEDOT:PSS, (b) CQD doped PEI on ITO. (c) Work-function values deduced from UPS spectra. The work-function of PEODT:PSS was significantly reduced with PEI covering. However, CQD doping did not change the modified work-function of PEDOT:PSS.

3.4 Conclusion

In conclusion, we have demonstrated high-efficiency homo-tandem solar cells with enhanced PCE by introducing a CQD-doped PEI on a tunnel junction ICL. The CQD-doped PEI layer provided substantial dynamic advantages in the operation of both single-junction solar cells using the PEI as an ITO WF modifying layer and homo-tandem solar cells based on the tunnel junction ICL. The inclusion of CQDs in PEI layers leads to improved electron extraction property in single-junction solar cells and better series connection in tandem solar cells. The highest efficient solar cell with CQD-doped PEI layer in between ITO and photoactive layer exhibited a maximum PCE of 9.49%, which represents a value nearly 10% higher than those of solar cells with pristine PEI layer. In case of tandem solar cells, the highest performing tandem solar cell fabricated with CQD-doped PEI layer in ICL yields a PCE of 12.13%; this value represents an ≈15% increase in the efficiency compared with tandem solar cells with pristine PEI layer. IS studies clearly showed enhanced recombination process in ICL layer with CQD-doped PEI layer. Therefore, we concluded that the enhanced PCE in the tandem solar cells with a CQD-doped PEI layer was attributable to effective recombination of electrons produced in back cell and holes produced in front cell in the ICL together with better series connection by reducing series resistance.

Chapter 4. Improved exciton dissociation efficiency by a carbon-quantum-dot doped workfunction modifying layer in polymer solar cells

4.1 Research Background

Polymer solar cells (PSCs) based on bulk-heterojunction (BHJ) blends of semiconducting polymers and soluble fullerene derivatives have received much attention due to their potential in the production of cost-effective renewable energy sources for portable electronic devices and building integrated photovoltaics.[171-174] The low-cost simple fabrication based on a solution process is one of the greatest advantages of BHJ PSCs.[175-177] In order to maximize this advantage, there are a number of ongoing studies aimed at simplifying the process. The easiest approach for simplification of the fabrication process is omitting the functional layers that are considered to be necessary. Since the photoactive layer is not able to be removed, the charge transport layers often became the target of removal.

In inverted solar cells, the electron transport layer connecting the indium tin oxide (ITO) electrode and the photoactive layer has two functions. One is to transfer electrons from the photoactive layer to the ITO electrode. The other is the role of symmetry breaking.[136,178] Since the organic BHJ system has no prior symmetry breaking to induce an electromotive force for photocurrents, a symmetry breaking condition must be formed artificially to achieve an efficient drift of photo carriers. In conventional structure solar cells using ITO (work-function (WF) 4.7 eV) as the anode electrode and Al (WF 4.0-4.3 eV) as the cathode electrode, symmetry breaking is simply created by the WF difference between these two electrodes.[179-183] However, in inverted solar cells using ITO as the cathode and Ag as the anode, symmetry breaking is not spontaneously formed because evaporated Ag has a similar WF as ITO (WF 4.6-4.7 eV).[136,178,184-186] Of course, by combining ITO and a high WF Au electrode, symmetry breaking can be formed spontaneously. However, Au is quite expensive metal, which detracts from the great advantage of PSCs as a cost-effective energy source. Thus, generally in the case of inverted solar cells using ITO and Ag electrodes, the electron transport layer and the hole transport layer are actually in charge of generating the internal potential.

In 2012, Y. Zhou and coworkers reported an interesting method to develop better symmetry breaking, even without the electron transport layer.[83] They substantially reduced the WF of ITO and PEDOT:PSS by modifying the surface using polymers containing simple aliphatic amine groups such as

polyethyleneimine ethoxylated (PEIE) or polyethyleneimine (PEI). Their WF modification using PEI or PEIE was a universal method that was able to allow the fabrication at very low cost and from environmentally friendly solvents. However, many solar cell studies have not yet abandoned the use of electron transport layers. Thus, currently, the PEI method has been mainly used as a technique to create a tunnel-junction intermediate connection layer by modulating the work function of PEDOT:PSS in a tandem cell.[149,187,188] In single-junction PSCs, PEI was generally used as the modifier for the surface of the ZnO electron transport layer to improve the energy level alignment.[43,189] Studies using ITO electrodes directly without an electron transport layer were rare.

It is presumed that the reluctance to use PEI alone without an electron transport layer was because of the non-conducting property of the PEI modifier. Since the WF modifying effect of PEI only occurred near the interface, there was a possibility of impairing the electron transport property when a thick PEI layer was applied. In order to maintain the electron transport property of the PEI layer as much as possible, an ultrathin PEI layer (approximately 2-3 nm) should be used. However, considering that the roughness of common commercial ITO was around 2 nm, it was not easy to make a uniform 2-3 nm thin film by spin coating on the ITO surface. To overcome such problems in our previous study, we incorporated several-nm-sized zwitterionic carbon quantum dots (CQDs) into the PEI layer.[186] The incorporation of CQDs in the PEI layer led to improved electron extraction properties in single-junction solar cells even with a somewhat-thick PEI layer (approximately 7-15 nm). However, because of limited functionality of the CQD ligands focused on solubility, only improvements in charge transport properties were obtained.

In this work, we have incorporated novel CQD having NH_2 ligands into the PEI layer to improve the work-function modification effect as well as charge transport property. The CQD-doped PEI layer reduced the charge recombination and the series resistance at the interface between the active layer and PEI layer. Because of these enhanced electron transport properties of CQD-doped PEI layer, the overall photovoltaic performance of solar cells with a CQD-doped PEI layer improved significantly. In addition, a study of net photocurrent density as a function of effective voltage showed that devices with a CQD-doped PEI layer had a much higher charge separation probability compared to a device with a pristine PEI layer. This dramatic improvement in charge separation probability was attributed to enhanced exciton dissociation probability due to NH_2 ligands of CQD dopants. Kelvin-probe force microscopy study demonstrated that the CQD-doped PEI layer induced a lower work-function of ITO than that of ITO with a pristine PEI. As a result, the solar cell with CQD-doped PEI layer had a stronger internal field, and this strengthened internal field induced better exciton dissociation efficiency, thereby improving solar cell performance.

4.2 Experimental

Synthesis of NR-CQDs: CQDs were synthesized by following the microwave-assisted hydrothermal method. In a typical experiment, 0.005 g neutral red powder was dissolved in 40 mL of ethyl alcohol and 114 μL of ethylenediamine. The solution was heated in a microwave oven (700W) for 2 min. During this time, the pale orange solution changed to dark-orange by carbonization. After cooling to room temperature naturally, the solution was purified by column chromatography using silica gel (70-230 mesh). These purified carbon quantum dots were used for the experiment.

Active materials: Poly[4,8-bis(5-(2-ethylhexyl)thiophen-2-yl)benzo[1,2-b;4,5-b']dithiophene-2,6-diyl-alt-(4-(2-ethylhexyl)-3-fluorothieno[3,4-b]thiophene-)-2-carboxylate-2-6-diyl)] (PTB7-Th, also called as PCE10) was purchased from 1-material, [6,6]-phenyl C71-butyric acid methyl ester ($PC_{71}BM$) was purchased from 1-material. PEDOT:PSS (AI4083) was purchased from Heraeus Clevios. Polyethylenimine (PEI) and all solvents used in device fabrication process were purchased from Sigma Aldrich.

Solar cell fabrication: The ITO substrates were cleaned with detergent and ultra-sonicated in acetone and IPA for 15 min each. The PEI was dissolved in 2-methoxyethannol with weight concentration of 0.1wt%. CQD was added to PEI solutions to make blended PEI solutions with 0, 1%, 2%, 5% and 10% CQD. The blended PEI solutions were ultra-sonicated for 30 min. Prepared blended PEI solutions were spin-coated at 5,000 rpm for 30 s on top of the ITO in air after UV-Ozone treatment, and then annealed at 100° C for 10 min. The PTB7-Th:$PC_{71}BM$ solution was made by 1:1.5 weight ratios in chlorobenzene with 3 vol% of DIO at RT and spin-coated at 1,000 rpm for 60 s on top of the PEI layer and dried for 1 h in N_2-filled glovebox. Finally, a 5 nm MoO_3 hole transport layer and 100 nm Ag top electrode were deposited by thermal evaporation under a vacuum pressure of 2 x 10^{-6} torr. The device area was 0.13 cm^2.

Solar cell characterization: The current density-voltage (*J-V*) characteristic curves of the solar cells were obtained using a Keithley 2401 source measurement unit under AM1.5G simulated illumination with standard power of 100 mW/cm^2. The intensity of the simulated sunlight was calibrated using a standard Si-photodiode detector with a KG-3 filter (Newport Co., Oriel). EQE spectra of each solar cell device were obtained using a solar cell spectral response/QE/IPCE measurement system (Newport Co., Oriel IQE-200B). The light intensity at each wavelength was calibrated using a standard, single-crystal Si-photovoltaic cell. The absorption spectra was measured by a UV/Vis spectrometer (Varian, Cary5000). Charge extraction (CE) was conducted using the CE analyzer function of an organic semiconductor parameter test system (McScience T4000) under 1.0 sun at V_{oc} conditions. The surface properties and morphologies of the pristine PEI and CQD doped PEI films were characterized by

NanoNavi II AFM system (SII Nano Technology Inc.) in tapping mode. The WF of ITO, pristine PEI and CQD doped PEI were measured by KPFM (KP 6500 Digital Kelvin probe, McAllister Technical Services. Co. Ltd). The AFM and KPFM samples were fabricated by spin-coating pristine PEI and CQD doped PEI on same ITO substrates which was used for solar cells fabrications. Non-modulated impedance spectroscopy was performed using an impedance analyzer (IVIUM Tech., IviumStat) under illumination conditions at an open circuit voltage in the frequency range between 0.1 Hz and 1.0 MHz.

4.3 Results and Discussion

Figure 4.1a show a schematic structural diagram of the carbon dot used in this study. CQDs were synthesized by a microwave-assisted hydrothermal method using neutral red (3-amino-7-dimethylamino-2-methylphenazine hydrochloride) and ethylenediamine. A detailed description of the fabrication of CQD is given in the experimental section. A high-resolution transmission electron microscopy (HR-TEM) image of the CQD is presented in **Figure 4.1b and 4.1c**. The TEM image shows homogeneously dispersed CQDs without any aggregation feature. The typical mean size of CQD was measured to be 3.6 ± 1.2 nm. The extend TEM image (inset of **Figure 4.1c**) shows a well-defined crystalline structure with an interlayer spacing of 0.21 nm, which corresponds to (100) lattice plane of graphite.[191,192]
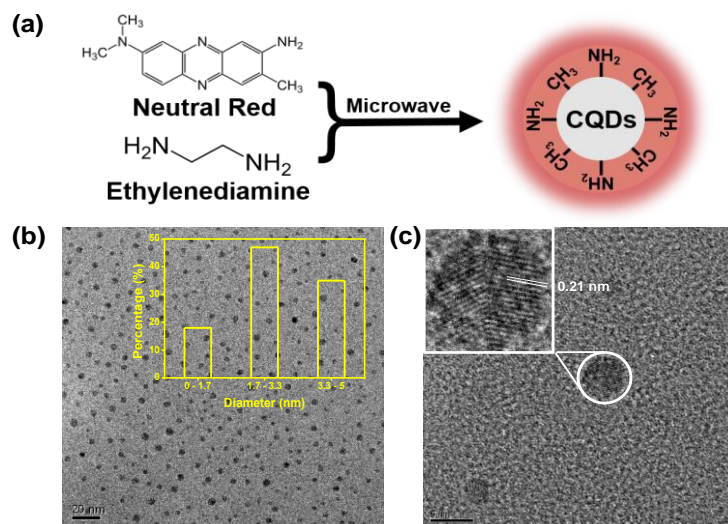
Figure 4.1. (a) Schematic diagram of CQD synthesis. (b) TEM images of CQDs. The typical mean size of the CQDs was 3.6 ± 1.2 nm. (c) HRTEM image showed the arrangement of carbon atoms in CQDs with a lattice spacing of 0.21 nm.

Initially, the effects of CQD doping on the PEI layer were investigated with single junction solar cells based on poly[4,8-bis(5-(2-ethylhexyl)thiophen-2-yl)benzo[1,2-b:4,5-b']dithiophene-alt-3-fluoro-thieno[3,4-b]thiophene-2-carboxylate] (PTB7-Th, also called PCE-10) and [6,6]-phenyl-C71-butyric acid methyl ester ($PC_{71}BM$). The CQD doped PEI layers were placed between the photo-active layer and the indium tin oxide (ITO) transparent electrode instead of the electron transport layer, as shown in schematic diagram of device structure (**Figure 4.2a**). **Figure 4.2b** shows the current density (J) - voltage (V) characteristics of PTB7-Th:$PC_{71}BM$ solar cells with pristine PEI layer or CQD doped PEI layer. To find the proper doping ratio, we varied the ratio of CQD from 0% to 10% by weight. Details related to the performance of these solar cells are listed in Table 4.1 and EQE spectra are presented in **Figure 4.2c**. The solar cell with pristine PEI layer yielded a PCE of 8.549% with a J_{SC} of 16.824 mA/cm^2, a V_{OC} of 0.783 V, and a fill factor (FF) of 0.649. The highest efficiency was obtained with PEI layer doped with 2% CQD. The best efficiency solar cell showed the PCE of 9.468% with a J_{SC} of 17.751 mA/cm^2, a V_{OC} of 0.781 V, and a FF of 0.683. A comparison of PV parameters between the device with the pristine PEI layer and the device with the CQD-doped PEI layer indicated that the performance enhancement in the solar cell with the CQD-doped PEI layer originated from J_{SC} and FF improvements.
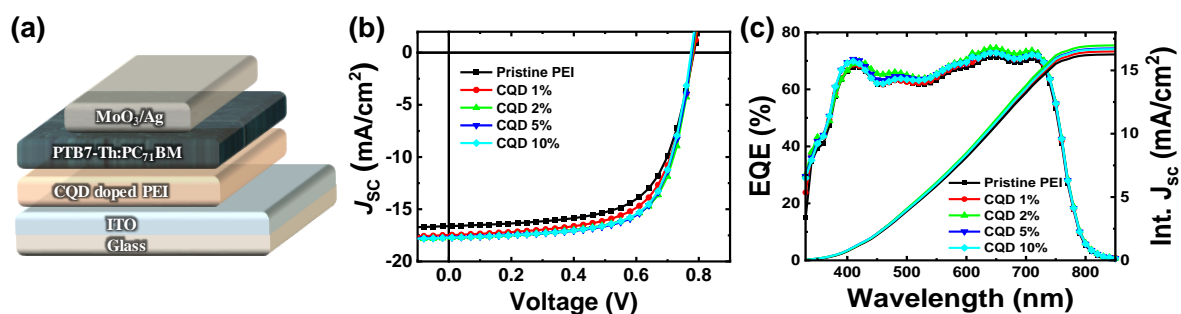
Figure 4.2. (a) Schematic illustration of device structure used in this study. (b) The *J-V* characteristics of PTB7-Th:PC$_{71}$BM solar cells with pristine PEI and CQD-doped PEI with various doping ratios, (c) EQE curves of PTB7-Th:PC$_{71}$BM solar cells with pristine PEI and CQD-doped PEI with various doping ratios.

Table 4.1. Summarized photovoltaic performance characteristics of PTB7-Th:PC$_{71}$BM solar cells with pristine PEI layer and CQD doped PEI layer with various doping ratios.

	V_{OC} [V]	J_{SC} [mA/cm^2]	EQE J_{SC} [mA/cm^2]	*FF*	η [%]	η_{avg} [%]	R$_s$ [Ωcm^2]
Pristine PEI	0.783	16.824	16.26	0.649	8.549	8.405 ($\pm$0.132)	5.68
CQD 1%	0.783	17.475	16.50	0.654	8.949	8.839 ($\pm$0.098)	4.83
CQD 2%	0.781	17.751	16.97	0.683	9.468	9.371 ($\pm$0.080)	3.61
CQD 5%	0.780	17.723	16.74	0.681	9.398	9.231 ($\pm$0.128)	3.74
CQD 10%	0.775	17.731	16.68	0.679	9.327	9.082 ($\pm$0.182)	3.87

In organic solar cells, performance improvement through interface engineering is primarily based on improving the charge transport characteristics. Additionally, improving the charge transport properties also entails a decrease in the rate of charge recombination due to less accumulation at the interface.[193-195] The PTB7-Th:PC$_{71}$BM solar cells with CQD-doped PEI layer showed all general effects of interface engineering. **Figure 4.3a** shows Nyquist plots of the non-modulated impedance spectroscopy measured under dark conditions for PTB7-Th:PC$_{71}$BM solar cells with a 2% CQD-doped PEI layer and pristine PEI layer. The solar cell with CQD-doped PEI layer exhibited significantly reduced series resistance. Because device fabrication parameters were identical for the two solar cells (with the exception of the CQD doping), the difference in the series resistance likely originated only from the modification of charge transport characteristics that was induced by doping. This reduction of series resistance resulted in an improvement of charge extraction property, as shown in **Figure 4.3b**. A direct comparison of charge extraction density calculated from charge extraction (CE) measurements between the devices with and without CQD-doping indicated that the device with CQD-doped PEI layer had enhanced charge extraction density.
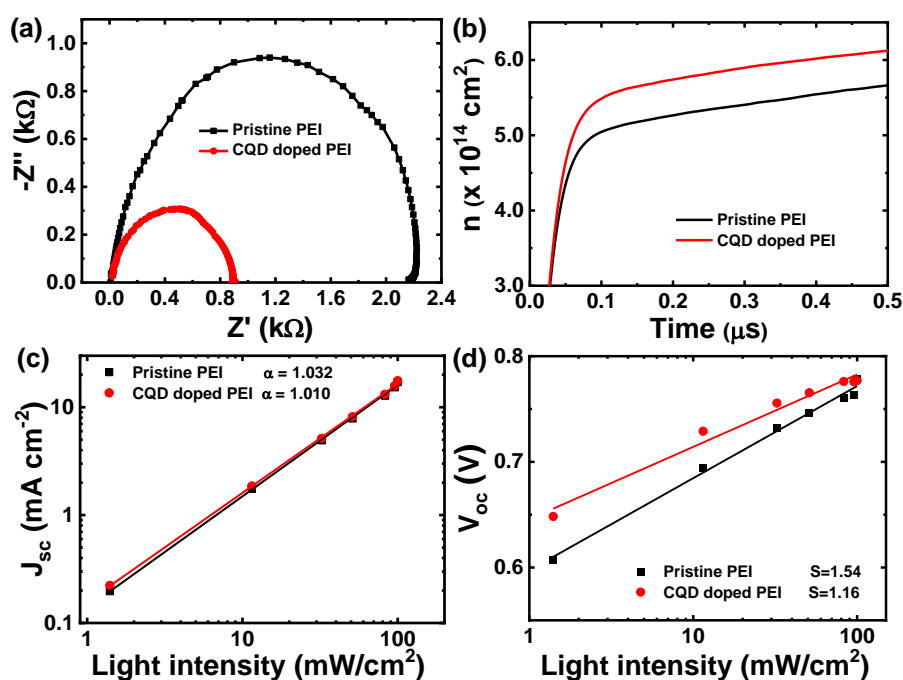
Figure 4.3. (a) Non-modulated impedance spectroscopy of PTB7-Th:PC$_{71}$BM solar cells with pristine PEI layer and CQD-doped PEI layer, (b) Charge extraction density of PTB7-Th:PC$_{71}$BM solar cells with pristine PEI layer and CQD-doped PEI layer, (c) J_{sc} versus light intensity for PTB7-Th:PC$_{71}$BM solar cells with pristine PEI layer and CQD-doped PEI layer, (d) V_{oc} versus light intensity for PTB7-Th:PC$_{71}$BM solar cells with pristine PEI layer and CQD-doped PEI layer.

To investigate the effect of the insertion of a CQD-doped PEI layer on recombination dynamics in solar cells, J_{SC} and V_{OC} vs. light intensity (I) were explored. Since J_{SC} and I have a power law relationship, $J_{SC} \propto I^\alpha$, bimolecular recombination becomes negligible under short-circuit conditions as α approaches 1.[196] As shown in **Figure 4.3c**, the fitted α values were 1.032 for the solar cell with pristine PEI layer and 1.010 for the solar cell with CQD-doped PEI layer, both close to 1, indicating that both the solar cell with pristine PEI layer and the solar cell with CQD-doped PEI layer were nearly free from bimolecular recombination loss. For the V_{OC} vs. light intensity, the slope of the line of best fit should be equal to 1.0(kT/q) in the absence of trap assisted recombination.[197] The extracted slope value was 1.54(kT/q) for the solar cell with pristine PEI layer. In the case of the solar cell with CQD-doped PEI layer, a much smaller slope value of 1.16(kT/q) was observed, indicating that trap-assisted recombination was significantly suppressed in the solar cell with CQD-doped PEI layer. Therefore, the enhanced *FF* was attributed to this reduced trap-assisted recombination property.

In order to confirm whether the enhancement of J_{SC} originated from the improved charge transport property alone, *J-V* curves were converted to net photocurrent density (J_{ph}) versus effective voltage (V_{eff}) as shown in **Figure 4.4a**. Dark current density (J_D) used to extract the J_{ph} (=J_L-J_D, where J_L is the current density measured under illumination) is plotted in **Figure 4.4b**. In general, saturation current density (J_{sat}) is governed by the incident photon flux only because saturation of J_{ph} means that all generated excitons are dissociated and collected without any bimolecular recombination. In this condition, the exciton generation rate (G_{max}) is given by $J_{sat} = q \cdot L \cdot G_{max}$, where q and L are the elementary charge and the thickness of the active layer, respectively. [198] In addition, the charge separation probability ($P(E,T)$) can be extracted using the ratio J_{ph}/J_{sat}.[199] Extracted G_{max} and $P(E,T)$ values are listed in **Table 4.2**. A comparison between the solar cell with pristine PEI layer and the solar cell with CQD-doped PEI layer indicated that both solar cells exhibited almost identical G_{max}. Interestingly, there was a huge increase in $P(E,T)$ from 86.7% for the solar cell with pristine PEI layer to 93.6% for the solar cell with CQD-doped PEI layer. Since the same photoactive layer was used, the same G_{max} value is predictable result. For the $P(E,T)$, since the charge transport characteristics and recombination characteristics have been improved in the solar cell with CQD-doped PEI layer, a slight increase in $P(E,T)$ can be expected to some extent, but the measured value was larger than expected.

$P(E,T)$ is basically influenced by charge collection efficiency and exciton dissociation efficiency. Although charge collection efficiency was enhanced slightly because of reduced trap-assisted recombination by CQD-doping, the increase in extraction charge density derived from CE measurements was somewhat insignificant. In addition, the increase in FF also was not quite noticeable, either. Therefore, the increase in $P(E,T)$ could not be attributed solely to transport enhancement. Since

the exciton generation rate was calculated to be the same in both solar cells, eventually, it is considered that the increase in J_{SC} was influenced by the increase in exciton dissociation efficiency. In general, factors that can affect exciton dissociation in a fixed donor-acceptor configuration ratio are BHJ active layer morphology and internal potential created by WF difference of electrodes. For the BHJ morphology, however, there are no significant factors affecting the active layer morphology in our study. In fact, there was no difference between the morphology of the pristine PEI surface and the CQD-doped PEI surface observed by AFM, and the morphologies of the active layers deposited thereon were almost identical, as shown in **Figure 4.5**. Therefore, the increase in exciton dissociation efficiency was not due to the BHJ morphological change.
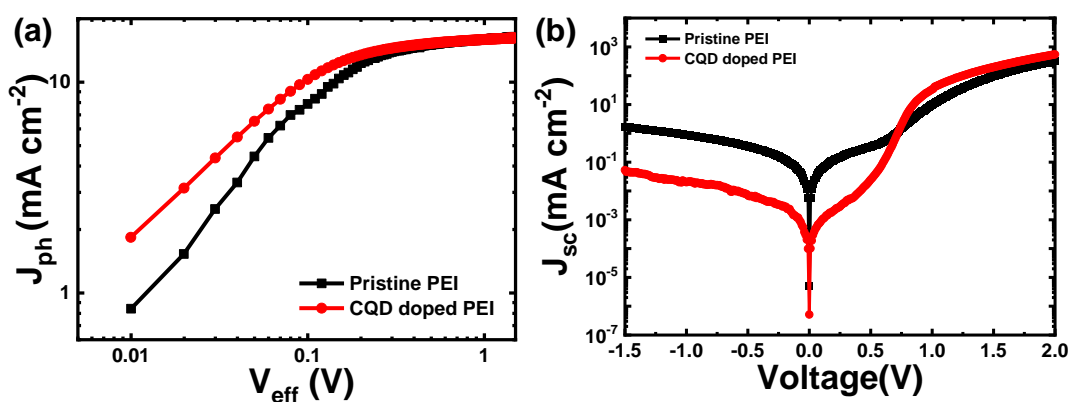
Figure 4.4. (a) Photocurrent density (J_{ph}) versus effective voltage (V_{eff}). (b) J-V measured under dark conditions.

Table 4.2. Exciton generation rate (G_{max}) and charge separation probabilities ($P(E,T)$) of PTB7-Th:PC$_{71}$BM solar cells with pristine PEI layer and CQD-doped PEI layer.

	Exciton generation rate G_{max} (m^{-3}s^{-1})	Exciton dissociation probability $P(E,T)$ (%)
Pristine PEI	1.04×10^{27}	86.7
CQD doped PEI	1.05×10^{27}	93.6
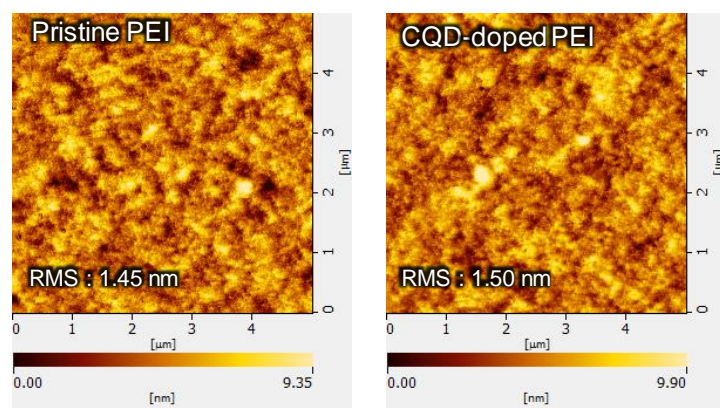
Figure 4.5. AFM images of the PTB7-Th:PC$_{71}$BM active layer deposited on pristine PEI layer (left) and CQD-doped PEI layer (right).

The remaining possibility that can increase exciton dissociation efficiency is an increase in internal potential due to the WF change. In terms of momentum space, the driving force for exciton dissociation depends on the energy difference between the lowest excited state in the donor and charge transfer state.[200] If this explanation is rewritten in terms of real space, the photo-generated excitons initially diffuse toward the donor-acceptor interface, and then electrons and holes can escape into their respective material phases. For each direction of escape, the exciton dissociation is supported by an effective internal electric field.[201,202] In short circuit condition (at 0 applied bias), an internal electric field is created by the WF difference between the cathode and anode.

In order to check the WF change by CQD-doping, we performed Kelvin-probe force microscopy (KPFM) measurements for the bare ITO, ITO with pristine PEI layer, and ITO with CQD-doped PEI layer. The measurement results are shown in the energy band diagram in **Figure 4.6a**. The WF of bare ITO was measured to be 4.7 eV, which was a typical value for commercial ITO. The PEI-coated ITO showed a significantly lower value of 4.28 eV, as reported in the previous literature.[83,188,203] For the ITO with CQD-doped PEI, there was a greater decrease of 4.13 eV in the WF values. This lower WF value is attributed to the NH$_2$ ligand used to stabilize CQD. In general, the PEI polymer is composed of amine groups in their backbone and side chains, and can therefore cause strong molecular dipoles between the PEI molecule and ITO surface.[182,204] These strong dipoles can shift the vacuum level, thereby reducing the WF of ITO. In our work, it was likely that there were many NH$_2$ ligands on the CQD surface function similar to amine groups in PEI, thereby strengthening their ability to reduce WF.

A summary of the concept is depicted in **Figure 4.6b**. Generally, internal built-in potential (V_{bi}) originates from the Fermi level (E_F) or work function difference between two electrodes in a metal-semiconductor-metal (MSM) type device architecture.[205,206] This V_{bi} can support the dissociation of

excitons generated by absorbed light.[201,202] Under short-circuit conditions, the E_F values of the two electrodes are forced to align and develop a uniform V_{bi} across the active layer. The commonly used electrodes in polymer solar cells, typically ITO and Al for the conventional structure or ITO and Ag for the inverted structure, relatively weak V_{bi} is developed. In the device with pristine PEI layer, relatively weak V_{bi} is developed. However, the solar cell with CQD-doped PEI layer has a stronger internal field due to a greater decrease in WF of ITO induced by amine ligands in CQD surface. This strengthened internal field induced better exciton dissociation efficiency, thereby improving solar cell performance.
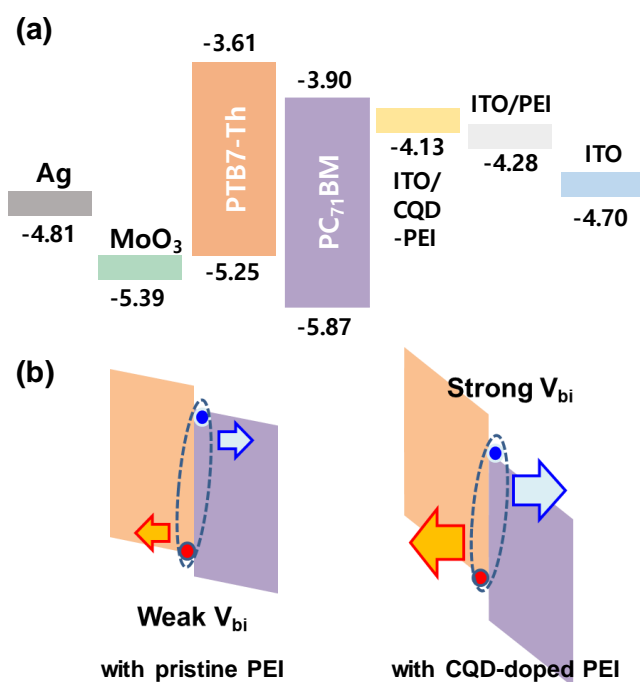
Figure 4.6. (a) Energy level diagram of PTB7-Th:PC$_{71}$BM solar cells. The work-functions of ITO, ITO with PEI, and ITO with CQD-doped PEI were measured by Kelvin-probe force microscopy. (b) Diagram of summarized concept; CQD-doped PEI induced stronger internal field due to the lower work-function. This strengthened internal field induced better exciton dissociation efficiency.

4.4 Conclusion

We have demonstrated enhanced photovoltaic performance of polymer solar cells based on PTB7-Th and PC$_{71}$BM by incorporation of CQD having NH$_2$ ligands into the PEI work-function modifying layer. A CQD-doped PEI layer provided substantial dynamic advantages in the operation of BHJ solar cells using the PEI layer as an ITO WF modifier. The solar cell with a CQD-doped PEI layer exhibited an average PCE of 9.37%, which represents a value nearly 11.3% higher than that of a solar cell with pristine PEI layer. This PCE improvement was primarily due to improvement of the electron extraction properties derived from CQD-doped PEI. Impedance spectroscopy clearly showed a significantly reduced series resistance in the solar cell with CQD-doped PEI layer. A study of net photocurrent density as a function of effective voltage showed that devices with CQD-doped PEI layer has a much higher charge separation probability compared to the device with pristine PEI layer. A Kelvin-probe force microscopy study demonstrated that a CQD-doped PEI layer induced lower work-function of ITO than that of ITO with pristine PEI, which induced a stronger internal field. This strengthened internal field induced better exciton dissociation efficiency. Consequently, it was concluded that the enhancement of solar cell efficiency could be attributed to the improved electron transport properties as a result of CQD doping and the increase in the exciton dissociation probability due to the strengthened internal field.

Chapter 5. Importance of interface engineering between the hole transport layer and the indium-tin-oxide electrode for high-efficient polymer solar cells

5.1 Research Background

Interface engineering is an essential technology for high performing bulk heterojunction (BHJ) organic photovoltaic (OPV) cells.[207-209] Since the initial studies of organic solar cells, the introduction of two important structure related technologies, the BHJ active layer and the charge transport layer, have induced significant improvement of OPVs in addition to the development of new donor and acceptor materials.[6,76,211] Many organic and inorganic materials that could function as hole and electron transport layers have been developed and studied to enhance the performance of OPVs. Among them, poly(3,4-ethylenedioxythiophene):poly(styrene sulfonate) (PEDOT:PSS) is the most widely used charge transfer layer even though it was the first used.[97,211] Initially, the purpose of the introduction of PEDOT:PSS was to improve the surface morphology of the indium tin oxide (ITO) electrode.[100] After the discovery that the introduction of PEDOT:PSS improved efficiency more than expected, many studies have been conducted to clarify the exact role of PEDOT:PSS. As a result, it has been found that the role of PEDOT:PSS is to improve not only interface morphology but also charge transfer characteristics, due to its high work function (WF) and relatively high electrical conductivity.[212,213]

Why PEDOT:PSS was chosen, of all potential materials? Firstly, PEDOT:PSS was a 'conducting' organic material. Although PEDOT:PSS was a relatively poor conductor, as an organic conducting polymer it was an ideal material to serve as a buffer between the semiconducting organic active layer and the conducting inorganic electrode.[214] Moreover, PEDOT:PSS had no absorption in the visible region, and it was solution processable, unlike other conductive polymers that were electrochemically synthesized.[215] Because of this background, the initial studies on the PEDOT:PSS layer mainly focused on increasing its electrical conductivity. It was simply expected that if the electrical conductivity was improved, the hole transport properties would also be improved. However, research found that the improvement in solar cell performance was always limited even when the conductivity of PEDOT:PSS was significantly enhanced. Instead, when a charge transport layer with high electrical conductivity was introduced, extra currents were induced by lateral transport from an area other than under the electrode, resulting in an over-estimate of cell efficiency. Since then, PEDOT:PSS with low-conductivity (known as AI4083, electrical conductivity: 10^{-3}-10^{-2} S/cm) was developed, and this low-conductivity PEDOT:PSS is now used in most devices.[216-218]

When using a high conductivity PEDOT:PSS (e.g., that of Baytron PH or Clevios P, with a conductivity of $10\text{-}10^2$ S/cm), it was assumed that the interface between ITO and PEDOT:PSS was an ohmic contact. Therefore, it was thought that interface problems related to PEDOT:PSS were mostly caused by the interface between the active layer and PEDOT:PSS. As a result, all the studies reported so far have been conducted in the direction of improving the hole transfer characteristics by increasing the electrical conductivity or further increasing the WF of the PEDOT:PSS surface contacting the active layer.[219-221] This research strategy did not change significantly even after low-conductivity PEDOT:PSS began to be used predominantly. However, the interface between low-conductivity PEDOT:PSS and ITO is no longer considered to be an ohmic contact. Instead, the interface between low-conductivity PEDOT:PSS and ITO is understood to be similar to the heterogeneous junction of organic polymers and inorganic conductors, so it is highly likely that the interface problem of the initial metal-insulator-metal solar cell was recreated. Of course, due to the high WF value of PEDOT:PSS, it has much better contact properties than direct contact between an active layer and ITO, but the interface problem between low-conductivity PEDOT:PSS and ITO is clearly a point that has been overlooked up to now.[116,118,120]

In this work, we introduced the use of a conjugated polyelectrolyte between the PEDOT:PSS hole transport layer (HTL) and the ITO bottom electrode to overcome the complicated organic-inorganic interface problem. To confirm the difference between low-conductivity PEDOT:PSS and high-conductivity PEDOT:PSS, three different types of commercial, PEDOT:PSS (AI4083, Clevios P, and PH1000) as well as a higher-conductivity PEDOT:PSS sample prepared by adding dimethyl sulfoxide (DMSO) were used in the experiment. The configuration of active materials did not have much influence on the interfacial problem between the HTL and the ITO electrode, but various donor-acceptor configurations, including both fullerene-based and non-fullerene-based BHJ mixtures, were utilized to confirm the unknown effect of the active layer. The conjugated polyelectrolyte used was potassium poly[9,9-bis(3′-sulfonatopropyl)fluorene-alt-(9-(2,7-diethylheptyl)-carboazole)] (WPFSCz-), which has good hole transport properties. In addition, to confirm whether the proposed idea was applicable not only to PEDOT:PSS but also to oxide-based charge transport layers, it was also applied to a solar cell using MoO_x and an inverted solar cell with ZnO.

5.2 Experimental

WPFSCz- Synthesis: All reagents and solvents were purchased from Aldrich, TCI Chemical Co., and Strem Chemicals Inc., and were used without further purification. 9-(2,7-Diethylheptyl)-2,7-

bis(4,4,5,5-tetramethyl-1,3,2-dioxaborolan-2-yl)-9H-carbazole, 2,7-dibromo-9,9-bis(4-sulfonatobutyl) fluorene dipotassium, and potassium poly[9,9-bis(3′-sulfonatopropyl)fluorene-*alt*-(9-(2,7-diethylheptyl)-carboazole)] (WPFSCz-) were prepared according to procedures described in the literature.[223-225]

Device Fabrication: ITO substrates were cleaned with detergent and ultrasonicated in acetone and isopropyl alcohol (IPA) for 15 min each. After a UV-ozone surface treatment, solutions with 0.01 wt% of WPFSCz- in distilled water and methanol (4:1) were spin-coated on ITO at 5000 rpm for 40 s and annealed at 100 °C for 10 min. An HTL of PEDOT:PSS (AI4083, Clevios P, PH1000, or PH1000 + 5% DMSO) was spin-coated at 5000 rpm for 40 s and annealed at 150 °C for 10 min. The thickness of the PEDOT:PSS layer was 40-50 nm. The substrates were then transferred to an N_2-filled glovebox. The active layer solution was made with a 1:1.2 ratio of PBDB-T-2F and Y6 in chloroform with 0.5% 1-chloronaphthalene as a processing additive to achieve a better phase-separated morphology. The active layer was deposited on top of the PEDOT:PSS layer by spin-coating at 5000 rpm for 40 s. A Phen-NaDPO solution (0.5 mg/ml in IPA) was spin-coated at 5000 rpm for 30 s on top of the PBDB-T-2F:Y6 layer as an electron transport layer. Finally, 100 nm of aluminum was deposited by thermal evaporation at a vacuum condition of 2×10^{-6} Torr. The device area was 0.13 cm^2.

Device Characterization: The power conversion efficiencies of the organic solar cells were measured by *J-V* curves using a Keithley 2401 source measurement unit under an AM 1.5G 100 mW/cm^2 spectra from a solar simulator (Newport Co., Oriel). To calibrate the intensity of the solar simulator, a standard Si-photodiode detector with a KG-3 filter (Newport Co., Oriel) was used. The external quantum efficiency (EQE) was measured using a quantum efficiency measurement system solar cell spectral response/QE/IPCE (Newport Co., Oriel IQE-200B). The light intensity at each wavelength was calibrated using a standard, single-crystal Si photovoltaic cell.

Conductivity measurements: The surface conductivities of PEDOT:PSS (AI4083, Clevios P, PH1000, and PH1000 + 5% DMSO) were determined using a Hall effect measurement system (Ecopia model No. HMS-5000). The thicknesses of the films were measured using a Dektak XT surface profiler. These samples were fabricated by spin-coating WPFSCz- and PEDOT:PSS on the same ITO substrates that were used for solar cell fabrication.

Kelvin probe force microscope (KPFM) measurements: The surface properties of the ITO, ITO with WPFSCz-, PEDOT:PSS, and PEDOT:PSS with WPFSCz- were characterized with a NanoNavi II AFM system (SII Nano Technology Inc.) in tapping mode. The WF of ITO, pristine PEI, and colloidal-quantum-dot-doped PEI were measured with a KPFM (KP 6500 Digital Kelvin probe, McAllister Technical Services. Co. Ltd). The samples for the KPFM measurements were fabricated in the same

way as the samples for the conductivity measurements.

Impedance Spectroscopy (IS) Measurements: Non-modulated IS, IMVS, and IMPS were performed using an impedance analyzer (IVIUM Tech., IviumStat) at an V_{OC} over a frequency range of 0.1 Hz to 1.0 MHz under illumination conditions with a red light emitting diode light source (λ = 635 nm).

Transient Photovoltage and Photocurrent Measurements: TPC and TPV measurements were conducted using the analyzer function of an organic semiconductor parameter test system (McScience T4000) at V_{OC} conditions under 1 sun illumination.

Ultraviolets Photoelectron Spectroscopy (UPS) Measurements: Photoelectron spectroscopies were carried out with an ESCALAB 250-XI surface analysis system equipped with a He discharge lamp providing He-I photons of 21.22 eV for UPS analysis and a monochromatic Al-Kα X-ray gun with photons energies of 1486.6 eV for X-ray photoelectron spectroscopy (XPS) characterization. The base vacuum pressure of the analysis system was ~10^{-7} torr. The Fermi edge was calibrated using a clean ITO film, and all spectra presented were plotted with respect to the determined Fermi level. All XPS measurements were calibrated with reference to the In $3d_{5/2}$ core level (443.9 eV) of a freshly prepared ITO film.

5.3 Results and Discussion

Figure 5.1 shows the chemical structure of the conjugated WPFSCz- polyelectrolyte and a schematic illustration of the solar cell structure used in this study. WPFSCz- has a similar backbone structure to PFN-based conjugated polyelectrolytes that are already widely used for surface modification of inorganic metal oxides such as ZnO and MoO$_3$.[226-228] Thus, we expected that it can be well combined with ITO, which is a similar oxide material. In addition, because WPFSCz- has a conjugated backbone, there would be no significant physical contact problems with the PEDOT:PSS surface. Details regarding the synthesis of WPFSCz- are provided in the Experimental Section. The prepared WPFSCz- was spin-coated onto the pre-cleaned ITO surface, and then an HTL layer was deposited by spin-coating. For the photoactive layer materials, we used PBDB-T-2F (also called PM6) donor and Y6 non-fullerene acceptor, which currently receive the most attention in OPV research. In addition, solar cells with a fullerene-based BHJ blend of PTB7-Th:PC71BM and with a non-fullerene-based BHJ blend of PTB7-Th:IEICO-4F were also tested.
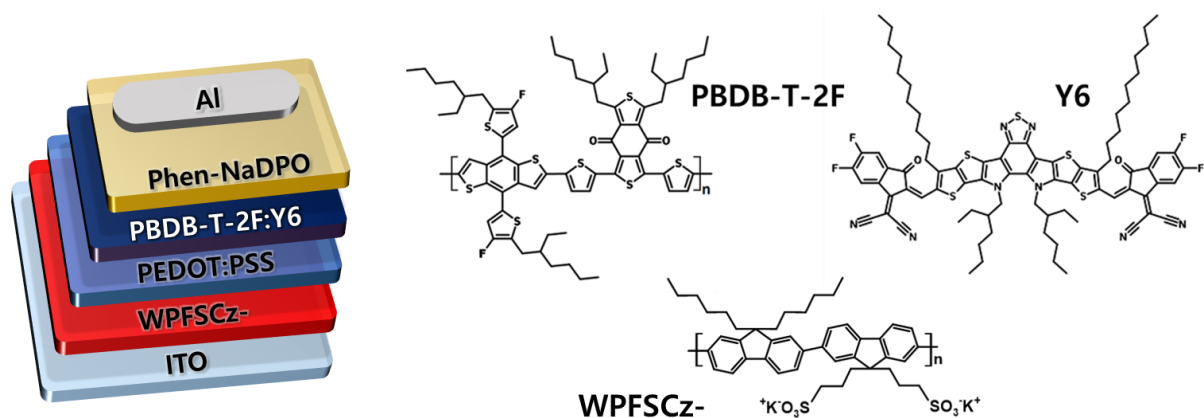
Figure 5.1. Schematic illustration of the device structure and chemical structure of the photoactive materials (donor: PBDB-T-2F (also called PM6), acceptor: Y6) and WPFSCz-.

Figure 5.2 shows the effect of the inserted WPFSCz- on current density (J)-applied voltage (V) characteristics according to the type of PEDOT:PSS. The conductivity values measured by the van der Pauw method were 0.005, 0.026, 6.849, and ~10^3 S/cm for the AI4083, Clevios P, PH1000, and PH1000 with 5% DMSO, respectively. In all cases, the solar cells with a WPFSCz- layer showed improved performance compared to the solar cells without a WPFSCz- layer. The difference in performance according to the presence or absence of WPFSCz- was greater when the conductivity of PEDOT:PSS was lower. For the AI4083, which showed the biggest difference, the PBDB-T-2F:Y6 solar cell without the WPFSCz- layer had a power conversion efficiency (PCE) of 15.86% with a short-circuit current density (J_{sc}) of 25.643 mA/cm^2, an open-circuit voltage (V_{oc}) of 0.864 V, and a fill factor (FF) of 71.58%, while the solar cell with the WPFSCz- layer had a PCE of 17.34% with a J_{sc} of 26.824 mA/cm^2, a V_{oc} of 0.864 V, and a FF of 74.83%. The details related to the performance of these solar cells are listed in **Table 5.1**. This performance difference almost disappeared as the conductivity was increased. The diminishing performance difference occurred because, as mentioned above, the contact problem between PEDOT:PSS and ITO became negligible as the conductivity of PEDOT:PSS increased. Instead, the problem seemed to have moved from the interface between PEDOT:PSS and ITO to the interface between PEDOT:PSS and the active layer. This was confirmed by the significantly improved performance caused by treatment of the interface between PEDOT:PSS and the active layer with hydroquinone (HQ) in a device using PH1000.[229]
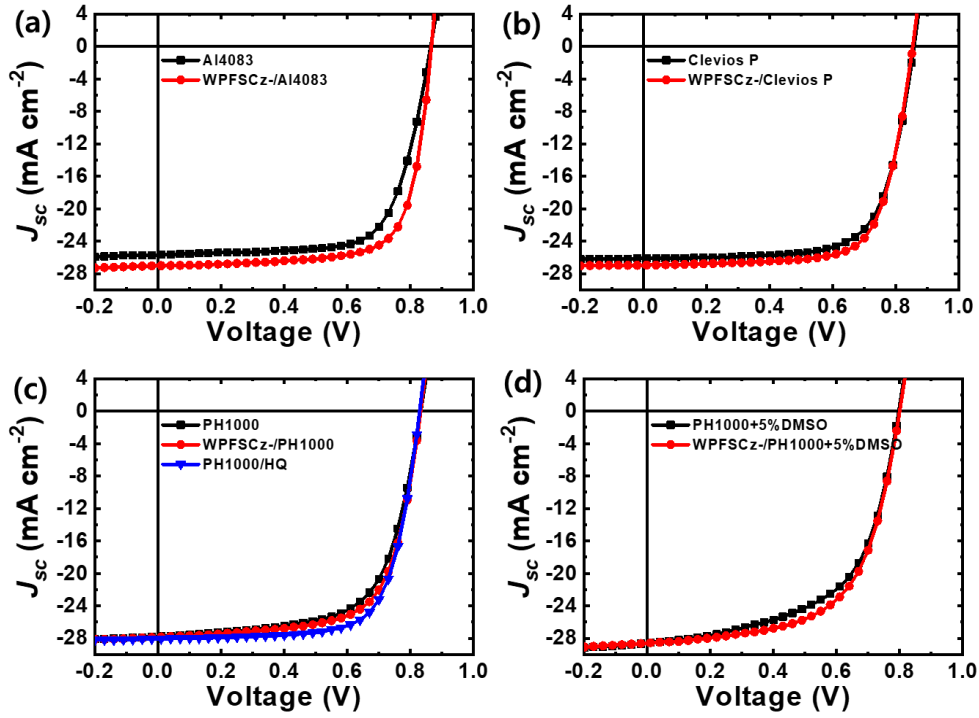
Figure 5.2. *J-V* characteristics of PBDB-T-2F:Y6 solar cells made with and without a WPFSCz- layer, based on different types of PEDOT:PSS: (a) AI4083, (b) Clevios P, (c) PH1000, and (d) PH1000 + 5% DMSO.

Table 5.1. Summarized photovoltaic performance characteristics of PBDB-T-2F:Y6 solar cells with and without a WPFSCz- layer based on various types of PEDOT:PSS. Average PCE values were obtained from 30 devices. EQE J_{sc} values were calculated from EQE measurements.

	V_{OC} [V]	J_{SC} [mA/cm^2]	EQE J_{SC} [mA/cm^2]	*FF*	η [%]	η_{avg} [%]	R_s [Ωcm^2]
ITO/AI4083	0.864	25.643	25.24	71.58	15.86	15.61 ($\pm$0.23)	43.2
ITO/ WPFSCz-/AI4083	0.864	26.824	26.12	74.83	17.34	17.12 ($\pm$0.21)	24.6
ITO/Clevios P	0.857	26.118	25.73	70.47	15.75	15.45 ($\pm$0.29)	41.1
ITO/ WPFSCz-/Clevios P	0.853	26.956	26.02	71.92	16.53	16.26 ($\pm$0.25)	40.4
ITO/PH1000	0.832	27.769	26.03	64.96	15.02	14.68 ($\pm$0.32)	45.7
ITO/ WPFSCz-/PH1000	0.832	27.850	26.21	67.85	15.72	15.39 ($\pm$0.31)	43.6
ITO/PH1000+5%DMSO	0.799	28.567	25.58	58.01	13.21	12.87 ($\pm$0.32)	37.8
ITO/WPFSCz-/PH1000+5%DMSO	0.800	28.588	25.84	61.07	13.96	13.62 ($\pm$0.31)	37.7

To explore the influence of the inserted WPFSCz- layer between ITO and PEDOT:PSS upon J_{sc} in detail, J-V curves were replotted with net photocurrent density (J_{ph}) *vs.* effective voltage (V_{eff}) using dark current density, as shown in **Figure 5.3**. A detailed theoretical background for J_{ph}-V_{eff} analysis is provided in previous work.[230,231] From the J_{ph}-V_{eff} analysis, the exciton generation rate (G_{max}) and the charge separation probability ($P(E,T)$) can be extracted using the relation $J_{sat} = q \cdot L \cdot G_{max}$ and the ratio J_{ph}/J_{sat}, where J_{sat} is saturation current density, and q and L are the elementary charge and the thickness of the active layer, respectively.[232] The extracted G_{max} and $P(E,T)$ values are listed in **Table 5.2**. In the case of G_{max}, the inserted WPFSCz- layer had no effect. However, $P(E,T)$ showed a markedly enhanced value in the device with the WPFSCz- layer. The degree of increase in $P(E,T)$ decreased as the conductivity of PEDOT:PSS increased. $P(E,T)$ is basically influenced by either the exciton dissociation efficiency or charge collection efficiency.[199,233] Because we used the same active layer, exciton dissociation efficiency would be the same for each device. Therefore, it can be said that the increase in *P(E,T)* mostly came from improvement of charge collection efficiency.
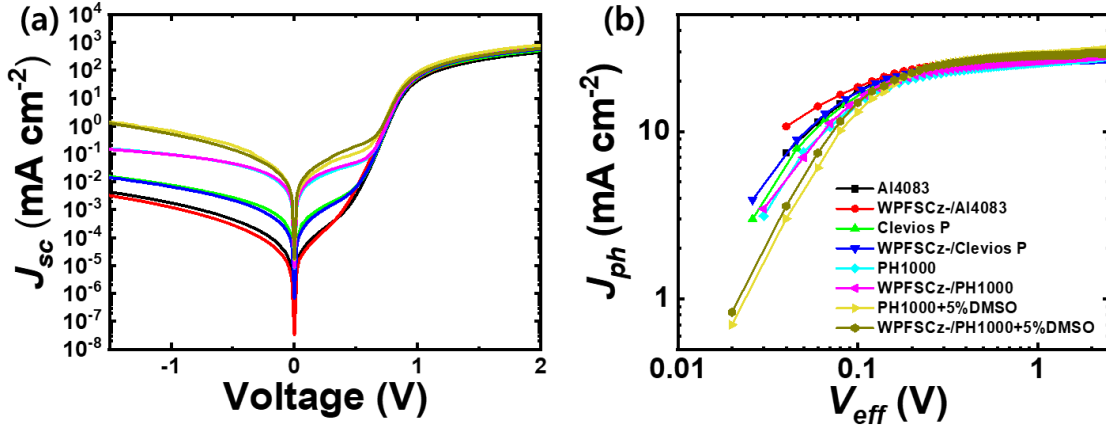
Figure 5.3. *J-V* measurements of PBDB-T-2F:Y6 solar cells based on PEDOT:PSS AI4083, Clevios P, PH1000, and PH1000 + 5% DMSO, both with and without a WPFSCz- layer. (a) Dark current density (J_{SC}). (b) Photocurrent density (J_{ph}) versus effective voltage ($V_{eff} = V_0 - V$).

Table 5.2. Summary of exciton generation rate (G_{max}) and charge separation probabilities ($P(E,T)$) of PBDB-T-2F:Y6 solar cells with and without a WPFSCz- layer using different types of PEDOT:PSS.

	Exciton generation rate G_{max} (m^{-3}s^{-1})	Exciton dissociation probability $P(E,T)$ (%)
AI4083	1.70×10^{28}	93.9
WPFSCz-/AI4083	1.73×10^{28}	97.3
Clevios P	1.67×10^{28}	93.6
WPFSCz-/Clevios P	1.71×10^{28}	94.7
PH1000	1.80×10^{28}	89.0
WPFSCz-/PH1000	1.82×10^{28}	90.6
PH1000+5%DMSO	1.85×10^{28}	85.4
WPFSCz-/PH1000+5%DMSO	1.86×10^{28}	87.2

The main factors affecting charge collection efficiency are charge recombination and charge extraction. First, by measuring the change of J_{sc} or V_{oc} depending on the intensity of the incident light, the change in charge recombination according to the insertion of a WPFSCz- layer was analyzed. In the J_{sc} vs. light intensity plots (**Figure 5.4a-d**), all of the fitted α values approached 1.0, indicating that all of the devices were nearly free from bimolecular recombination loss.[234,235] However, in V_{oc} vs. light intensity plots (**Figure 5.4e-h**), a clear difference was observed between solar cells with and without a WPFSCz- layer. In the case of solar cells using AI4083, the extracted slope value was 1.638 kT/q for the solar cell without a WPFSCz- layer, while a much smaller slope value of 1.303 kT/q was observed in the solar cell with a WPFSCz- layer. The reduced slope indicated that trap-assisted interfacial recombination was indeed suppressed by the insertion of a WPFSCz- layer. Consistent with other experimental results, this difference became smaller in the solar cell with higher conductivity PEDOT:PSS.
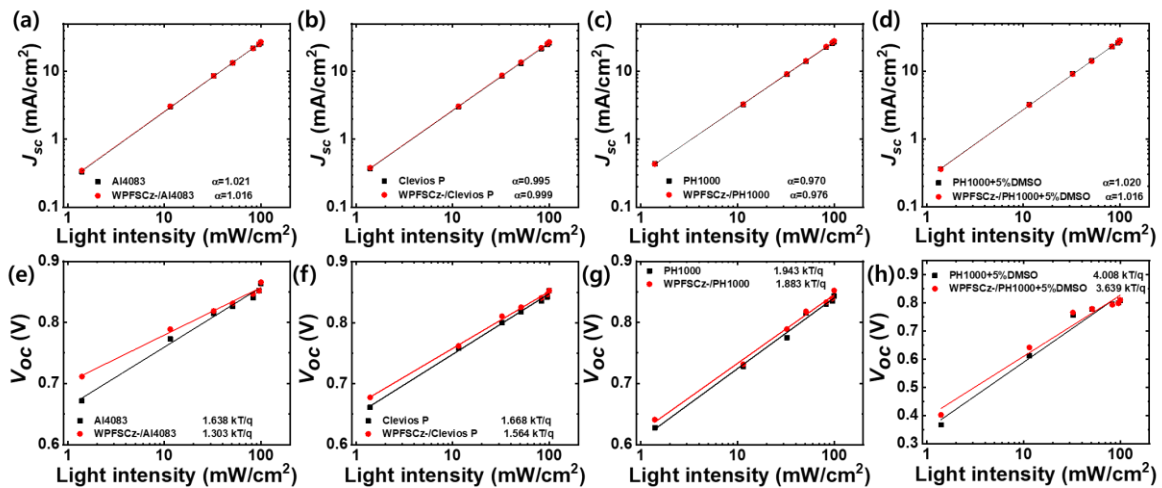
Figure 5.4. (a-d) J_{sc} versus light intensity for PBDB-T-2F:Y6 solar cells with and without WPFSCz- layer. (e-h) V_{oc} versus light intensity for PBDB-T-2F:Y6 solar cells with and without WPFSCz- layer. The device based on (a, e) AI4083, (b, f) clevios P, (c, g) PH1000, (d, h) PH1000+5% DMSO.

The improvement of the charge extraction ability by the reduction of trap-assisted interfacial recombination was also evident in many other characterization experiments. Transient photovoltage (TPV) and transient photocurrent (TPC) measurements were carried out to probe the difference of charge carrier dynamics between the solar cells with and without a WPFSCz- layer. The TPV measurements conducted under an open-circuit condition (**Figure 5.5a**) showed that the solar cell with a WPFSCz- layer beneath the PEDOT:PSS had a much longer decay time. In general, it is known that a voltage decrease in a TPV measurement is caused by the recombination of electrons and holes at defect sites.[236,237] Therefore, this longer decay time indicated that the recombination that occurred between ITO and AI4083 was effectively controlled by the insertion of a WPFSCz- layer. This also meant that the interfacial defect site that existed between ITO and AI4083 as a recombination location had been effectively removed by the WPFSCz- layer. Recalling that the performance improvement in the solar cell with a WPFSCz- layer was achieved by FF improvement, the TPV result showing a reduction in interfacial recombination was consistent with the *J-V* results. **Figure 5.5b** shows the photocurrent decay profile under a short circuit condition. The solar cell with a WPFSCz- layer exhibited a shorter decay time compared to the devices without a WPFSCz- layer.

The improved charge extraction capability due to the reduction of trap-assisted interfacial recombination by the insertion of a WPFSCz- layer can also be confirmed with impedance spectroscopy (IS) analysis.[168] Basically, non-modulated impedance spectroscopy (**Figure 5.5c**) showed clearly reduced series resistance in solar cell with WPFS-layer. In addition, intensity-modulated photocurrent spectroscopy (IMPS, **Figure 5.5d**) and intensity-modulated photovoltage spectroscopy (IMVS, **Figure 5.5e**) also showed reduced transit time (τ_{tran}) and significantly increased recombination time (τ_{rec}) in the solar cell with WPFS-layer (see **Table 5.3**). Charge collection efficiencies (η_c) obtained via the relation $\eta_c = 1 - (\tau_{tran}/\tau_{rec})$, were 96.5 and 92.9% for solar cells with and without a WPFSCz- layer, respectively.[238-240] These results were consistent with the results obtained from J_{ph}-V_{eff} analyses and internal quantum efficiency (IQE) measurements. To investigate directly the trap density change caused by the insertion of a WPFSCz- layer, the frequency-dependent capacitance was measured, and then the trap density was extracted from the derivative of the capacitance.[241] A comparison of the distributions of trap density extracted from the low frequency regions of the frequency-dependent capacitance (**Figure 5.5f**) showed that the trap density of the solar cell with a WPFSCz- layer was clearly lower than that of the solar cell without a WPFSCz- layer.
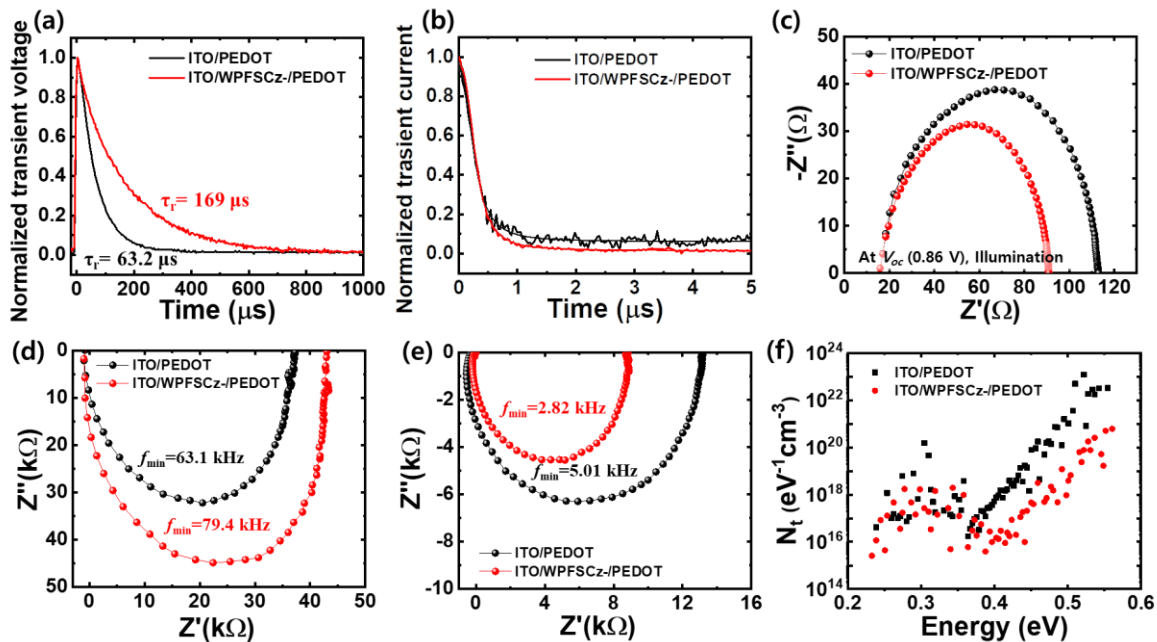
Figure 5.5. Photovoltage, photocurrent, and impedance spectroscopy measurements of PBDB-T-2F:Y6 solar cells with and without a WPFSCz- layer. (a) Transient photovoltage. (b) Transient photocurrent. (c) Non-modulated impedance spectroscopy. (d) Intensity-modulated photocurrent spectroscopy. (e) Intensity-modulated photovoltage spectroscopy. (f) Trap density vs. trap energy level.

Table 5.3. Summarized transit time (τ_{trap}), recombination time (τ_{rec}), and charge collection efficiency of PBDB-T-2F:Y6 solar cells made with and without a WPFSCz- layer.

	τ_{tran} (μs)	τ_{rec} (μs)	Charge collection efficiency (%)
PEDOT:PSS	2.52	31.8	92.9
WPFSCz-/PEDOT:PSS	2.00	56.4	96.5

To further investigate what kind of traps were eliminated by the insertion of a WPFSCz- layer, we conducted X-ray photoelectron spectroscopy (XPS). **Figure 5.6a** shows the O 1s spectra of ITO with and without a WPFSCz- layer. Because the thickness of the WPFSCz- layer deposited on the ITO was much thinner than the XPS skin-depth, most of the XPS peaks appeared to be due to the ITO layer, as evidenced by the In 3d and Sn 3d peaks, which were not from WPFSCz-. The O 1s spectrum in ITO is generally deconvoluted into three symmetric components.[242-244] The highest binding energy component at 532.8 eV (± 0.01 eV) is associated with the oxygen interacting with carbon (O-C) which is routinely observed even on clean ITO surfaces that have been exposed to air. The lowest binding energy component at 530.4 eV is assigned to the O-metal in lattice. The medium binding energy component at 531.7 eV (± 0.01 eV) corresponds to oxygen deficient regions, which are called oxygen vacancies (normally, O-H) acting as a defect/trap. The intensity of this oxygen vacancy peak clearly decreased with WPFSCz- layer deposition, meaning that the relative amounts of defects were decreased with WPFSCz- deposition.[245] Although the difference was reduced, the reason that trap-assisted recombination was reduced in all of the PEDOT:PSS in the V_{oc} *vs*. light-intensity experiment (**Figure 5.4**) was attributed to this reduction of trap sites.

In addition to removing defect sites, the deposition of the WPFSCz- layer modified the energy level and formed a cascading energy alignment, which was favorable for charge transport. The WF of pristine ITO was measured to be 4.65 eV. The WF of ITO covered with a WPFSCz- layer increased to 4.98 eV. The WF of AI4083 was measured to be 5.18 eV regardless of whether it was deposited directly on the ITO or a WPFSCz- layer was deposited on the ITO prior to the AI4083 being deposited. Furthermore, the surface potential difference also observed in the Kelvin probe force microscope (KPFM) measurement was caused by self-aligned surface electric dipoles.[246-248] The contact potential differences were measured with a cantilever tip coated with rhodium (WF = 4.72 eV) under a -600 mV bias as shown **Figure 5.7**. All KPFM images showed a uniform potential difference. The contact potential difference value of ITO had a positive value, which indicated that the Fermi level of ITO was lower than that of the biased tip, while the negative contact potential value indicated a higher Fermi level compared to the biased tip. When WPFSCz- was coated on the ITO surface, the contact potential difference value dramatically changed. A direct comparison between ITO/AI4083 and ITO/WPFSCz-/AI4083 indicated that insertion of WPFSCz- induced a higher contact potential difference. Consequently, benefiting from these cascade energy alignment and surface potential modification of ITO/WPFSCz-/AI4083 together with the defect elimination effect, the WPFSCz- layer improved the charge carrier extraction ability and the reduction of the extraction time as shown in the TPV, TPC, and IS measurements (**Figure 5.5a-c**).
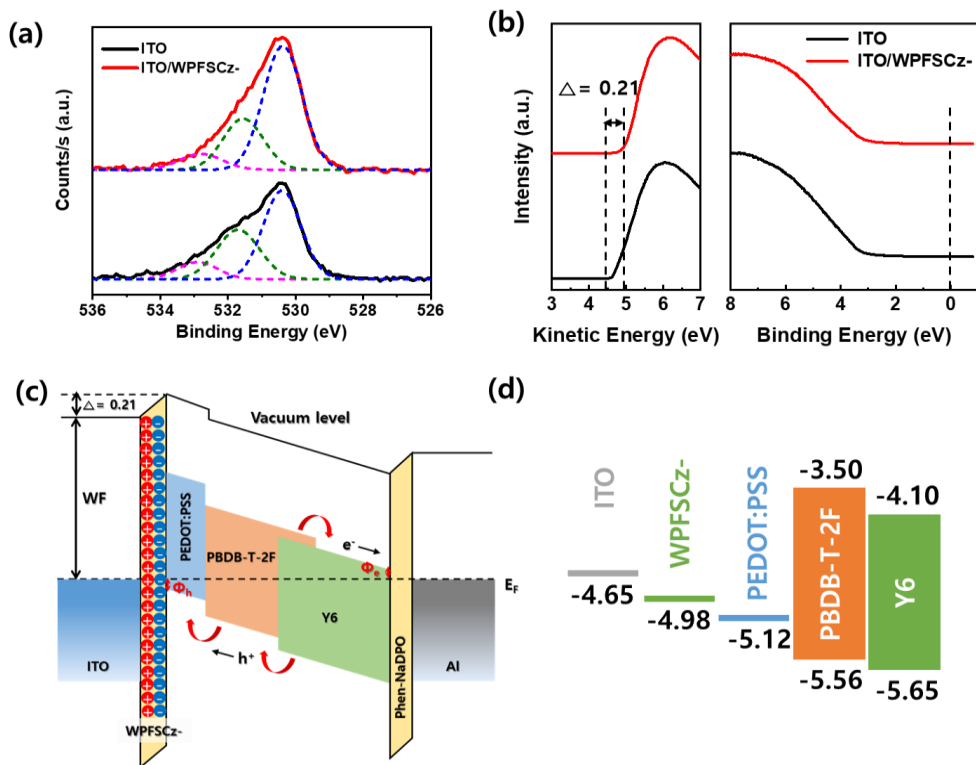
Figure 5.6. (a) X-ray photoelectron spectra of O 1s peaks obtained from ITO with and without a layer of WPFSCz-. (b) High binding region of ultraviolet photoelectron spectra of ITO with and without a WPFSCz-. (c) The corresponding energy level diagrams. (d) The energy level diagram of the components in the PBDB-T-2F:Y6 solar cells with a WPFSCz-layer.
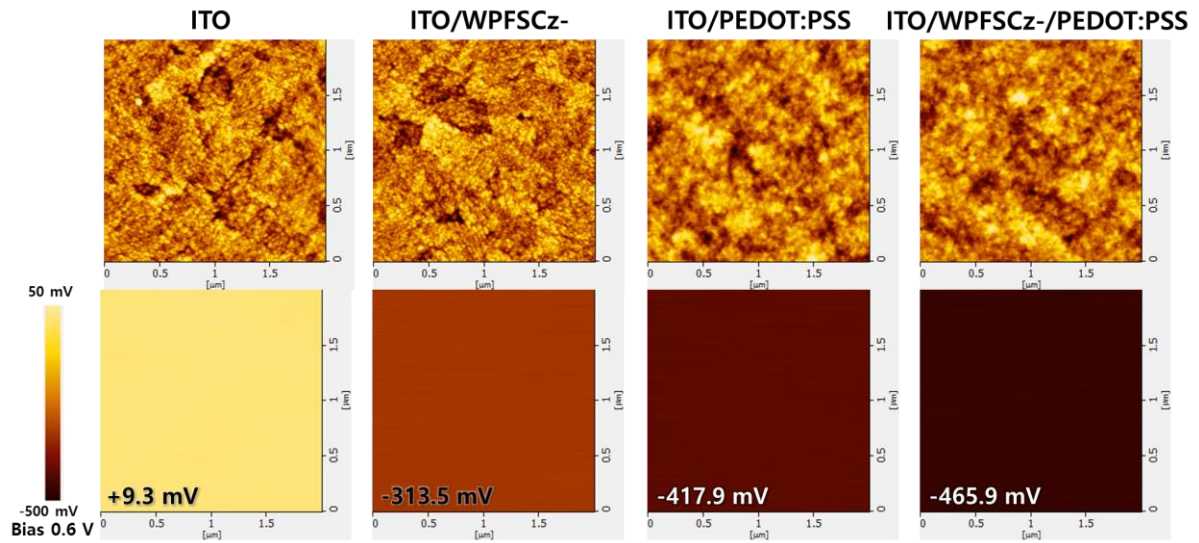
Figure 5.7. Surface potential images of (a) ITO, (b) ITO with WPFSCz-, (c) PEDOT:PSS on ITO, and (d) PEDOT:PSS on ITO with WPFSCz-.

Such interface problems seem to exist somewhat between ITO and low-conductivity PEDOT:PSS, as well as between a metal oxide-based charge transport layer and ITO. When we applied a WPFSCz- layer between MoO_x HTL and ITO, a similar improvement effect was observed (**Figure 5.8**). A solar cell with an inverted structure using a ZnO electron transport layer also exhibited the same improvement (**Figure 5.9**). In the case of ZnO, PFN-Br was utilized instead of WPFSCz- due to the energy level issue. The light intensity dependent V_{oc} experiment (see **Figure 5.4**) showed that trap-assisted recombination was reduced with the introduction of PFN-Br between ITO and ZnO. Therefore, it can be concluded that it was due to the same effect as using WPFSCz- under PEDOT:PSS.
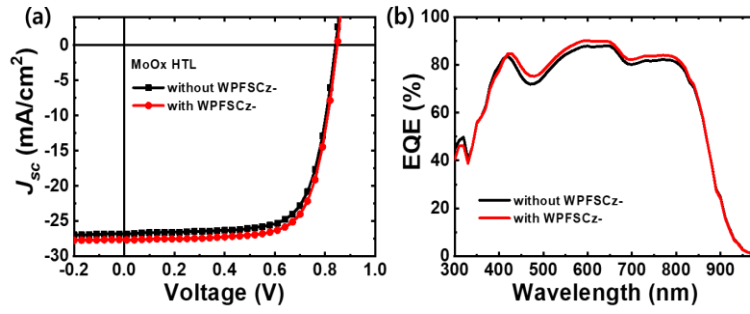
Figure 5.8. (a) The *J-V* characteristics, (b) EQE curves of PBDB-T-2F:Y6 inverted devices without and with WPFSCz- layer based on MoO$_x$ as HTL.

Table 5.4. Photovoltaic performance characteristics of PBDB-T-2F:Y6 solar cells without and with WPFSCz- layer based on various PEDOT:PSS.

	V_{OC} (V)	J_{SC} (mA/cm^2)	*FF*	η (%)
ITO/MoO$_x$	0.841	26.839	71.23	16.08
ITO/WPFSCz-/MoO$_x$	0.848	27.661	73.25	17.18
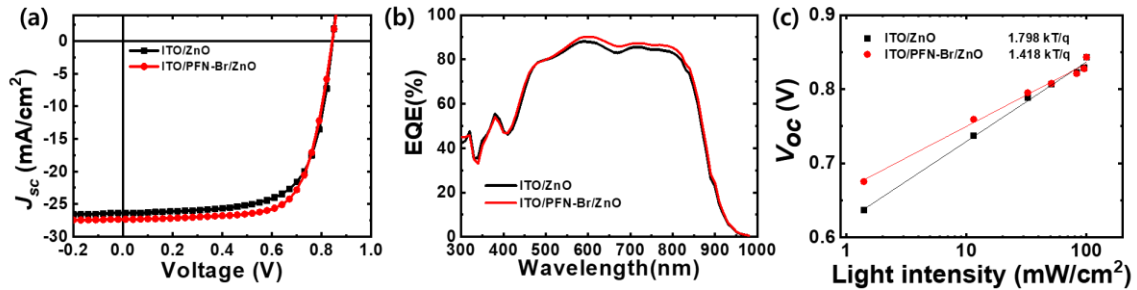
Figure 5.9. (a) The *J-V* characteristics, (b) EQE curves of PBDB-T-2F:Y6 inverted devices without and with PFN-Br layer, (c) V_{oc} versus light intensity for PBDB-T-2F:Y6 inverted devices without and with PFN-Br layer.

Table 5.5. Photovoltaic performance characteristics of PBDB-T-2F:Y6 inverted devices without and with PFN-Br layer.

	V_{OC} (V)	J_{SC} (mA/cm^2)	*FF*	η (%)
ITO/ZnO	0.844	26.372	68.33	15.21
ITO/PFN-Br/ZnO	0.843	27.341	70.49	16.22

5.4 Conclusion

We have employed a WPFSCz- conjugated polyelectrolyte layer to overcome the organic-inorganic interface problem between low-conductivity PEDOT:PSS (AI4083) and high-conductivity, inorganic ITO electrodes. The insertion of the WPFSCz- layer provided substantial advantages in the operation of non-fullerene-based polymeric solar cells. First, the inserted WPFSCz- layer reduced recombination losses at the interface by elimination of interfacial trap sites, resulting in an improvement in FF. Second, the deposition of the WPFSCz- layer modified the WF of ITO. WPFSCz- coated ITO had a WF value between the WF values of pure ITO and of PEDOT:PSS, thereby forming an effective cascading energy alignment, which is favorable for hole transport. Benefiting from the cascading energy alignment and the surface potential modification together with the defect elimination effect, the best PCE of a solar cell based on PM6 and Y6 significantly increased from 15.86 to 17.34%. In addition, we found that the problem of the interface in contact with ITO occurred not only in PEDOT:PSS but also in oxide-based charge transport layers. It was confirmed that insertion of the conjugated polyelectrolyte layer between a MoO_3 (or ZnO) charge transport layer and ITO showed the same results.

Chapter 6. Summary

In this thesis, various interfacial engineering methods which can be easily and effectively applied to charge transport layer for highly efficient organic solar cells are studied. The interface engineering through appropriate materials facilitates charge transfer by matching the energy levels, thereby reducing the interfacial resistance and carrier recombination probability.

In chapter 2, The introduction of poly(3,4-ethylenedioxythiophene):poly(styrenesulfonate) (PEDOT:PSS) as a standard hole transport layer greatly increased the efficiency of early organic solar cells. However, because PEDOT:PSS has a metallic property, it can still form a barrier by means of metal–semiconductor contact at its interface with the photoactive layer. In this study, we modified the PEDOT:PSS surface with hydroquinone (HQ) to remove that barrier. HQ treatment of the PEDOT:PSS surface lowered the hole transport barrier at the interface between the PEDOT:PSS and the active layer. In addition, because of the secondary doping effect of HQ, the sheet resistance of the PEDOT:PSS surface decreased by almost two orders of magnitude. As a result, the device fabricated with the HQ-modified PEDOT:PSS showed a 28% increase in efficiency compared to the device without HQ treatment. Modifying the PEDOT:PSS surface with HQ solution is an easy way to effectively boost the performance of polymer solar cells.

In chapter 3, The tunnel junction intermediate connection layer (ICL), which is the most critical component for high-efficient tandem solar cell, generally consists of hole conducting layer and polyethyleneimine (PEI) polyelectrolyte. However, because of the nonconducting feature of pristine PEI, photocurrent is open-restricted in ICL even with a little thick PEI layer. Here, high-efficiency homo-tandem solar cells are demonstrated with enhanced efficiency by introducing carbon quantum dot (CQD)-doped PEI on tunnel junction ICL. The CQD-doped PEI provides substantial dynamic advantages in the operation of both single-junction solar cells and homo-tandem solar cells. The inclusion of CQDs in the PEI layer leads to improved electron extraction property in single-junction solar cells and better series connection in tandem solar cells. The highest efficient solar cell with CQD-doped PEI layer in between indium tin oxide (ITO) and photoactive layer exhibits a maximum power conversion efficiency (PCE) of 9.49%, which represents a value nearly 10% higher than those of solar cells with pristine PEI layer. In the case of tandem solar cells, the highest performing tandem solar cell fabricated with C-dot-doped PEI layer in ICL yields a PCE of 12.13%; this value represents an ~15% increase in the efficiency compared with tandem solar cells with a pristine PEI layer.

In chapter 4, In addition to the phase-separated morphology of donor and acceptor, the internal field created by work-function difference between cathode and anode can also influence the exciton dissociation probability. In this study, we have demonstrated enhanced photovoltaic performance by

increasing exciton dissociation efficiency. To improve both work-function modification effect and charge transport properties, we have incorporated novel carbon quantum dots (CQD) having NH_2 ligands into the polyethyleneimine (PEI) work-function modifying layer as a dopant. A study of net photocurrent density as a function of effective voltage showed that devices with a CQD-doped PEI layer had a much higher charge separation probability compared to devices with a pristine PEI layer. A Kelvin-probe force microscopy study demonstrated that a CQD-doped PEI layer induced lower work-function of ITO than that of ITO with a pristine PEI, which induced a stronger internal field. This strengthened internal field induced better exciton dissociation efficiency, thereby improving solar cell performance.

In chapter 5, In early studies on organic solar cells with high conductivity PEDOT:PSS, the contact between ITO and PEDOT:PSS was considered ohmic. However, because low-conductivity PEDOT:PSS (such as AI4083) is mainly utilized in contemporary solar cells, the contact between ITO and PEDOT:PSS is not ohmic anymore. Despite the high possibility that there are serious interface problems, little attention has been paid to the interface between PEDOT:PSS and ITO. Most of the previous studies of interfaces in organic solar cells have focused on the interface between the active and charge transport layers. In this work, we have employed a conjugated polyelectrolyte that uses potassium poly[9,9-bis(3′-sulfonatopropyl)fluorene-alt-(9-(2,7-diethylheptyl)-carboazole)] (WPFSCz-) between ITO and low-conductivity PEDOT:PSS to overcome complicated organic-inorganic interfacial problems. Insertion of the WPFSCz- layer provides substantial advantages in the operation of the polymer solar cells. First, the inserted WPFSCz- layer modifies the work-function of the ITO, thereby forming effective cascading energy alignment, which is favorable for good hole transport. Second, the introduction of the WPFSCz- layer eliminates interfacial trap sites. The reduction in traps reduces recombination losses at the interface, resulting in an improvement in fill factor. These effects result in a significant increase in the efficiency of non-fullerene solar cells based on PM6 and Y6, from 15.86 to 17.34%. In addition, we have found that the problem of the interface in contact with ITO occurs not only in PEDOT:PSS, but also in oxide-based charge transport layers. We have confirmed that insertion of the WPFSCz- layer between ITO and an MoO_3 (or ZnO) charge transport layer shows the same positive results.

References

1. C. K. Chiang, C. R. Fincher, Jr., Y. W. Park, A. J. Heeger, H. Shirakawa, E. J. Louis, S. C. Gau, and Alan G. MacDiarmid, *Phys. Rev. Lett.*, 1978, **40**, 1472.

2. C. W. Tang, *Appl. Phys. Lett.*, 1986, **48**, 183.

3. M. Hiramoto, H. Fujiwara and M. Yokoyama, *Appl. Phys. Lett.*, 1991, **58**, 1062.

4. M. Hiramoto, H. Fujiwara and M. Yokoyama, *J. Appl. Phys.*, 1992, **72**, 3787.

5. N. S. Sariciftci, L. Smilowitz, A. J. Heeger and F. Wudl, *Science*, 1992, **285**, 1474.

6. G. Yu, J. Gao, J. C. Hummelen, F. Wudl and A. J. Heeger, *Science*, 1995, **270**, 1789.

7. Best Research-Cell Efficiency Chart (NREL) https://www.nrel.gov/pv/cell-efficiency.html

8. Q. Liu, Y. Jiang, K. Jin, J. Qin, J. Xu, W. Li, J. Xiong, J. Liu, Z. Xiao, K. Sun, S. Yang, X. Zhang and L. Ding, *J. Mater. Chem. A*, 2020, **8**, 8857-8861.

9. J. L. Wang, K. K. Liu, L. Hong, G. Y. Ge, C. Zhang and J. Hou, *ACS Energy Lett.*, 2018, **3**, 2967-2976.

10. Q. Fan, W. Su, S. Chen, W. Kim, X. Chen, B. Lee, T. Liu, U. A. Méndez-Romero, R. Ma, T. Yang, W. Zhuang, Y. Li, Y. Li, T.-S. Kim, L. Hou, C. Yang, H. Yan, D. Yu and E. Wang, *Joule*, 2020, **4**, 658-672.

11. H. Sun, X. Guo and A. Facchetti, *Chem.*, 2020, **6**, 1310-1326.

12. J. Gao, W. Gao, X. Ma, Z. Hu, C. Xu, X. Wang, Q. An, C. Yang, X. Zhang and F. Zhang, *Energy Environ. Sci.*, 2020, **13**, 958-967.

13. J. Y. Kim, K. Lee, N. E. Coates, D. Moses, T.-Q. Nguyen, M. Dante and A. J. Heeger, *Science*, 2007, **13**, 317.

14. L. Meng, Y. Zhang, X. Wan, C. Li, X. Zhang, Y. Wang, X. Ke, Z. Xiao, L. Ding, R. Xia, H.-L. Yip, Y. Cao and Y. Chen, *Science*, 2018, **361**, 1094-1098.

15. Q. An, J. Wang, W. Gao, X. Ma, Z. Hu, J. Gao, C. Xu, M. Hao, X. Zhang, C. Yang and F. Zhang, *Science Bulletin*, 2020, **65**, 538-545.

16. X. Ma, M. Luo, W. Gao, J. Yuan, Q. An, M. Zhang, Z. Hu, J. Gao, J. Wang, Y. Zou, C. Yang and F. Zhang, *J. Mater. Chem. A*, 2019, **7**, 7843-7851.

17. J. Yao, B. Qiu, Z.-G. Zhang, L. Xue, R. Wang, C. Zhang, S. Chen, Q. Zhou, C. Sun, C. Yang, M. Xiao, L. Meng and Y. Li, *Nat. Comm.*, 2020, **11**, 2726.

18. Q. Liao, Q. Kang, Y. Yang, C. B. An, B. W. Xu and J. H. Hou, *Adv. Mater.*, 2019, **31**, 1906557.

19. K. Lin, J. Wang, Z. Hu, R. Xu, J. Liu, X. Liu, B. Xu, F. Huang and Y. Cao, *Sol. Energy Mater. Sol. Cells*, 2017, **168**, 22-29.

20. P. Fu, L. Huang, W. Yu, D. Yang, G. Liu, L. Zhou, J. Zhang and C. Li, *Nano Energy*, 2015, **13**, 275-282.

21. A. Elfwing, W. Cai, L. Ouyang, X. Liu, Y. Xia, Z. Tang and O. Inganäs, *ACS Appl. Mater. Interfaces*, 2018, **10**, 9579–9586.

22. Q. An, J. Wang, X. Ma, J. Gao, Z. Hu, B. Liu, H. sun, X. Guo, X. L. Zhang and F. Zhang, *Energy Environ. Sci.*, 2020 Accepted Manuscript.

23. C. J. Brabec, S. Gowrisanker, J. J. M. Halls, D. Laird, S. Jia and S. P. Williams, *Adv. Mater.*, 2010, **22**, 3839-3856.

24. G. Yu and A. J. Heeger, *J. Appl. Phys.*, 1995, **78**, 4510-4515.

25. B. A. Collins, Z. Li, J. R. Tumbleston, E. Gann, C. R. Mcneill and H. Ade, *Adv. Energy Mater.*, 2013, **3**, 65-74.

26. N. Gasparini, A. Salleo, I. McCulloch and D. Baran, *Nat. Rev. Mater.*, 2019, **4**, 229-242.

27. H. Fu, Z. Wang and Y. Sun, *Sol. RRL*, 2017, **2**, 1700158.

28. T. Ameri, G. Dennler, C. Lungenschmied and C. J. Brabec, *Energy Environ. Sci.*, 2009, **2**, 347-363.

29. D. D. C. Rasi and R. A. J. Janssen, *Adv. Mater.*, 2019, **8**, 1806499.

30. T. Ameri, N. Li and C. J. Brabec, *Energy Environ. Sci.*, 2013, **6**, 2390-2413.

31. A. Gusain, R. M. Faria and P. B. Miranda, *Front. Chem.*, 2019, **7**, 41.

32. N. K. Elumalai and A. Uddin, *Energy Environ. Sci.*, 2016, **9**, 391-410.

33. C. M. Proctor, M. Kuik, T.-Q. Nguyen, *Prog. Polym. Sci.*, 2013, **38**, 1941-1960.

34. G.-J. A. H. Wetzelaer, M. Scheepers, A. M. Sempere, C. Momblona, J. Ávila and H. J. Bolink, *Adv. Mater.*, 2015, **27**, 1837-1841.

35. S. Khelifi, K. Decock, J. Lauwaert, H. Vrielinck, D. Spoltore, F. Piersimoni, J. Manca, A. Belghachi, and M. Burgelman, *J. Appl. Phys.*, 2011, **110**, 094509.

36. L. Zhang, X. Xing, L. Zheng, Z. Chen, L. Xiao, B. Qu and Q. Gong, *Sci. Rep.*, 2014, **4**, 5071.

37. O. O. Amusan, H. Louis, S. Zafarc, A. T. Hamzata and D. M. Peter, *Chem. Methodol.*, 2019, **3**, 425-441.

38. J. Huang, Z. Yin and Q. Zheng, *Energy Environ. Sci.*, 2011, **4**, 3861-3877.

39. B. Gholamkhass, N. M. Kiasari and P. Servati, *Org. Elec.*, 2012, **13**, 945-953.

40. R. Zhang, M. Zhao, Z. Wang, Z. Wang, B. Zhao, Y. Miao, Y. Zhou, H. Wang, Y. Hao, G. Chen and F. Zhu, *ACS Appl. Mater. Interfaces*, 2018, **10**, 4895-4903.

41. L. Nian, W. Zhang, N. Zhu, L. Liu, Z. Xie, H. Wu, F. Würthner and Y. Ma, *J. Am. Chem. Soc.*, 2015, **137**, 6995.

42. W. Yu, L. Huang, D. Yang, P. Fu, L. Zhou, J. Zhang and C. Li, *J. Mater. Chem. A*, 2015, **3**, 10660.

43. S. Nho, G. Baek, S. Park, B. R. Lee, M. J. Cha, D. C. Lim, J. H. Seo, S.-H. Oh, M. H. Song and S. Cho, *Energy Environ. Sci.*, 2016, **9**, 240.

44. X. Wen, A. Nowak-Krll, O. Nagler, F. Kraus, N. Zhu and N. Zheng, *Angew. Chem.*, 2019, **131**, 13185-13189.

45. Z. Lin, C. Jiang, C. Zhu, and J. Zhang, *ACS Appl. Mater. Interfaces*, 2013, **5**, 713-718.

46. S. Lattante, *Electronics*, 2014, **3**, 132-164.

47. D. H. Wang, J. K. Kim, J. H. Seo, I. Park, B. H. Hong, J. H. Park and A. J. Heeger, *Angew. Chem. Int. Ed.*, 2013, **52**, 2874.

48. Z. G. Yin, Q. D. Zheng, S.-C. Chen, J. X. Li, D. D. Cai, Y. L. Ma, J. J. Wei, *Nano Res.*, 2015, **8**, 456.

49. M. Y. Ameen S. Padhan, M. R. Suresh and V. S. Reddy, *Optical Meter.*, 2015, **39**, 134-139.

50.   P. L. Qin, G. J. Fang, W. J. Ke, F. Cheng, Q. Zheng, J. W. Wan, H. W. Lei and X. Z. Zhao, *J. Mater. Chem. A*, 2014, **2**, 2742.

51.   Z. A. Tan, D. P. Qian, W. Q. Zhang, L. J. Li, Y. Q. Ding, Q. Xu, F. Z. Wang and Y. F. Li, *J. Mater. Chem. A*, 2013, **1**, 657.

52.   Z. He, C. Zhong, X. Huang, W.-Y. Wong, H. Wu, L. Chen, S. Su and Y. Cao, *Adv. Mater.*, 2011, **23**, 4636.

53.   C.-Z. Li, C.-Y. Chang, Y. Zang, H.-X. Ju, C.-C. Chueh, P.-W. Liang, N. Cho, D. S. Ginger, A. K. Y. Jen, *Adv. Mater.*, 2014, **26**, 6262.

54.   F. Qin, W. Wang, L. Sun, X. Jiang, L. Hu, S. Xiong, T. Liu, X. Dong, J. Li, Y. Jiang, J. Hou, K. Fukuda, T. Someya and Y. Zhou, *Nat. Comm.*, 2020, **11**, 4508.

55.   K. Zhang, X.-Y. Liu, B.-W. Xu, Y. Cui, M.-L. Sun and J.-H. Hou, *Chinese J. Polym. Sci.*, 2017, **35**, 219-229.

56.   K. Sun, S. Zhang, P. Li, Y. Xia, X. Zhang, D. Du, F. H. Isikgor and J. Ouyang, *J. Mater Sci: Mater Electron*, 2015, **26**, 4438-4462.

57.   M. N. Gueye, A. Carella, J. Faure-Vincent, R. Demadrille and J.-P. Simonato, *Prog. Mater. Sci.*, 2020, **108**, 100616.

58.   S. Jäckle, M. Liebhaber, C. Gersmann, M. Mews, K. Jäger, S. Christiansen and K. Lips, *Sci. Rep.*, 2017, **7**, 2170.

59.   S. W. Baek, G. Park, J. Noh, C. Cho, C. H. Lee, M. K. Seo, H. Song and J. Y. Lee, *ACS Nano*, 2014, **8**, 3302.

60.   R. Peng, Z. Wan, W. Song, T. Yan, Q. Qiao, S. Yang, Z. Ge and M. Wang, *ACS Appl. Mater. Interfaces*, 2019, **11**, 42447-42454.

61.   S. R. Ha, S. Park, J. T. Oh, D. H. Kim, S. Cho, S. Y. Bae, D.-W. Kang, J.-M. Kim and H. Choi, *Nanoscale*, 2018, **10**, 13187-13193.

62.   J. Wang, H. Yu, C. Hou and J. Zhang, *ACS Appl. Mater. Interfaces*, 2020, **12**, 26543-26554.

63.   Q. Yang, S. Yu, P. Fu, W. Yu, Y. Liu, X. Liu, Z. Feng, X. Guo and C. Li, *Adv. Funct. Mater.*, 2020, **30**, 1910205.

64. M. Zeng, X. Wang, R. Ma, W. Zhu, Y. Li, Z. Chen, J. Zhou, W. Li, T. Liu, Z. He, H. Yan, F. Huang and Y. Cao, *Adv. Energy Mater.*, 2020, **10**, 2000743.

65. G. Li, R. Zhu and Y. Yang, *Nat. Photonics*, 2012, **6**, 153-161.

66. A. J. Heeger, *Adv. Mater.*, 2014, **26**, 10-27.

67. C. J. Brabec, N. S. Sariciftci and J. C. Hummelen, *Adv. Funct. Mater.*, 2001, **11**, 15-26.

68. M. Li, K. Gao, X. Wan, Q. Zhang, B. Kan, R. Xia, F. Liu, X. Yang, H. Feng, W. Ni, Y. Wang, J. Peng, H. Zhang, Z. Liang, H.-L. Yip, X. Peng, Y. Cao and Y. Chen, *Nat. Photonics*, 2017, **11**, 85-90.

69. M. G. Kang, H. J. Park, S. H. Ahn and L. J. Guo, *Sol. Energ. Mater. Sol. Cells*, 2010, **94**, 1179-1184.

70. W. Zhao, S. Li, H. Yao, S. Zhang, Y. Zhang, B. Yang, J. Hou, *J. Am. Chem. Soc.*, 2017, **139**, 7148-7151.

71. F. Zhao, S. Dai, Y. Wu, Q. Zhang, J. Wang, L. Jiang, Q. Ling, Z. Wei, W. Ma, W. You, C. Wang and X. Zhan, *Adv. Mater.*, 2017, **29**, 1700144.

72. C. E. Small, S. Chen, J. Subbiah, C. M. Amb, S.-W. Tsang, T.-H Lai, J. R. Reynolds and F. So, *Nat. Photonics*, 2012, **6**, 115-120.

73. H. J. Son, B. Carsten, I. H. Jung and L. Yu, *Energy Environ. Sci.*, 2012, **5**, 8158-8170.

74. C. Lee, H. Kang, W. Lee, T. Kim, K. H. Kim, H. Y. Woo, C. Wang and B. J. Kim, *Adv. Mater.*, 2018, **27**, 2466-2471.

75. W. Chen, M. P. Nikiforov and S. B. Darling, *Energy Environ. Sci.*, 2012, **5**, 8045-8074.

76. J. K. Lee, W. L. Ma, C. J. Brabec, J. Yuen, J. S. Moon, J. Y. Kim, K. Lee, G. C. Bazan and A. J. Heeger, *J. Am. Chem. Soc.*, 2008, **130**, 3619-3623.

77. Z. Lu, B. Jiang, X. Zhang, A. Tang, L. Chen, C. Zhan and J. Yao, *Chem. Mater.*, 2014, **26**, 2907-2914.

78. Y. Yan, F. Cai, L. Yang, J. Li, Y. Zhang, F. Qin, C. Xiong, Y. Zhou, D. G. Lidzey and T. Wang, *Adv. Mater.*, 2017, **29**, 1604044.

79. H. Zhou, Y. Zhang, J. Seifter, S. D. Collins, C. Luo, G. C. Bazan, T.-Q Nguyen, and A. J. Heeger, *Adv. Mater.*, 2013, **25**, 1646-1652.

80. Z. Yu, B. Li, J. Ouyang, *Adv. Funct. Mat.*, 2018, **28**, 1802554.

81. Y. Sun, J. H. Seo, C. J. Takacs, J. Seifter, A. J. Heeger, *Adv. Mater.*, 2011, **23**, 1679-1683.

82. S.-S. Li, K.-H. Tu, C.-C. Lin, C.-W. Chen and M. Chhowalla, *ACS Nano*, 2010, **4**, 3169-3174.

83. Y. Zhou, C. Fuentes-Hernandez, J. Shim, J. Meyer, A. J. Giordano, H. Li, P. Winget, T. Papadopoulos, H. Cheun, J. Kim, M. Fenoll, A. Dindar, W. Haske, E. Najafabadi, T. M. Khan, H. Sojoudi, S. Barlow, S. Graham, J.-L Bredas, S. R. Marder, A. Kahn and B. Kippelen, *Science*, 2012, **336**, 327-332.

84. Y. Sun, C. J. Takacs, S. R. Cowan, J. H. Seo, X. Gong, A. Roy and A. J. Heeger, *Adv. Mater.*, 2011, **23**, 2226-2230.

85. J. Y. Kim, S. H. Kim, H.-H. Lee, W. Ma, X. Gong and A. J. Heeger, *Adv. Mater.*, 2006, **18**, 572-576.

86. T. Gershon, *Mater. Sci. Technol.*, 2011, **27**, 1357-1371.

87. Z. Liang, Q. Zhang, L. Jiang and G. Cao, *Energy Environ. Sci.*, 2015, **8**, 3442-3476.

88. Z. Yin, J. Wei and Q. Zheng, *Adv. Sci.*, 2016, **3**, 1500362.

89. A. Duarte, K.-Y. Pu, B. Liu, G. C. Bazan, *Chem. Mater.*, 2011, **23**, 501-515.

90. J. H. Seo, A. Gutacker, Y. Sun, H. Wu, F. Huang, Y. Cao, U. Scherf, A. J. Heeger, G. C. Bazan, *J. Am. Chem. Soc.*, 2011, **133**, 8416-8419.

91. X. Li, W. Zhang, K. Usman, J. Fang, *Adv. Energy Mater.*, 2018, **107**, 1702730.

92. Y. Xue, P. Guo, H.-L. Yip, Y. Li and Y. Cao, *J. Mater. Chem. A*, 2017, **5**, 3780-3785.

93. Q. Zhang, W.-T. Wang, C.-Y. Chi, T. Wächter, J.-W. Chen, C.-Y. Tsai, Y.-C. Huang, M. Zharnikov, Y. Tai and D-J. Liaw, *Energy Environ. Sci.*, 2018, **11**, 682-691.

94. Y. Cai, L. Chang, L. You, B. Fan, H. Liu, Y. Sun, *ACS Appl. Mater. Interfaces*, 2018, **10**, 24082-24089.

95. H.-L. Yip and A. K.-Y. Jen, *Energy Environ. Sci.*, 2012, **5**, 5994-6011.

96. Z. Hu, J. Zhang, Z. Hao and Y. Zhao, *Sol. Energy Mater. Sol. Cells*, 2011, **95**, 2763-2767.

97. T. M. Brown, J. S. Kim, R. H. Friend and F. Cacialli, *Appl. Phys. Lett.*, 1999, **75**, 1679-1681.

98. S. R. Dupont, M. Oliver, F. C. Krebs and R. H. Dauskardt, *Sol. Energy Mater. Sol. Cells*, 2012, **97**, 171-175.

99. D. Yu, O. K. Oyewole, D. Kwabi, T. Tong, V. C. Anye, J. Asare, E. Rwenyagila, A. Fashina, O. Akogwu, J. Du and W. O. Soboyejo, *J. Appl. Phys.*, 2014, **116**, 074506.

100. A. C. Arias, M. Granstrom, D. S. Thomas, K. Petritsch and R. H. Friend, *Phys. Rev. B*, 1999, **60**, 1854-1860.

101. B. R. Lee, E. D. Jung, T. S. Nam, M. Jung, J. S. Park, S. Lee, H. Choi, S.-J. Kim, N. R. Shin, Y.-K. Kim, S. O. Kim, J. Y. Kim, H.-J. Shin, S. Cho and M. H. Song, *Adv. Mater.*, 2014, **26**, 494-500.

102. P. Fu, X. Guo, B. Zhang, T. Chen, W. Qin, Y. Ye, J. Hou, J. Zhang and C. Li, *J. Mater. Chem. A*, 2016, **4**, 16824-16829.

103. M.-H. Park, J.-H. Li A. Kumar, G. Li and Y. Yang, *Adv. Funct. Mater.*, 2009, **19**, 1241-1246.

104. S.-H. Liao, H.-J. Jhuo, P.-N. Yeh, Y.-S. Cheng, Y.-L. Li, Y.-H. Lee, S. Sharma and S.-A. Chen, *Sci. Rep.*, 2014, **4**, 6813.

105. L. K. Jagadamma, M. Al-Senani, A. El-Labban, I. Gereige, G. O. N. Ndjawa, J. C. D. Faria, T. Kim, K. Zhao, F. Cruciani, D. H. Anjum, M. A. McLachlan, P. M. Beaujuge and A. Amassian, *Adv. Energy Mater.*, 2015, **5**, 1500204.

106. J. H. Kim, P.-W. Liang, S. T. Williams, N. Cho, C.-C. Chueh, M. S. Glaz, D. S. Ginger, A. K.-Y. Jen, *Adv. Mater.*, 2015, **27**, 695-701.

107. C. Xie, L. Chen and Y. Chen, *J. Phys. Chem. C*, 2013, **117**, 24804-24814.

108. H. Choi, J. S. Park, E. Jung, G.-H. Kim, B. R. Lee, S. O. Kim, M. H. Song, H. Y. Woo and J. Y. Kim, *Adv. Mater.*, 2011, **23**, 2759-2763.

109. D. Liu, Y. Li, J. Yuan, Q. Hong, G. Shi, D. Yuan, J. Wei, C. Huang, J. Tang and M.-K. Fung, *J. Mater. Chem. A*, 2017, **5**, 5701-5708.

110. X.-Y. Li, L.-P. Zhang, F. Tang, Z.-M. Bao, J. Lin, Y.-Q. Li, L. Chen and C.-Q. Ma, *RSC Adv.*, 2016, **6**, 24501-24507.

111. C. Song, Z. Zhong, Z. Hu, J. Wang, L. Wang, L. Ying, J. Wang and Y. Cao, *Org. Elec.*, 2016, **28**, 252-256.

112. H. Liu, X. Li, L. Zhang, Q. Hong, J. Tang, A. Zhang and C.-Q. Ma, *Org. Elec.*, 2017, **47**, 220-227.

113. W. Xing, Y. Chen, X. Wu, X. Xu, P. Ye, T. Zhu, Q. Guo, L. Yang, W. Li and H. Huang, *Adv. Funct. Mater.*, 2017, **27**, 1701622.

114. B. Cao, X. He, C. R. Fetterly, B. C. Olsen, E. J. Luber and J. M. Buriak, *ACS Appl. Mater. Interfaces*, 2016, **8**, 18238-18248.

115. W. Zhang, B. Zhao, Z. He, X. Zhao, H. Wang, S. Yang, H. Wu, Y. Cao, *Energy Environ. Sci.*, 2013, **6**, 1956-1964.

116. A. Guerrero, L. F. Marchesi, P. P. Boix, S. Ruiz-Raga, T. Ripolles-Sanchis, G. Garcia-Belmonte and J. Bisquert, *ACS Nano,* 2012, **6**, 3453-3460.

117. P. P. Boix, J. Ajuria, I. Etxebarria, R. Pacios, G. Garcia-Belmonte and J. Bisquert, *J. Phys. Chem. Lett.*, 2011, **2**, 407-411.

118. J. Bisquert and G. Garcia-Belmonte, *J. Phys. Chem. Lett.*, 2011, **2**, 1950-1964.

119. S. Cho, S. H. Park and K. Lee, *J. Korean Phys. Soc.*, 2005, **47**, 474-478.

120. B. Xu, S.-A. Gopalan, A.-L Gopalan, N. Muthuchamy, k.-P. Lee, J.-S. Lee, S.-W. Lee, S.-W. Kim, J.-S. Kim, H.-M. Joeng, J.-B. Kwon, J.-H. Bae and S.-W. Kang, *Sci. Rep.*, 2017, **7**, 45079.

121. M. R. Lenze, N. M. Kronenberg, F. Wurthner and K. Meerholz, *Org. Elec.*, 2015, **21**, 171-176.

122. J. Bisquert, I. Mora-Sero and F. Fabregat-Santiago, *Chem. Electro. Chem.*, 2014, **1**, 289-296.

123. V. Gonzalez-Pedro, E. J. Juarez-Perez, W.-S. Arsyad, E. M. Barea, F. Fabregat-Santiago, I. Mora-Sero and J. Bisquert, *Nano Lett.*, 2014, **14**, 888-893.

124. X.Crispin, F. L. E. Jakobsson, A. Crispin, P. C. M. Grim, P. Andersson, A. Volodin, C. Haesendonck, M. Van der Auweraer, W. R. Salaneck and M. Berggren, *Chem. Mater.*, 2006, **18**, 4354-4360.

125.   J. Quyang, *Displays*, 2013, **34**, 423-436.

126.   D. McGillivray, J. P. Thomas, M. Abd-Ellah, N. F. Heinig, K. T. Leung, *ACS Appl. Mater. Interfaces*, 2016, **8**, 34303-34308.

127.   M. Donoval, M. Micjan, M. Novota, J. Nevrela, S. Kovacova, M. Pavuk, P. Juhasz, M. Jegalka, J. Kovac Jr., J. Jakabovic, M. Cigan and M. Weis, *Appl. Surf. Sci.*, 2017, **395**, 86-91.

128.   M. Wang, M. Zhou, L. Zhu, Q. Li and C. Jiang, *Solar Energy*, 2016, **129**, 175-183.

129.   C. Kvarnstrom, H. Neugebauer, A. Ivaska and N. S. Sariciftci, *J. Mol. Struct.*, 2000, **521**, 271-277.

130.   C. J. Brabec, S. Gowrisanker, J. J. M. Halls, D. Laird, S. J. Jia and S. P. Williams, *Adv. Mater.*, 2010, **22**, 3839.

131.   S. Nho, G. Baek, S. Park, B. R. Lee, M. J. Cha, D. C. Lim, J. H. Seo, S.-H. Oh, M. H. Song and S. Cho, *Energy Environ. Sci.*, 2016, **9**, 240.

132.   D. C. Lim, B. Y. Seo, S. Nho, D. H. Kim, E. M. Hong, J. Y. Lee, S.-Y. Park, C.-L. Lee, Y. D. Kim and S. Cho, *Adv. Energy Mater.*, 2015, **5**, 1500393.

133.   W. Zhao, S. Li, H. Yao, S. Zhang, Y. Zhang, B. Yang and J. Hou, *J. Am. Chem. Soc.*, 2017, **139**, 7148.

134.   X. Li, X. Liu, W. Zhang, H.-Q. Wang and J. Fang, *Chem. Mater.*, 2017, **29**, 4176.

135.   H. Zhou, Y. Zhang, C.-K. Mai, S. D. Collins, G. C. Bazan, T.-Q. Nguyen and A. J. Heeger, *Adv. Mater.*, 2015, **27**, 1767.

136.   H. Kim, J. H. Seo and S. Cho, *Appl. Phys. Lett.*, 2011, **99**, 213302.

137.   T. Ameri, N. Lia and C. J. Brabec, *Energy Environ. Sci.*, 2013, **6**, 2390.

138.   S. Sista, Z. Hong, L.-M. Chenx and Y. Yang, *Energy Environ. Sci.*, 2011, **4**, 1606.

139.   J. Y. Kim, K. Lee, N. E. Coates, D. Moses, T.-Q. Nguyen, M. Dante and A. J. Heeger, *Science*, 2007, **317**, 222.

140.   J.-H. Kim, J. B. Park, F. Xu, D. Kim, J. Kwak, A. C. Grimsdale and D.-H. Hwang, *Energy Environ. Sci.*, 2014, **7**, 4118.

141.   J. Gilot, M. M. Wienk and R. A. J. Janssen, *Adv. Mater.*, 2010, **22**, E67.

142. Y. Gao, V. Le Corre, A. Gaïtis, M. Neophytou, M. Abdul Hamid, K. Takanabe and P. M. Beaujuge, *Adv. Mater.*, 2016, **28**, 3366.

143. H. Kang, S. Kee, K. Yu, J. Lee, G. Kim, J. Kim, J.-R. Kim, J. Kong and K. Lee, *Adv. Mater.*, 2015, **27**, 1408.

144. N. T. Ho, H. N. Tien, S.-J. Jang, V. Senthilkumar, Y. C. Park, S. Cho and Y. S. Kim, *Sci. Rep.*, 2016, **6**, 30327.

145. G. Dennler, H.-J. Prall, R. Koeppe, M. Egginger, R. Autengruber and N. S. Sariciftci, *Appl. Phys. Lett.*, 2006, **89**, 073502.

146. A. Hadipour, B. de Boer, J. Wildeman, F. B. Kooistra, J. C. Hummelen, M. G. R. Turbiez, M. M. Wienk, R. A. J. Janssen and P. W. M. Blom, *Adv. Funct. Mater.*, 2006, **16**, 1897.

147. K. Kawano, N. Ito, T. Nishimori and J. Sakai, *Appl. Phys. Lett.*, 2006, **88**, 073514.

148. Y. Zhou, C. Fuentes-Hernandez, J. W. Shim, T. M. Khan and B. Kippelen, *Energy Environ. Sci.*, 2012, **5**, 9827.

149. J. Lee, H. Kang, J. Kong and K. Lee, *Adv. Energy Mater.*, 2014, **4**, 1301226.

150. Q. Wei, T. Nishizawa, K. Tajima and K. Hashimoto, *Adv. Mater.*, 2008, **20**, 2211.

151. K. Yao, L. Chen, X. Chen and Y. Chen, *Chem. Mater.*, 2013, **25**, 897.

152. S. van Reenen, S. Kouijzer, R. A. J. Janssen, M. M. Wienk and M. Kemerink, *Adv. Mater. Interfaces*, 2014, **1**, 1400189.

153. a) Y. Zhang, L. Chen, X. Hu, L. Zhang and Y. Chen, *Sci. Rep.*, 2015, **5**, 12839; b) H. Kang, J. Lee, S. Jung, K. Yu, S. Kwon, S. Hong, S. Kee, S. Lee, D. Kim and K. Lee, *Nanoscale*, 2013, **5**, 11587.

154. R. Sharma, F. Alam, A. K. Sharma, V. Dutta and S. K. Dhawan, *J. Mater. Chem. A*, 2015, **3**, 22227.

155. W. Kwon, G. Lee, S. Do, T. Joo and S.-W. Rhee, *Small*, 2014, **10**, 506.

156. X. Zhang, C. Liu, Z. Li, J. Guo, L. Shen, W. Guo, L. Zhang, S. Ruan and Y. Long, *Chem. Eng. J.*, 2017, **315**, 621.

157. L. Yan, Y. Yang, C.-Q. Ma, X. Liu, H. Wang and B. Xu, *Carbon*, 2016, **109**, 598.

158. Y. K. Jung, E. Shin and B.-S. Kim, *Sci. Rep.*, 2015, **5**, 18807.

159. Y. K. Jung, Y. Choi, B.-S. Kim, Carbon Nanomaterials for Biomedical Applications (Eds: M. Zhang, R. R. Naik, L. Dai), Springer International Publishing, Switzerland 2016, Ch. 10, pp. 299-317.

160. H. Zhu, W. Zhang and S. F. Yu, *Nanoscale*, 2013, **5**, 1797.

161. D. Qu, M. Zheng, L. Zhang, H. Zhao, Z. Xie, X. Jing, R. E. Haddad, H. Fan and Z. Sun, *Sci. Rep.*, 2014, **4**, 5294.

162. D. C. Lim, K.-D. Kim, S.-Y. Park, E. M. Hong, H. O. Seo, J. H. Lim, K. H. Lee, Y. Jeong, C. Song, E. Lee, Y. D. Kim and S. Cho, *Energy Environ. Sci.*, 2012, **5**, 9803.

163. J.-H. Kim, S. A. Shin, J. B. Park, C. E. Song, W. S. Shin, H. Yang, Y. Li and D.-H. Hwang, *Macromolecules*, 2014, **47**, 1613.

164. J.-H. Kim, C. E. Song, B. S. Kim, I.-N. Kang, W. S. Shin and D.-H. Hwang, *Chem. Mater.*, 2014, **26**, 1234.

165. J. You, C.-C. Chen, Z. Hong, K. Yoshimura, K. Ohya, R. Xu, S. Ye, J. Gao, G. Li and Y. Yang, *Adv. Mater.*, 2013, **25**, 3973.

166. Y. S. Liu, C.-C. Chen, Z. R. Hong, J. Gao, Y. Yang, H. P. Zhou, L. T. Dou, G. Li and Y. Yang, *Sci. Rep.*, 2013, **3**, 3356.

167. Y. Liu, J. R. Jennings, Y. Huang, Q. Wang, S. M. Zakeeruddin and M. Grätzel, *J. Phys. Chem. C*, 2011, **115**, 18847.

168. F. Fabregat-Santiago, G. Garcia-Belmonte, I. Mora-Seró and J. Bisquert, *Phys. Chem. Chem. Phys.*, 2011, **13**, 9083.

169. K. Adhitya, A. Alsulami, A. Buckley, R. C. Tozer and M. Grell, *IEEE J. Photovoltaics*, 2015, **5**, 1414.

170. Y. T. Set, B. Li, F. J. Lim, E. Birgersson and J. Luther, *Appl. Phys. Lett.*, 2015, **107**, 173301.

171. T. Kim, J.-H Kim, T. E. Kang, C. Lee, H. Kang, M. Shin, C. Wang, B. Ma, U. Jeong, T.-S. Kim and B. J. Kim, *Nat. Commun.*, 2015, **6**, 8547.

172. H. N. Tran, D. H. Kim, S. Park, S. Cho, *Curr. Appl. Phys.*, 2018, **18**, 534-540.

173. K.-S. Chen, J.-F. Salinas, H.-L. Yip, L. Huo, J. Hou and A. K.-Y. Jen, *Energy Environ. Sci.*, 2012, **5**, 9551-9557.

174. S. A. Hashemi, S. Ramakrishna and A. G. Aberle, *Energy Environ. Sci.*, 2020, **13**, 685-743.

175. T. Wang, R. Sun, M. Shi, F. Pan, Z. Hu, F. Huang, Y. Li and J. Min, *Adv. Energy Mater.*, 2020, **10**, 2000590.

176. M. S. Kumar, K. Mohanta and S. K. Batabyal, *Sol. Energy Mater. Sol. Cells*, 2017, **161**, 157-161.

177. C. Sun, F. Pan, H. Bin, J. Zhang, L. Xue, B. Qiu, Z. Wei, Z.-G. Zhang and Y. Li, *Nat. Commun.*, 2018, **9**, 743.

178. J. H. Seo, H. Kim and S. Cho, *Phys. Chem. Chem. Phys.*, 2012, **14**, 4062-4065.

179. H. You, L. Dai, Q. Zhang, D. Chen, Q. Jiang and C. Zhang, *Polymers*, 2018, **1**, 725.

180. F. Wang, B. Zhang, Q. Li, Z. Shi, L. Yu, H. Liu, Y. Wang, S. Dai, Z. Tan and Y. Li, *J. Mater. Chem. A*, 2016, **4**, 1915.

181. A. C. Hinckley, C. Wang, R. Pfattner, D. Kong, Y. Zhou, B. Ecker, Y. Gao and Z. Bao, *ACS Appl. Mater. Interfaces*, 2016, **8**,19658

182. K. Yao, L. Chen, Y. Chen, F. Li, X. Ren, H. Wang, Y. Li, *Polym. Chem.*, 2012, **3**, 710.

183. X. Li, X. Liu, P. Sun, Y. Feng, H. Shan, X. Wu, J. Xu, C. Huang, Z.-K. Chen, Z.-X. Xu, *RSC Adv.*, 2017, **7**, 17076.

184. E. Yalcin, M. Can, C. Rodriguez-Seco, E. Aktas, R. Pudi, W. Cambarau, S. Demic and E. Palomares, *Energy Environ. Sci.*, 2019, **12**, 230.

185. Z. Liu and n. Wang, *J. Mater. Chem. A*, 2020, **8**, 3211.

186. Z. Lin, J. Chang, C. Zhang, D. Chen, J. Wu and Y. Hao, *J. Phys. Chem. C*, 2017, **121**, 10275.

187. Y. Zhou, C. Fuentes-Hernandez, J. W. Shim, T. M. Khan and B. Kippelen, *Energy Environ. Sci.*, 2012, **5**, 9827-9832.

188. R. Kang, S. Park, Y. K. Jung, D. C. Lim, M. J. Cha, J. H. Seo and S. Cho, *Adv. Energy Mater.*, 2012, **8**, 1702165.

189. P. Fan, D. Zhang, Y. Wu, J. Yu and T. P. Russell, *Adv. Funct. Mater.*, 2020, **30**, 2002932.

190. Z. Ling, Y. Zhao, S. Wang, S. Pan, H. Lian, C. Peng, X. Yang, Y. Liao, W. Lan, B. Wei and G. Chen, *J. Mater. Chem. C*, 2019, **7**, 9354-9361.

191.   S. N. Baker and G. A. Baker, *Angew. Chem. Int. Ed.*, 2010, **49**, 6726-6744.

192.   H. Yang, Y. Liu, Z. Guo, B. Lei, J. Zhuang, X. Zhang, Z. Liu and C. Hu, *Nat. Commun.*, 2019, **10**, 1789.

193.   P. Li, B. Wu, Y. C. Yang, H. S. Huang, X. D. Yang, G. D. Zhou and Q. L. Song, *Sol. Energy*, 2018, **170**, 212-216.

194.   Y. Wang, Z. Liang, J. Qin, J. Tong, P. Guo, X. Cao, J. Li and Y. Xia, *IEEE J. Photovoltaics*, 2019, **9**, 1678-1685.

195.   W. Lan, Y. Liu, B. Wu, B. Xu, H. Pu, B. Wei, Y. Peng, W. Tian and F. Zhu, *ACS Appl. Energy Mater.*, 2019, **2**, 7385-7392.

196.   L. J. A. Koster, V. D. Mihailetchi, H. Xie and P. W. M. Blom, *Appl. Phys. Lett.*, 2005, **87**, 203502.

197.   L. J. A. Koster, V. D. Mihailetchi, R. Ramaker, P. W. M. Blom, *Appl. Phys. Lett.*, 2005, **86**, 123509.

198.   L. Zhang, X. Xing, L. Zheng, Z. Chen, L. Xiao, B. Qu and Q. Gong, *Sci. Rep.*, 2015, **4**, 5071.

199.   J.-L. Wu, F.-C. Chen, Y.-S. Hsiao, F.-C. Chien, P. Chen, C.-H. Kuo, M. H. Huang and C.-S. Hsu, *ACS Nano*, 2011, **5**, 959-967.

200.   D. Qian, Z. Zheng, H. Yao, W. Tress, T. R. Hopper, S. Chen, S. Li, J. Liu, S. Chen, J. Zhang, X.-K Liu, B. Gao, L. Ouyang, Y. Jin, G. Pozina, I. A. Buyanova, W. M. Chen, O. Inganäs, V. Coropceanu, J.-L. Bredas, H. Yan, J. Hou, F. Zhang, A. A. Bakulin and F. Gao, *Nat. Mater.*, 2018, **17**, 703-709.

201.   A. Petersen, A. Ojala, T. Kirchartz, T. A. Wagner, F. Würthner and U. Rau, *Phys. Rev. B*, 2012, **85**, 245208.

202.   H. Tamura and I. Burghardt, *J. Phys. Chem. C*, 2013, **117**, 15020-15025.

203.   L. Yan, Y. Song, Y. Zhou, B. Song and Y. Li, *Org. Electron.*, 2015, **17**, 94-101.

204.   Y.-H. Kim, T.-H. Han, H. Cho, S.-Y. Min, C.-L. Lee and T.-W. Lee, *Adv. Funct. Mater.*, 2014, **24**, 3808-3814.

205.   C. J. Brabec, A. Cravino, D. Meissner, N. S. Sariciftci, T. Fromherz, M. T. Rispens, L. Sanchez and J. C. Hummelen, *Adv. Funct. Mater.*, 2001, **11**, 374-380.

206.   S. Chen, J. R. Manders, S.-W. Tsang and F. So, *J. Mater. Chem.*, 2012, **22**, 24202-24212.

207.   F. Jin, Z. Su, B. Chu, P. Cheng, J. Wang, H. Zhao, Y. Gao, X. Yan and W. Li, *Sci. Rep.*, 2016, **6**, 26262.

208.   C. Sun, Z. Wu, Z. Hu, J. Xiao, W. Zhao, H.-W. Li, Q.-Ya Li, S.-W. Tsang, Y.-X. Xu, K. Zhang, H.-L. Yip, J. Hou, F. Huang, Y. Cao, *Energy Environ. Sci.*, 2017, **10**, 1784-1791.

209.   F. Pan, C. Sun, Y. Li, D. Tang, Y. Zou, X. Li, S. Bai, X. Wei, M. Lv, X. Chen and Y. Li *Energy Environ. Sci.*, 2019, **12**, 3400-3411.

210.   L. S. Roman, M. Berggren, and O. Inganäs, *Appl. Phys. Lett.*, 1999, **75**, 3557.

211.   F. Zhang, M. Johansson, M.R. Andersson, J.C. Hummelen and O. Inganäs, *Adv. Mater.*, 2002, **14**, 662-665.

212.   T. Aernouts, W. Geens, J. Poortmans, P. Heremans, S. Borghs and R. Mertens, *Thin Solid Films*, 2002, **403**, 297-301.

213.   T. M. Brown, J. S. Kim, R. H. Friend, F. Cacialli, R. Daik and W. J. Feast, *Synthetic Metals*, 2000, **111**, 285-287.

214.   L. Ding, M. Jonforsen, L. S Roman, M. R. Andersson and O. Inganäs, *Synthetic Metals*, 2000, **110**, 133-140.

215.   M. Lefebvre, Z. Qi, D. Rana and P. G. Pickup, *Chem. Mater.*, 1999, **11**, 262-268.

216.   M. Cui, D. Li, X. Du, N. Li, Q. Rong, N. Li, L. Shui, G. Zhou, X. Wang, C. J. Brabec and Li Nian, *Adv. Mater.*, 2020, **32**, 2002973.

217.   X. Fan, W. Nie, H. Tsai, N. Wang, H. Huang, Y. Cheng, R. Wen, L. Ma, F. Yan and Y. Xia, *Adv. Sci.*, 2019, **6**, 1900813.

218.   K. Jiang, Q. Wei, J. Yuk, L. Lai, Z. Peng, H. K. Kim, J. Yuan, L. Ye, H. Ade, Y. Zou and H. Yan, *Joule*, 2019, **3**, 1-14.

219.   Z. Zhao, Q. Wu, F. Xia, X. Chen, Y. Liu, W. Zhang, J. Zhu, S. Dai and S. Yang, *ACS Appl. Mater. Interfaces*, 2015, **7**, 1439-1448.

220. M. Zeng, X. Wang, R. Ma, W. Zhu, Y. Li, Z. Chen, J. Zhou, W. Li, T. Liu, Z. He, H. Yan, F. Huang and Y. Cao, *Adv. Energy Mater.*, 2020, **10**, 2000743.

221. C. S. Pathak, J. P. Singh, and R. Singha, *Appl. Phys. Lett.*, 2017, **111**, 102107.

222. B. Xu, S.-A. Gopalan, A.-L. Gopalan, N. Muthuchamy, K.-P. Lee, J.-S. Lee, S.-W. Lee, S.-W. Kim, J.-S. Kim, H.-M. Joeng, J.-B. Kwon, J.-H. Bae and S.-W. Kang, *Sci. Rep.*, 2017, **7**, 45079.

223. S.-H. Oh, S.-I. Na, Y.-C. Nah, D. Vak, S.-S. Kim and D.-Y. Kim, *Org. Electron.*, 2007, **8**, 773−783.

224. S.-H. Oh, S.-I. Na, J. Jo, B. Lim, D. Vak, and D.-Y. Kim, *Adv. Funct. Mater.*, 2010, **20**, 1977−1983.

225. R. Kang, S.-H. Oh and D.-Y. Kim, *ACS Appl. Mater. Interfaces*, 2014, **6**, 6227-6236.

226. C. Han, Y. Cheng, L. Chen, L. Qian, Z. Yang, W. Xue, T. Zhang, Y. Yang and W. Cao, *ACS Appl. Mater. Interfaces*, 2016, **8**, 3301-3307.

227. E. J. Lee, S. W. Heo, Y. W. Han and D. K. Moon, *J. Mater. Chem. C*, 2016, **4**, 2463.

228. P. Shen, M. Yao, G. Wang, R. Mi, W. Guo, Y. Bai and L. Shen, *J. Mater. Chem. A*, 2018, **6**, 17401-17408.

229. S. Park, M. Cha, J. H. Seo, J. Heo, D. C. Lim and S. Cho, *ACS Appl. Mater. Interfaces*, 2018, **10**, 41578-41585.

230. Q. An, X. Ma, J. Gao, F. Zhang, *Science Bulletin*, 2019, **64**, 504-506.

231. C. Duan, W. Cai, B. B. Y. Hsu, C. Zhong, K. Zhang, C. Liu, Z. Hu, F. Huang, G. C. Bazan, A. J. Heeger and Y. Cao, *Energy Environ. Sci.*, 2013, **6**, 3022.

232. L. Lu, T. Xu, W. Chen, J. M. Lee, Z. Luo, I. H. Jung, H. I. Park, S. O. Kim and L. Yu, *Nano Lett.*, 2013, **13**, 2365-2369.

233. V. D. Mihailetchi, L. J. A. Koster, J. C. Hummelen, and P. W. M. Blom, *Phys. Rev. Lett.*, 2004, **93**, 216601.

234. Y. Zhong, M. T. Trinh, R. Chen, W. Wang, P. P. Khlyabich, B. Kumar and Q. Xu, C.-Y. Nam, M. Y. Sfeir, C. Black, M. L. Steigerwald, Y.-L. Loo, S. Xiao, X.-Y. Zhu and C. Nckolls, *J. Am. Chem. Soc.*, 2014, **136**, 15215–15221.

235. L. J. Koster, M. Kemerink, M.M. Wienk, K. Maturova, R.A. Janssen, *Adv. Mater.*, 2011, **23**, 1670-1674.

236. Z. Li, F. Gao, N. C. Greenham and C. R. McNeill, *Adv. Funct. Mater.*, 2011, **21**, 1419-1431.

237. W. Tress, S. Corvers, K. Leo and M. Riede, *Adv. Energy Mater.*, 2013, **3**, 873-880.

238. S. Cho, K.-D. Kim, J. Heo, J. Y. Lee, G. Cha, B. Y. Seo, Y. D. Kim, Y. S. Kim, S.-Y. Choi and D. C. Lim, *Sci. Rep.*, 2014, **4**, 4306.

239. M. Bag and K. S. Narayan, *Phys. Rev. B*, 2010, **82**, 115452.

240. K. Zhu, T. B. Vinzant, N. R. Neale and A. J. Frank, *Nano Lett.*, 2007, **7**, 3739-3746.

241. D. H. Kim, J. Ryu, F. T. A. Wibowo, S. Y. Park, J. Y. Kim, S.-Y. Jang and S. Cho, *ACS Appl. Energy Mater.*, 2020, **3**, 8375-8382.

242. M. T. Dang, J. Lefebvre and J. D. Wuest, *ACS Sustainable Chem. Eng.*, 2015, **3**, 3373-3381.

243. C. Zhang, L. Qi, Q. Chen, L. Lv, Y. Ning, Y. Hu, Y. Hou and F. Teng, *J. Mater. Chem. C*, 2014, **2**, 8715.

244. W. Zhang, W. Ju, X. Wu, Y. Wang, Q. Wang, H. Zhou, S. Wang and C. Hu, *Appl. Surface Sci.*, 2016, **367**, 542-551.

245. W.-C Chang, C.-H. Kuo, P.-J. Lee, Y.-L. Chueh and S.-J. Lin, *Phys. Chem. Chem. Phys.*, 2012, **14**, 13041-13045.

246. C. V. Hoven, A. Garcia, G. C. Bazan and T.-Q. Nguyen, *Adv. Mater.*, 2008, **20**, 3793-3810.

247. P. Maiti, P. Guha, R. Singh, J. K. Dash and P. V. Satyam, *Appl. Surface Sci.*, 2019, **476**, 691-700.

248. L. Ye, Y. Jing, X. Guo, H. Sun, S. Zhang, M. Zhang, L. Huo, and J. Hou, *J. Phys. Chem. C*, 2013, **117**, 14920-14928.

국문 초록

표면 개질을 통한 고성능의 유기태양전지 제작 및 특성 연구

울산대학교 대학원

물 리 학 과

박 수 정

유기태양전지는 저렴한 제작단가, 가벼운 소자, 유연성 및 투명성 등의 장점을 가지고 있어 차세대 모바일기기를 위한 에너지원으로 큰 관심을 받고 있다. 최근에는 새로운 유기 반도체 물질 및 보다 효율적인 소자 구조의 개발로 가파른 성능 향상을 이루어 현재 17%가 넘는 광전변환효율을 나타내고 있다. 이로써 유기태양전지의 대표적인 문제점으로 지적 받았던 낮은 광전변환효율이 극복됨에 따라 상용화에 가까워졌다는 평가를 받고 있다. 하지만 이미 상용화된 무기물 반도체 기반 태양전지와 경쟁하기 위해서는 추가적인 효율 증가가 필요한 상황이다. 광활성층에서 입사된 빛에 의해 생성된 전하들이 분리, 이동의 과정의 거쳐 전극에 도달하기 위해서는 필수적으로 계면을 거쳐야 한다. 하지만, 유기반도체인 광활성층의 계면에서 형성되는 수십 meV의 에너지 장벽은 계면에서의 전하 축적을 유발시켜 광기전력 특성을 감소시킨다. 따라서 전극과 유기 반도체 사이에 효과적인 전하 전달과 전하 재결합을 막을 수 있는 적절한 계면층의 성능 개질은 고성능 태양전지를 구현하기 위해서 필수적으로 요구되고 있는 부분이다. 이에, 본 연구에서는 유기태양전지의 성능을 극대화하기 위해 다양한 계면 처리 방법을 시험하고 유기태양전지의 성능에 미치는 영향을 분석하였다.

첫번째, 정공수송물질로 사용되는 전도성 고분자인 PEDOT:PSS는 금속의 성질을 가지기 때문에 유기 반도체인 광활성층 사이의 계면에서 금속과 반도체 접합에 의한 에너지 장벽이 형성될 수 있다. 본 연구에서는 Hydroquinone (HQ)을 PEDOT:PSS 표면에 처리하여 이 장벽을 제거하고자 했다. PEDOT:PSS 표면에 처리된 HQ는 광활성층과의 계면에서 정공 수송 장벽을 낮추었을 뿐만 아니라 2차 도핑 효과를 통해 PEDOT:PSS의 면저항을 크게 감소시켰다. HQ를 처리한 PEDOT:PSS 기반 소자의 효율은 HQ를 처리하지 않은 소자 대비 28% 향상된 결과를 보였다.

두번째, 탠덤 소자의 터널 접합 중간 연결층은 정공 전도층과 PEI 고분자전해질로 구성된다. 하지만 PEI는 절연체이기 때문에 중간 연결층에서 PEI층이 조금만 두꺼워져도 광전류가 제한된

다. 두번째 연구에서는 탠덤 소자의 터널 접합 중간연결층에 carbon quantum dot (CQD)를 첨가하여 고효율의 탠덤 소자를 구현하고자 했다. 중간 연결층의 PEI에 CQD를 첨가한 탠덤 소자는 더 나은 직렬연결을 형성하며 CQD를 첨가하지 않은 기존의 탠덤 소자 대비 15% 향상된 효율인 최고 효율 12.13%를 보여주었다.

세번째, 엑시톤 분리 확률은 음극과 양극의 일함수 차이로 생성된 내부 전계에 의해서도 영향을 받는다. 본 연구에서는 일함수를 조절하는 PEI층에 NH_2 리간드를 갖는 CQD를 첨가함으로써 일함수 조절 효과와 전하 이동 특성 모두 향상시키고자 했다. CQD를 첨가한 PEI로 개질된 ITO는 기존 PEI로 개질된 ITO의 일함수보다 더 낮은 일함수를 가져 더 강한 내부 전계를 발생시켰다. 이렇게 강화된 내부 전계는 더 나은 엑시톤 분리 효율을 유도하여 유기태양전지 성능을 향상시키는 것으로 분석되었다.

마지막으로, 현재 유기태양전지에는 AI4083과 같이 낮은 전도도를 가지는 PEDOT:PSS가 주로 활용되고 있다. 하지만 PEDOT:PSS와 ITO 사이는 옴 접촉이 아니기 때문에 심각한 계면 문제가 있을 가능성이 높음에도 불구하고 큰 관심을 받지 못하고 있었다. 본 연구에서는 고분자 전해질인 WPFSCz-를 ITO와 PEDOT:PSS 사이에 도입하여 복잡한 유-무기 계면 문제를 극복하고자 했다. 도입된 WPFSCz-층은 ITO의 일함수를 변화시켜 정공 수송에 유리한 효과적인 단계적 에너지 레벨 정렬을 형성했다. 또한 WPFSCz-층의 도입되면서 계면 트랩이 제거됨에 따라 계면에서의 재결합 손실을 감소시켜 FF를 향상시켰다. 이러한 효과를 통해 유기태양전지 효율을 15.86%에서 17.34%로 크게 증가시킬 수 있었다.

이상의 연구를 통해, 유기태양전지에서 서로 다른 종류의 물질들이 접합할 때 계면에서 발생하는 문제를 다양한 계면 처리 방법을 통해 해결할 수 있었다. 이러한 방법들은 전하 이동 특성과 전하 추출 특성을 향상시킴으로써 효율을 증가시켜 고성능의 유기태양전지를 제작을 가능하게 하였다.